



Norwegian University of
Science and Technology

Stability assesment of the headrace tunnel system at Brattset Hydropower Project

Ragna Torås Halseth

Geotechnology

Submission date: June 2018

Supervisor: Krishna Kanta Panthi, IGP

Co-supervisor: Bibek Neupane, IGP

Norwegian University of Science and Technology
Department of Geoscience and Petroleum



Your ref.: MS/N31T44/IGB/RTKKP

Date: 12.01.2018

TGB4930 INGGEOL/BERGMEK - MSc thesis
for
Eng. geo. student Ragna Torås

STABILITY ASSESSMENT OF THE HEADRACE TUNNEL SYSTEM OF BRATTSET
HYDROPOWER PROJECT

Background

Brattset Hydropower Projects is located at Rennebu commune of Sør-Trøndelag fylke and is one of five projects developed KVO (Kraftverkene i Orkla), and is operated by Trønder Energi Kraft. The project lies in the Orkla River between the stretch Storfossmagasinet and Brattset. The project utilizes regulated reservoir and regulated outlet discharge from Ulset and Litjfossen Hydropower Plants, and has a gross head of 270m. The project consists of 16.7 km headrace tunnel system including inclined shaft, 400 m long tailrace tunnel, access tunnel and underground powerhouse. In 2008, after many years of operation, a tunnel collapse occurred from a weakness zone located at the downstream end of the headrace tunnel. In parallel with the rehabilitation work at the collapse area, an inspection was also carried out through the headrace tunnel (approximately 12 km TBM and rest D&B). Similarly, an inspection of the headrace tunnel (mainly TBM part) was also carried out in August 2015. A registration log was created through these two inspections. This MSc work is built based on experience from two inspections in the past and engineering geological surface field mapping carried out by the candidate during autumn 2017 (during project work).

MSc thesis task

This MSc thesis is a continuation of the Project work where the candidate has carried out engineering geological field mapping, assessed engineering geological conditions and identified long-term instability pattern along the headrace tunnel of the Brattset Hydropower Project. Hence, the MSc task will have the following tasks:

- Theoretical review on the Norwegian design principles for unlined waterway systems.
- Review on the instability issues in tunnels and underground cavern.
- Discuss engineering geological conditions and present instability conditions along the headrace tunnel alignment.

- Carry out laboratory testing of the rock samples collected during field mapping.
- Investigate swelling potential of the gauge materials of Norway and evaluate so that it could be used to the stability assessment
- Carry out stability assessment of the instability issues identified using both analytical and numerical modelling.
- Discuss the findings of stability assessment and highlight on the long-term instability issues of Norwegian hydropower tunnels.
- Conclude the work with recommendations.

Relevant computer software packages

Candidate shall use *roc-science package* and other relevant computer software for the master study.

Background information for the study

- Relevant information about the project such as reports, maps, information and data received from the supervisors and collected by the candidate.
- The information provided by the professor about rock engineering and hydropower.
- Scientific papers and books related to international tunnelling cases.
- Literatures in rock engineering, rock support principles, rock mechanics and tunnelling.

Cooperating partner

PhD Fellow Mr. Bibek Neupane will also be the co-supervisor of this MSc thesis.

The project work is to start on January 12, 2018 and to be completed by June 11, 2018.

The Norwegian University of Science and Technology (NTNU)
Department of Geology and Mineral Resources Engineering

January 12, 2018



Dr. Krishna K. Panthi

Associate Professor of geological engineering, main supervisor

Abstract

Unlined high pressure tunnels and shafts are regarded as a Norwegian specialty in the hydropower industry. During the last 60 years, more than 4000 km of hydropower tunnels have been excavated, where most of the tunnels have only 2-4 % of concrete or shotcrete lining. The development of the hydropower industry in Norway has been possible due to cost saving solutions such as the unlined high pressure tunnels and shafts, and air cushion chambers.

In the coming years, the Norwegian hydropower system will be an important resource for balancing the demand and production in the European electricity market. This will require a change in the production pattern, from supply driven to demand driven, which involve higher frequencies of start-and-stop sequences of the turbines in the hydropower plant. This production pattern is in use at Brattset Hydropower Project, where there has been an increase in rock falls and other stability problems in the recent years.

Stability assessments of the different instability issues experienced at Brattset have been carried out. Both empirical and analytical methods are applied, as well as numerical modelling. Input parameters to the analyzes are based on laboratory work, field observations and evaluation of rock mass parameters found in literature. The pressure amplitudes of hydraulic transients at Brattset are also estimated.

It is suggested that due to its long period, the mass oscillations that arise from fluctuating production will have the potential to affect the stability. The effects are mainly concentrated to discontinuities and would influence on the long-term stability of unlined tunnels. The degree of jointing is an important factor in relation to the proposed effects. The water pressure fluctuations due to mass oscillations would therefore be most critical for hydropower schemes situated in jointed rock mass. In order to fully understand the consequences of the new production regime, further research is required. This could involve continuous monitoring of the pressure response within discontinuities during fluctuating operation of the hydropower plants.

Sammendrag

Ufôrete trykktunneler og -sjakter regnes som en norsk spesialitet innen vannkraftindustrien. I løpet av de siste 60 årene er det bygget enn 4000 km med vannkrafttunneler, hvor de fleste tunnelene har kun 2-4 % sprøytebetong eller betongutstøpning. Utviklingen av vannkraftindustrien i Norge har vært mulig på grunn av kostnadsbesparende løsninger som ufôrete trykksjakter og tunneler, og luftputekamre.

Det norske vannkraftsystemet vil i de kommende årene bli en viktig ressurs for å balansere etterspørsel og produksjon i det europeiske elektrisitetsmarkedet. Dette vil føre til en endring i produksjonsmønsteret, fra kontinuerlig produksjon til effektkjøring av anlegget. Dette produksjonsmønsteret innebærer høyere frekvenser av start-og-stopp-sekvenser av turbiner og varierende vannføring i tunnelene. Effektkjøring er også i bruk på Brattset Kraftverk. Der har det i de senere årene vært en økning i antall nedfall i tunnelene og andre stabilitetsproblemer.

Stabilitetsvurderinger av de ulike problemene ved Brattset er utført. Både empiriske og analytiske metoder er benyttet, samt numerisk modellering. Inngangsparametere til analysene er basert på laboratoriearbeid, feltobservasjoner og evaluering av bergmasseparametere fra litteratur. Trykkamplituder til hydrauliske transienter ved Brattset er også estimert.

På grunn av den lange perioden til massesvingningene som oppstår fra varierende produksjon, vil vanntrykket fra svingningene kunne påvirke stabiliteten av vannveissystemet. Effektene er hovedsakelig konsentrert til diskontinuiteter i bergmassen og vil påvirke langtidsstabiliteten av ufôrete tunneler. Oppsprekingsgraden av bergmassen er en viktig faktor når det gjelder de foreslåtte effektene. Trykkvariasjonene på grunn av massesvingninger vil derfor være mest kritisk for vannkraftprosjekter bygget i svært oppsprukket bergmasse. For å fullt ut forstå konsekvensene av det nye produksjonsmønsteret, er det nødvendig med mer forskning. Dette kan innebære kontinuerlig overvåking av trykkresponsen i sprekker under variabel drift av vannkraftverkene.

Preface

This Master thesis is submitted to the Department of Geosciences and Petroleum at the Norwegian University of Science and Technology (NTNU). The thesis work has been carried out during the spring semester of 2018, and is the final submission before fulfilling the Master of Science degree in Geotechnology – Engineering Geology and Rock Mechanics.

The thesis focuses on the instability issues experienced at Brattset Hydropower Project in the recent years, and how these may be connected to the change in operation patterns in the Norwegian hydropower industry.

This thesis is a continuation of the Project work "Engineering geological conditions along the headrace tunnel at Brattset" that was submitted in December 2017. The content of Chapter 2 and Chapter 4 is largely based on literature study from the Project work, while in Chapter 7 the findings from the engineering geological investigations, conducted during the Project work, are summarized.

Associate Professor Dr. Krishna Kanta Panthi has been the main supervisor, and PhD fellow Mr. Bibek Neupane the co-supervisor, during both Project and Master thesis work.

Trondheim, 11.06.2018

Ragna Torås Halseth

Acknowledgments

I would first like to express my gratitude to Associate Professor Dr. Krishna Kanta Panthi, who has been my supervisor. His knowledge and enthusiasm in the fields of engineering geology and hydropower development have truly inspired me and enchanted this work.

PhD fellow Bibek Neupane has been my co-supervisor. He has contributed to this work with interesting discussions and creative ideas. For that I am very grateful.

I would like to thank Tor Harald Landløpet at Trønderenergi Kraft AS for receiving us at Brattset HPP, providing information and answering any questions I have had about the hydro-power project. I am also grateful for all help I have received from Senior Engineer Gunnar Vistnes and Senior Engineer Laurentius Tjihuis, with sample preparation and laboratory testing.

I would like to thank my dear Mathias, my parents and the rest of my family for all support and motivation throughout the studies and in the process of writing this thesis.

Finally, I will thank my fellow students for five good years at NTNU and excellent company in our study hall. I would also seize the opportunity to congratulate you all with finalized Master's, your efforts have been extraordinary.

R.T.H.

Contents

- Abstract iii
- Sammendrag v
- Preface vii
- Acknowledgments ix
- Table of Contents xi

- 1 INTRODUCTION 1**
- 1.1 Background of the study 1
- 1.2 Scope of study 2
- 1.3 Methodology 3
- 1.4 Limitations 4

- 2 DESIGN OF UNLINED WATERWAY SYSTEMS 5**
- 2.1 Introduction 5
- 2.2 Norwegian geology and topography 6
- 2.3 Development history 7
- 2.4 Design principles 9
 - 2.4.1 Required geological conditions 9
 - 2.4.2 Confinement criterion 10
- 2.5 Support philosophy 13

- 3 ROCK MASS PROPERTIES 15**
- 3.1 Introduction 15
- 3.2 Rock mass strength and deformability 16
 - 3.2.1 Failure criteria 16
 - 3.2.2 Estimation of rock mass strength 20
 - 3.2.3 Estimation of rock mass deformability 20
 - 3.2.4 Post-peak behaviour 21
 - 3.2.5 Strength anisotropy 23
 - 3.2.6 Weathering and alteration 24
- 3.3 Discontinuities 26
 - 3.3.1 Jointing of the rock mass 26

3.3.2	Shear strength of joints	29
3.3.3	Faults and weakness zones	30
3.4	Rock stresses	32
3.4.1	In-situ stresses in rock mass	32
3.4.2	Rock stresses surrounding a tunnel	34
3.5	Significance of water	35
3.5.1	Hydraulic conductivity of rock mass	36
3.5.2	Effect of saturation upon rock mass strength and stiffness	36
4	INSTABILITY ISSUES IN TUNNELS AND UNDERGROUND CAVERNS	39
4.1	Introduction	39
4.2	Structurally controlled failure	40
4.3	Stress-controlled failure	40
4.3.1	Failure mechanisms in brittle rock mass	41
4.4	Failure in faults and weakness zones	42
4.4.1	Swelling process and potential	43
5	HYDRAULIC TRANSIENTS IN THE WATERWAY SYSTEM	47
5.1	Hydraulic transients	47
5.2	Water hammer	48
5.3	Mass oscillations	48
5.4	Pressure period and amplitude	49
5.5	Effects of hydraulic transients on waterway systems	51
5.6	Hydraulic transients at Brattset HPP	51
5.6.1	Calculations of water hammer wave	52
5.6.2	Calculation of mass oscillations	52
6	REVIEW OF CASES	55
6.1	Collapse of Svandalsflona pressure shaft	55
6.1.1	Project description and geology	55
6.1.2	Rock mass conditions and support	56
6.1.3	Failure of weakness zone	57
6.2	Glendoe headrace tunnel collapse	58
6.2.1	Project description	59
6.2.2	Rock mass conditions and support	60
6.2.3	Tunnel collapse	60
6.3	Lessons learned from case studies	61
7	BRATTSET HYDROPOWER PROJECT	63

7.1	Project description	63
7.2	Project layout	65
7.2.1	Intake area	65
7.2.2	Headrace tunnel	66
7.2.3	Powerhouse area	66
7.3	Rock support	66
7.4	Engineering geological conditions	66
7.4.1	Geological setting	67
7.4.2	Rock mass conditions	67
7.4.3	Rock mass quality	72
7.4.4	In-situ rock stresses	73
7.5	Instability issues along the headrace tunnel	74
7.5.1	Collapse in weakness zone	74
7.5.2	Stress induced spalling and buckling	75
7.5.3	Block fall caused by intersecting discontinuities	77
7.5.4	Block fall caused by joints and induced fracturing	77
8	LABORATORY INVESTIGATIONS	79
8.1	X-Ray Powder Diffraction (XRD)	79
8.1.1	Procedure and results	80
8.2	Point load index test	81
8.2.1	Procedure and results	83
8.3	Results from testing of quartz keratophyre	84
9	ESTABLISHMENT OF INPUT PARAMETERS	87
9.1	Estimation of rock mechanical properties	87
9.1.1	Compressive strength	88
9.1.2	Elastic parameters	88
9.1.3	Hoek-Brown parameters	88
9.1.4	Dilation parameter	90
9.2	Joint properties	90
9.2.1	Shear strength parameters	90
9.2.2	Joint stiffness	91
9.3	Water pressure in joints	92
9.3.1	Distribution of load	92
9.4	Estimation of in-situ stress conditions	94
9.4.1	Model set up	94
9.4.2	Results	95

9.4.3	Application in further analysis	96
10	STABILITY ANALYZES	99
10.1	Introduction	99
10.1.1	Software for numerical modelling	99
10.2	Potential to stress induced instability	100
10.2.1	Stress potential classification by the Q-system	100
10.2.2	Maximal tangential stress and rock spalling strength approach	101
10.2.3	Stress conditions	102
10.2.4	Results	103
10.3	Limit equilibrium analysis of wedge fall	103
10.3.1	Model geometry	105
10.3.2	Identification of forces	106
10.3.3	Results	109
10.4	Spalling and buckling in schistose phyllite	110
10.4.1	Model set up	110
10.4.2	Input parameters	111
10.4.3	Modelling results	112
10.5	Block fall caused by joints and induced fracturing	114
10.5.1	Model geometry and setup	114
10.5.2	Input parameters	115
10.5.3	Results	117
10.6	3D modelling of swelling pressure in weakness zone	120
10.6.1	Model set up and geometry	120
10.6.2	Input parameters	121
10.6.3	Results	124
11	DISCUSSIONS	127
11.1	Design principle and hydraulic transients	127
11.2	Discussion on stability assessments	128
11.2.1	Input parameters	128
11.2.2	Potential to spalling	129
11.2.3	Wedge fall	130
11.2.4	Induced fracturing intersecting joint	131
11.2.5	Collapse of weakness zone	132
11.3	Long-term instability issues	133
12	CONCLUSIONS AND RECOMMENDATIONS	137
12.1	Conclusions	137

12.2 Recommendations	138
BIBLIOGRAPHY	139
APPENDICES	147
A STRIKE AND DIP MEASUREMENTS	147
B Q-VALUE ESTIMATION	149
C ESTIMATION OF GSI	153
D MAPS AND DRAWINGS RELATED TO PROJECT	155
E LAB RESULTS	161
F STANDARD CHART AND FIGURES	165

Chapter 1

Introduction

1.1 Background of the study

The total annual electricity production in Norway is in the order of 140-145 TWh, where 96 % of the production is covered by hydroelectric power (SSB, 2017). During the last century more than 200 hydropower stations have been built underground, and more than 4000 km of waterway tunnels have been excavated (Broch, 2013). Most of these tunnels are unlined, meaning that the amount of rock reinforcement is kept to a minimum.

In 1991, a new energy law was implemented in Norway. The law stipulated that the hydro electrical production would gradually develop from being supply driven to demand driven (Bråtveit et al., 2016). In Europe, it is expected that electricity production from non-regulated renewable sources, such as solar and wind power, will increase. Norwegian hydropower plants have the opportunity to store large amounts of water in the reservoirs, and are able to regulate the power production. Norwegian hydropower could therefore be an important resource for balancing the demand and production in the European electricity market (Grøv et al., 2011; Solvang et al., 2011).

The change in the production scheme, from supply to demand driven, involves higher frequencies of start-and-stop sequences of the turbines as well as more fluctuating production patterns. These rapid changes in the power production, generate pressure oscillations within the waterway systems (Nilsen and Thidemann, 1993). Bråtveit et al. (2016) inspected a number of unlined Norwegian waterway tunnels, and found that unlined tunnels subjected to this production method, have experienced an increased frequency of rock fall. The majority of hydropower projects in Norway were built before 1990 and designed with a more continuous production plan in mind. The long-term effects of the new operation pattern to the unlined waterways are therefore of great interest.

Brattset Hydropower Projects is located in Rennebu municipality in Sør-Trøndelag county.

It is one of five projects developed by KVO (Kraftverkene i Orkla), all operated by Trønder Energi Kraft. In 2008, after many years of operation, a collapse occurred in the downstream end of the headrace tunnel. The collapse was located in a weakness zone, and about 50 m³ of mass had fallen into the tunnel, blocking half of the tunnel cross-sectional area (Nyhaug, 2008). During the time of rehabilitation of the collapsed area, an inspection of the headrace tunnel was carried out. Similarly, a new inspection was done in August 2015. During both inspections a large number of instability issues were encountered, from small sized spalling to large block falls with volumes up to 15 m².

According to Nyhaug (2008) the weakness zone was most likely not discovered during construction of the tunnel, and the collapse in 2008 is an example of instability issues developing over time. The number of other instabilities observed during the tunnel inspections are also indicating that more issues are present. According to Dr. Krishna Panthi (discussion with supervisor during Project work), the amount of erosion damages and stability problems has increased since the production scheme changed towards higher frequencies of start-and-stop cycles and fluctuations.

The Project work carried out in the fall semester of 2017, utilized the experience gained during the two inspections in 2008 and 2015, to identify the stability issues developing in the headrace tunnel. In this Master thesis the focus will be to conduct stability assessments of the identified instabilities and look into the reasons behind the increasing amount of stability problems.

1.2 Scope of study

The scope of the thesis includes the following:

1. Theoretical review on the design philosophy of unlined hydropower tunnels in Norway.
2. Review on common instability issues in tunnels and underground caverns, including case studies.
3. Discussions of the engineering geological conditions along the headrace tunnel, which were studied during the Project work.
4. Laboratory testing of the rock samples collected during field mapping
5. Investigation of swelling potential of the gouge materials found in Norwegian tunnels, and evaluation of the findings so that it could be used in the stability assessment
6. Stability assessments of the identified instability issues using both empirical, analytical and numerical methods.

7. Discussions of the findings from the stability assessments and on the long-term instability issues of Norwegian hydropower tunnels.
8. Conclusions from the work, including recommendations related to long-term instability issues

1.3 Methodology

The methodology of the study can be summarized as follows:

1. Literature study

Most of the literature is found through the search engine *Oria*, at the NTNU University library. In addition have the proceedings from "Fjellsprengningskonferansen" and other publications from The Norwegian Tunneling Society (NFF) been valuable sources of information. The main topics of the literature study are:

- (a) Norwegian design principles for unlined waterway systems
- (b) Rock mass properties influencing stability
- (c) Stability problems in underground openings
- (d) Hydraulic transients in waterway systems

2. Study of Brattset Hydropower Project

Information regarding the project layout is gathered from maps, tender drawings and illustrations of the waterway system. Reports from tunnel inspections in 2008 and 2015 have been the main source for information about the instability issues at Brattset. The results from field work during the Project work have been the basis for evaluation of the engineering geological conditions along the headrace tunnel.

3. Estimation of stress conditions and rock mass properties

Stress conditions have been estimated from stress measurements, elastic analysis in RS^2 and the tunnel overburden. Rock mass properties have been estimated through use of the following methods:

- (a) Laboratory testing: Point load test and XRD analysis
- (b) Classification systems and empirical relationships
- (c) Estimation of input parameters to stability analysis using *RocData*

4. Stability assessments

Assessments of the identified stability issues have been carried out using different techniques. This include both empirical and analytical methods, as well as numerical methods. The following approaches have been applied:

- (a) Empirical method: Potential to spalling based on the Q-method from (NGI, 2015)

- (b) Semi-analytical method: Depth impact of spalling based on maximum tangential stress and spalling strength from (Martin and Christiansson, 2009)
- (c) Analytical method: Limit equilibrium analysis of wedge fall
- (d) Numerical method: Finite element analysis in both 2D and 3D, using computer software from *Rocscience* (RS^2 and RS^3)

1.4 Limitations

As the author was not involved in any of the tunnel inspections carried out in 2008 and 2015, the evaluation of the instability issues at Brattset is based on the documentation given from these. Identifying the modes of failure was difficult due to the limited access to good pictures of the failures in the tunnel. Considerations of the occurred events are largely based on short descriptions given in the reports combined with the authors interpretation of the geological setting.

The main challenge of the thesis has been to obtain reliable input to the stability assessments. The phyllite sample was too schistose for UCS testing, so only point load test was conducted for obtaining strength estimates. Other input values are estimates from surface mapping and literature study. Stress conditions are also estimated with the use of general trends of stress directions in the area and the results from stress measurements during construction of the power plant.

Calculations of hydraulic transients that arise from start and stop of the turbines are done by simplified equations. For instance are losses due to friction neglected. Exact measures of the tunnel layout are also difficult to determine, as drawing, maps and illustrations occasionally deviate from each other.

Chapter 2

Design of unlined waterway systems

2.1 Introduction

The Norwegian electricity production relies heavily on hydropower as the most important source of energy. According to SSB (2017) the hydropower industry in Norway generated 143.4 TWh in 2016, which was 96.3 % of the total electricity production in the country. Figure 2.1 shows how the total installed capacity in Norwegian hydropower plants has continuously increased since the development of hydropower projects accelerated in the 1950s and 60s. The majority of the powerhouses built since 1950 is located underground, and today the hydropower industry includes over 200 underground power houses and more than 4000 km of tunnels (Broch, 2013).

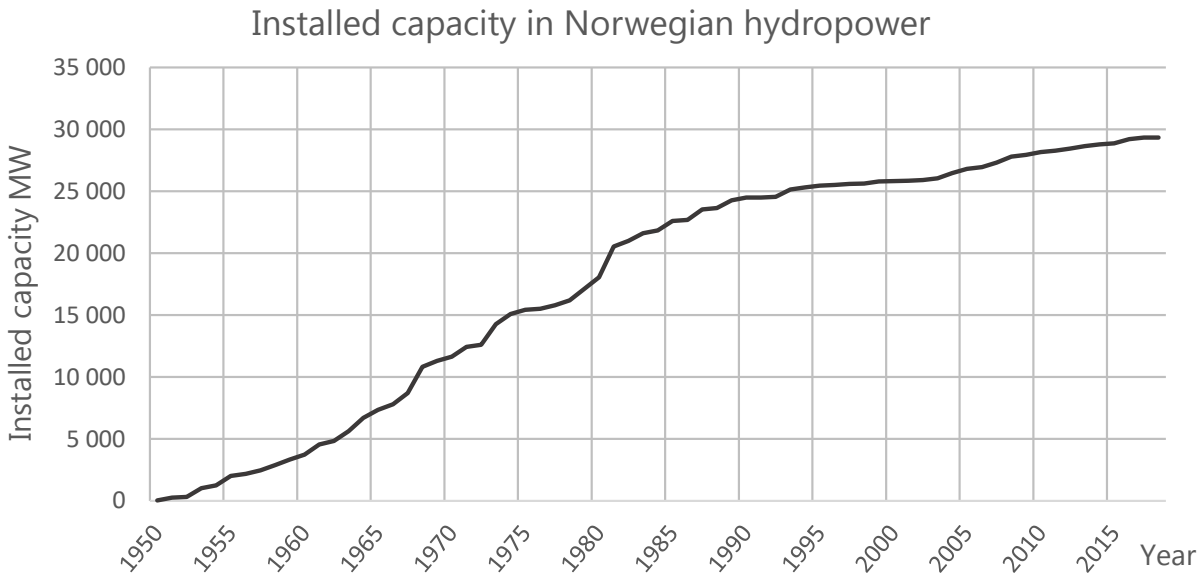


Figure 2.1: Installed capacity in Norwegian hydropower 1950 - 2017. Data from NVE (2017)

2.2 Norwegian geology and topography

The bedrock of Norway is old. The dominating rocks originate from the medium to late Precambrian period, with an age of 800 to 2500 million years (Panthi, 2014b). The Precambrian rocks form a part of the Baltic Precambrian shield, which include Norway, Sweden, Finland and the Kola Peninsula in Russia (Nilsen and Broch, 2012). Approximately two thirds of the bedrock in Norway is of Precambrian age. The Precambrian areas are dominated by different types of gneisses, but rock types such as granite, gabbro, amphibolite, quartzite and sandstone are also found (Nilsen and Thidemann, 1993). The remaining third of the Norwegian bedrock is dominated by rocks of Cambro-Silurian age, mainly from the formation of the Caledonian mountain range that stretches south-west towards north, see Figure 2.2. In these areas can rocks with varying degree of metamorphism, such as gneisses, schists, phyllites, greenstones and marbles be found, together with granites, gabbros, sandstones, shales, dolomites and limestones (Selmer-Olsen and Broch, 1982).

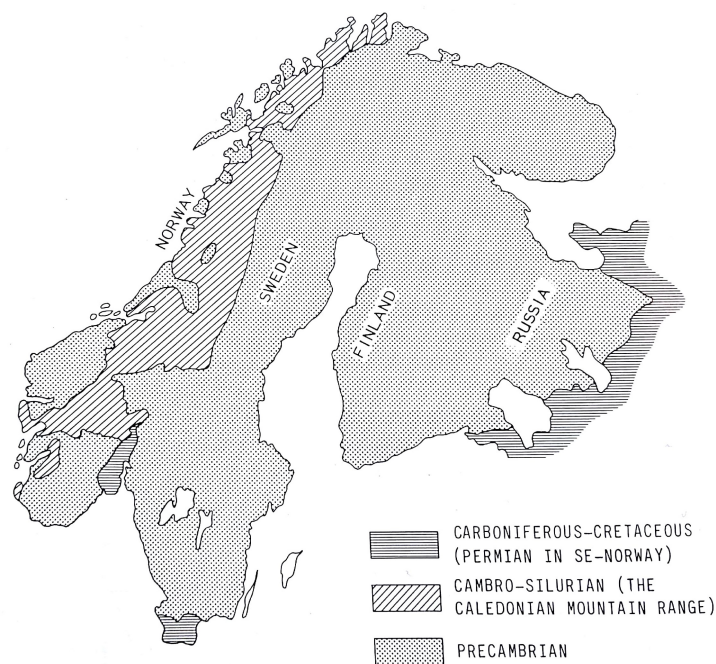


Figure 2.2: Simplified geological map of the Baltic Precambrian Shield (Nilsen and Thidemann, 1993)

Due to the large appearance of massive hard rock types, which from an engineering perspective generally are classified as high quality rock mass, Norway is often referred to as a hard rock province. However, many Norwegian rock types and rock masses typically have anisotropic mechanical properties and show a great variation in joining (Selmer-Olsen and Broch, 1982). As a result of several epochs of orogeny, with the Caledonian as the latest, most of the bedrock in Scandinavia is highly metamorphosed (Nilsen and Thidemann, 1993).

These earth movements have also led to the development of numerous faults, shear zones and thrust zones, features that may cause challenges during excavation and influence the stability of underground openings (Palmström, 1996). Another important feature of the Scandinavian region is the excessive erosion that has taken place during several de-glaciations over the last 1-2 million years, where the last ended 8500 years ago (Nilsen and Broch, 2012). The glacial erosion has removed most of the weathered rock cover, leaving nearly unweathered rock under a cover of young soils, less than 12 000 years (Selmer-Olsen and Broch, 1982). The bedrock is often exposed in outcrops, making it possible to predict the underground conditions from simple surface observations, mapping and sampling (Palmström, 1996).

The topography of Norway is well suited for the hydropower development. Topographically, almost 70 % of Norway's land area has an elevation of 300 or above, and 40 % exceeding 600 m (Hveding, 1992). Uplifting of the landmasses during Tertiary faulting and the glacial erosion from de-glaciations have caused a special topography in Norway, characterized by a highland plateau with numerous lakes of all sizes, and deeply eroded valleys and fjords cutting into the plateau (Nilsen and Thidemann, 1993). The elevation difference, considerable precipitation, and the many rivers and lakes provide ideal conditions for hydropower development (Panthi, 2014b).

2.3 Development history

The hydropower development in Norway is characterized by advances in tunneling technology, support philosophy and the use of innovative design solutions. Today the typical Norwegian approach involves unlined high pressure tunnels and shafts, and often use of an air cushion chamber. The beginning of these innovative designs can be traced back to the 1920. During and shortly after the First World War there was a shortage of steel, leading to uncertain deliveries and a considerable increase in the steel prices. As a result, the use of an above ground steel penstock to lead the water from the supply tunnel or reservoir to the power station (upper left in Figure 2.3) became too expensive. The hydropower industry was forced to find new solutions, and as a result four hydropower stations with unlined pressure tunnels were put into operation in 1919-21 (Broch, 1984; Broch, 2006). One of these (Skar) was a complete failure due to too low overburden, while the other three (Svelgen, Toklev, Herlandsfoss) operated successfully after fixing some initial problems (Broch, 1984).

Even though unlined tunnel and shafts were constructed and successfully operating during the 20s, the traditional solution of above ground powerhouse and penstock was continued until the 1950s. After World War Two, hydropower stations and tunnels were preferred placed underground for wartime security reasons. But as equipment and excavation meth-

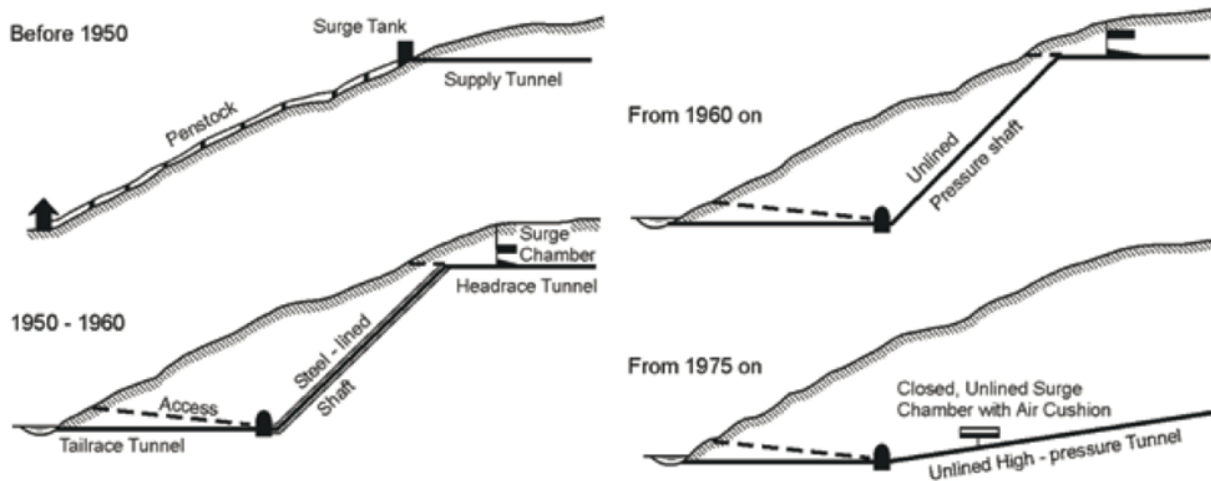


Figure 2.3: The development of the Norwegian waterway layout (Broch, 2013)

ods rapidly advanced after the war, underground construction generally became the most economical solution for hydropower projects (Broch, 2006). As illustrated in Figure 2.3, the use of steel penstock was still common practice at this time, and for the next 10 years or so steel-lining was put in use at mostly all new pressure shafts. During 1950-65 a total of 36 steel-lined pressure shafts were constructed, with water heads varying between 50-967 m (Broch, 1984).

It was not until 1958, almost 40 years after the record of 152 m static head in an unlined pressure tunnel at Svelgen was beaten. When the Tafjord K3 project, with a static head of 282 m, was set into operation in 1958, the industry gained new confidence in unlined pressure shafts. More unlined pressure shafts were constructed in the early 1960s and after 1965 the unlined shaft became the conventional solution for heads up to 600 m (Broch, 1984). Thereafter the concept of keeping the waterway system unlined, including high pressure shafts and tunnels, became a Norwegian specialty (Panthi, 2014b). Figure 2.4 reflects the growing confidence in unlined pressure shafts and tunnels. It shows a trend of continually increasing water heads, from the first record at Svelgen in 1921 until Nye Tyn in 2004 with a head of 1047 m (Panthi and Basnet, 2016).

The tightness of the rock mass was a key element when another innovative solution in the Norwegian hydropower engineering was introduced. In 1973 the first enclosed air cushion chamber was successfully put into operation at Driva Hydropower Plant (Rathe, 1975). The chamber is filled with compressed air, which acts as a cushion, damping the water oscillations due to starts and stops or rapid changes in the power production (Rathe, 1975; Nilsen and Thidemann, 1993). With the air cushion chamber, the conventional surge-shaft and

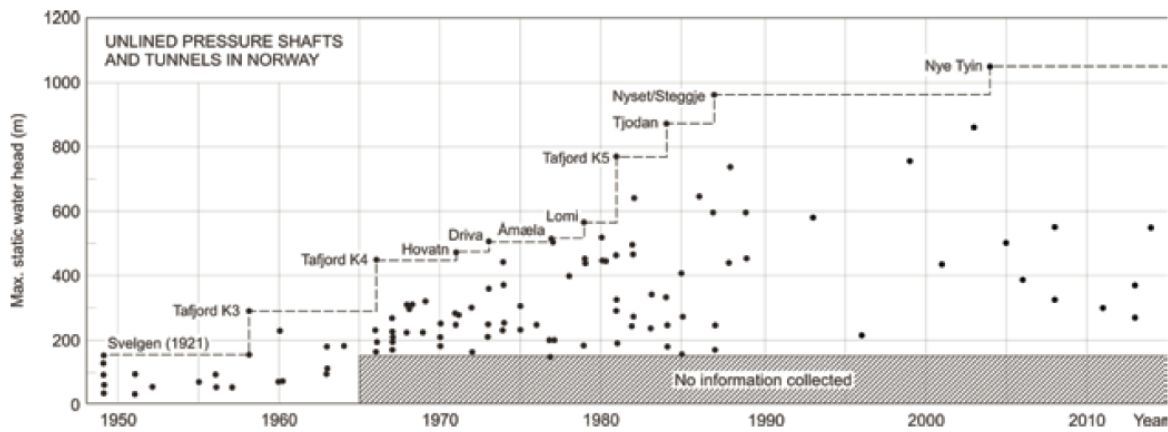


Figure 2.4: The development of unlined pressure shafts and tunnels in Norway (Broch, 2013).

surge-chamber arrangements could be replaced, giving more flexibility to the project layout (Rathe, 1975). It was no longer necessary to use shallow nearly horizontal headrace tunnel and inclined high pressure shaft. Instead a slightly inclined tunnel could be used to lead water directly from the reservoir towards the powerhouse (Kjørholt et al., 1992), as illustrated to the lower right in Figure 2.3.

2.4 Design principles

The stability of tunnels and shafts are highly influenced by the mechanical properties of the surrounding rock and the stress situation and distribution of stresses around the excavation (Panthi, 2014b). The Norwegian design principles consist of two main criteria that need to be fulfilled when planning an unlined high pressure shaft:

1. Required geological conditions
2. Sufficient confinement

2.4.1 Required geological conditions

As discussed earlier, the rock mass in Norway is dominated by high quality rock. This is favourable when designing unlined high pressure shafts and tunnels. However, there are certain conditions that can cause major problems if not avoided or handled by appropriate measures. The following conditions are emphasized by Nilsen and Thidemann (1993) as especially unfavourable, and recommended to avoid when placing the tunnel or shaft:

1. Rocks with high porosity, like some types of volcanic rocks and sandstones
2. Karstic areas

3. Heavily jointed rock mass with open and intercommunicating joints
4. Weakness zones and faults with unfavourable orientation
5. Impermeable layers of rock or clay above the tunnel or shaft, that may cause high water pressure to build up at critical locations

2.4.2 Confinement criterion

The second criterion, sufficient confinement, is highly influenced by topography and the distribution of stresses in the valley side. The tunnel or shaft should be placed such that the water pressure acting on the excavation wall is not exceeding the lowest principal stress in the rock mass. If the internal pressure is too high, this could lead to hydraulic splitting and deformations in the surrounding rock (Nilsen and Broch, 2012). To fulfill this requirement a number of design criteria have been suggested over the years. As more experience has been gained from completed projects, the criteria have continuously been revised and improved (Nilsen and Thidemann, 1993).

The first criteria

The first design criteria used for unlined high-pressure shafts and tunnels were based on equilibrium considerations. According to Broch (1984) the rule of thumb for planning unlined pressure shafts in Norway before 1968 was expressed as:

$$h > c \cdot H \quad (2.1)$$

where:

h = vertical depth of point studied

H = static water head (in m) at point studied

c = constant with a value of 0.6 for valley sides with inclination up to 35° , increased to 1.0 for valley sides up to 60°

In 1968 the unlined pressure shaft at Byrte, which had an inclination of 60° , failed. Inclination angles above 45° were rather uncommon, and after the failure a revised rule of thumb was presented by Selmer-Olsen (1969). This criterion took the inclination of the shaft into account:

$$h > \frac{\rho_w \cdot H}{\rho_r \cdot \cos \alpha} \quad (2.2)$$

where:

α = inclination of shaft

ρ_w = density of water

ρ_r = density of rock mass

According to Bjørlykke and Selmer-Olsen (1972) the formula is restricted to shafts up to 60°. Steeper shafts had to be placed within the assumed line of a 45° shaft. They also states that the formula is only valid for valley sides up to 35°, and for steeper valley sides only valid within several restricting conditions. A second formula presented by Bergh-Christiansen and Dannevig in 1971 included the inclination of the valley side:

$$L > \frac{\rho_w \cdot H}{\rho_r \cdot \cos \beta} \quad (2.3)$$

where:

L = shortest distance between surface and point studied

β = average inclination of valley side

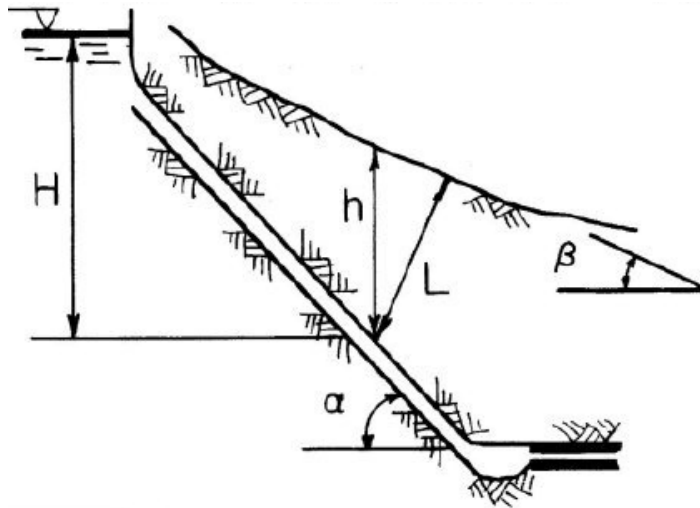


Figure 2.5: Parameter definitions for design criteria (Broch, 1984)

Finite element method and design charts

The empirical equilibrium rules of thumb presented above were purely based on the gravitational induced stresses in the rock mass. However, the rock stresses in valley sides are largely influenced by topography and in some cases tectonic stresses (Nilsen and Broch, 2012). Bjørlykke and Selmer-Olsen (1972) point out that Equation (2.3) is applicable at points where the principal stresses are normal to and parallel to the valley side. This may be the case in the middle part of the slope, close to the surface. But due to topography, the principal stresses will deviate from this in areas near the top plateau and the valley bottom. The equation will therefore give either too optimistic or too conservative overburden values at these points.

A better way to analyze these types of problems became available in 1972, when Bjørlykke and Selmer-Olsen (1972) presented a method based on a finite element analysis of two-dimensional models. The method is based on strain analysis, and can be used with various

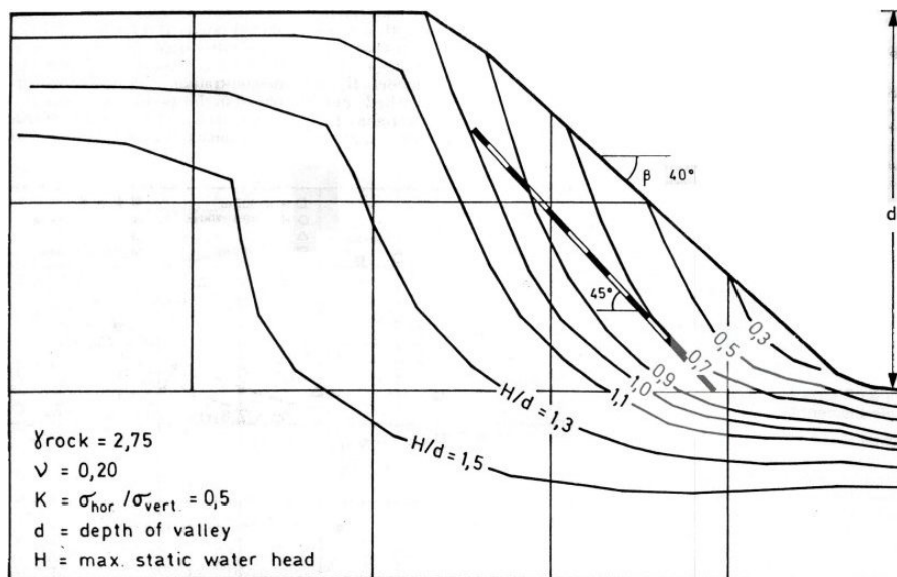


Figure 2.6: Design chart from finite element model. The curves run through points where the internal water pressure equals the minor principal stress in the rock mass. The pressure shaft is placed with sufficient overburden for $H/d = 0.7$ (Broch, 1984).

input for valley inclination (β) and rock properties (γ, ν). A result from such an analysis is presented as a design chart, as illustrated in Figure 2.6. The horizontal stress is given by both gravitational and tectonic stresses. This is defined by the factor K , which is the σ_h/σ_v ratio in a distance $5d$ from the valley. The static water head is expressed as the ratio H/d , where H is the maximum static head and d is the depth of the valley. A design chart can be obtained from the model calculations, showing lines running through points where the water head is equal to the minor principal stress in the surrounding rock mass. Each line represents the least overburden required at the given conditions H/d . The tunnel or shaft can then be placed inside the model such that the internal water pressure does not exceed the minor principal stress in the rock mass at any point.

Restrictions

Both the "rule of thumb" design formulas and the finite element method is based on two-dimensional considerations and a simplified geometry. These design methods must therefore be used with caution. This is especially important in areas where the topography forms a ridge, giving a convex shape to the valley side and stress relieve of the rock mass. Broch (2000) suggests that the ridges should therefore be accounted for in the design. This is done by making a revised topographical profile where the extra overburden is ignored.

The criterion of sufficient confinement is today often expressed in such a way that the maximum water pressure should never exceed the minor in-situ stress in the rock mass (Panthi, 2014b):

$$\sigma_3 > H \cdot \gamma_w \quad (2.4)$$

This requirement can be controlled by rock stress measurements, such as hydraulic fracturing, and use of numerical modelling. Usually a factor of safety is required, depending on the complexity of the geology, degree of pre-investigations, accuracy of stress measurements and knowledge of the final water head (Aasen et al., 2013).

2.5 Support philosophy

Rock support for underground excavations can be divided into two categories: preliminary support required for safety during construction and permanent support for long term stability. There is not always any practical difference between these two, as support methods such as rock bolts and pre-grouting can function as both preliminary and permanent support (Thidemann and Bruland, 1992; Bråtveit et al., 2016).

In the Norwegian support philosophy for hydropower tunneling, the rock mass is regarded as a self-supporting material that can carry considerable loads, even in jointed condition (Thidemann and Bruland, 1992). The idea has been to use the rock mass as a structural element and to limit the amount of rock reinforcement. This as a cost-effective method (Kristiansen and Stokkebø, 1992). The cost of installing rock support to completely prevent all rock fall has been considered to be significantly higher than the costs related to head loss caused by the rock debris (Bråtveit et al., 2016). The common consensus has therefore been to accept some minor rockfall within the waterway system (Broch, 2006). According to Broch (2006) most of the Norwegian hydropower tunnels have only 2-4 % of concrete or shotcrete lining. In a few cases it has been necessary to increase this to 40-60 %. For potential leakage zones sealing by grouting is preferred (Buen and Palmstrøm, 1985).

Chapter 3

Rock mass properties

3.1 Introduction

For engineering purposes it is important to distinguish between rock and rock mass. Rock is by definition a naturally composed aggregate of one or more minerals, and the properties of the rock will depend of the mineral composition, size, shape, orientation and binding forces between the minerals (Nilsen and Thidemann, 1993). However, the rock mass is a heterogeneous construction material consisting of the intact rock, all joints and other discontinuities. The presence of these structures will therefore have influence on the properties of the material which is being excavated and in which the tunnel or cavern is located (Nilsen and Palmström, 2000).

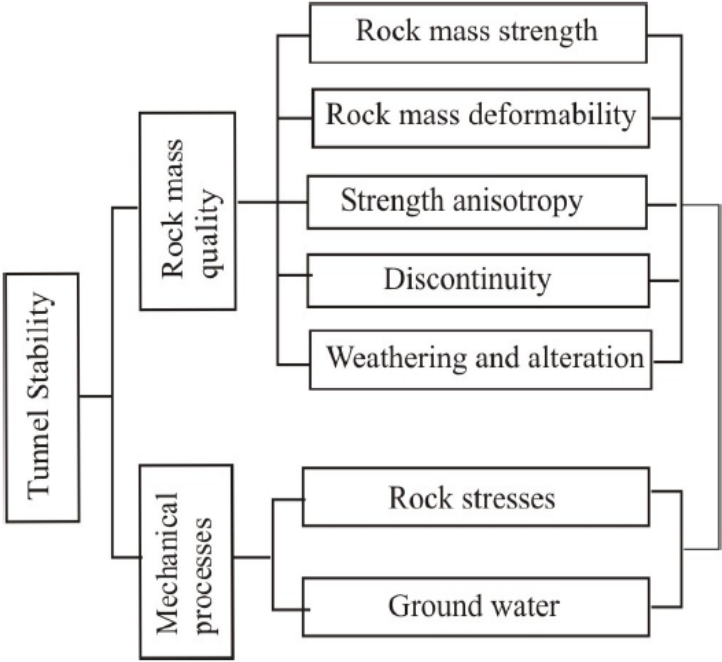


Figure 3.1: Factors influencing tunnel stability (Panthi, 2006)

In connection to stability of underground excavations, Panthi (2006) identifies two main features that characterize the rock mass: rock mass quality and mechanical processes acting on the rock mass. These two features are highly interlinked, as illustrated in Figure 3.1. The rock mass quality is determined by rock mass strength, deformability, strength anisotropy, discontinuities and weathering. The mechanical processes that influence the tunnel stability are rock stresses and groundwater. Additionally, the stability will be influenced by project specific factors such as the size, geometry, location and orientation of the excavation (Panthi, 2006; Nilsen and Palmström, 2000). In this chapter the rock mass properties and features influencing the stability of underground openings will be reviewed.

3.2 Rock mass strength and deformability

Reliable estimates for rock mass strength and deformation characteristics are important information in all aspects of rock engineering. Intact rock strength (σ_{ci}) and intact deformation modulus (E_{ci}) are typically determined through laboratory testing or field tests (Nilsen and Palmström, 2000). The rock mass strength (σ_{cm}) and rock mass deformation modulus (E_m) are usually estimated by empirical relationships.

3.2.1 Failure criteria

From an engineering perspective it is of great interest to have a measure of the failure properties in the rock mass and the ability to predict when failure will occur. Over the years a number of different failure criteria have been developed. Among theoretical failure criteria the most commonly used is the Mohr-Coulomb criterion (maximum effective shear stress) (Hudson and Harrison, 1997). A criterion that has gathered greater acceptance is the generalized Hoek-Brown criteria. It is an empirical criterion based on experimental failure data plotted in the $\sigma_1 - \sigma_3$ plane (Hudson and Harrison, 1997).

The Mohr-Coulomb criterion

When a rock specimen is loaded by three principal stresses, it is observed that the specimen fails in a mode of shear. The ultimate stress σ_1 and the confining stress σ_3 at failure can be presented by a Mohr's circle in a $\sigma - \tau$ -diagram. If a series of compression tests is conducted at different confining stresses, the envelope of the Mohr's circle represent the envelope of the rock strength. For rock material this curve is usually non-linear, but that the curve can be well approximated by a straight line in most cases (Li, 2015a). The Mohr-Coulomb failure criterion (M-C criterion) is given by the linear function:

$$\tau = c + \sigma_n \tan \phi \quad (3.1)$$

where the relation between the shear stress τ and the normal stress σ_n at failure is expressed. Associated with the criterion are also the parameters ϕ and c . ϕ is the angle of internal friction, and is equivalent to the angle of inclination of a surface sufficient to cause sliding of a material down the surface, and c is the cohesion, which is the pure shear strength of the material when no confining stress is applied (Hudson and Harrison, 1997; Li, 2015a).

The plane of failure does not coincide with the plane of maximum shear stress, i.e. at the plane where

$$\tau_{max} = \frac{\sigma_1 - \sigma_3}{2}, \quad \text{that is at } \beta = 45^\circ \quad (3.2)$$

At this plane the normal stress is too high for sliding to take place. However, if the angle of inclination is increased, the normal stress and hence the friction are reduced. At a specific angle, the frictional resistance is lower than the shear stress and sliding will occur along the plane, i.e. failure appear. As shown in Figure 3.2 this angle is given as $\beta^\circ = 45 + (\phi/2)$, where ϕ is the material's internal friction (Hudson and Harrison, 1997; Myrvang, 2001).

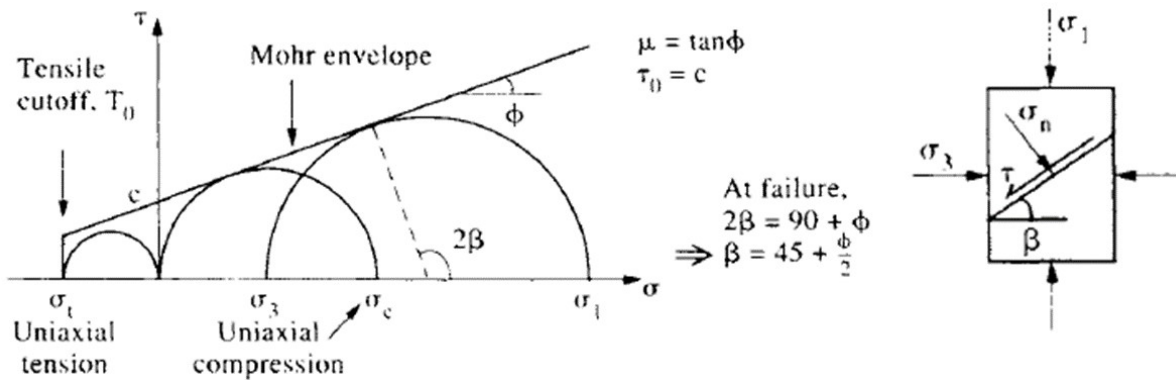


Figure 3.2: The Mohr-Coulomb failure criterion (Hudson and Harrison, 1997)

Because the criterion is developed for compressive stress, a *tensile cut-off* (T_0) is normally utilized to give a realistic value or the uniaxial tensile strength (Goodman, 1989). Hence, according to the criterion, failure or permanent deformation will take place in one of two ways (Myrvang, 2001):

1. The effective shear stress τ in the failure plane exceeds a certain value, depending on the normal stress σ_n on the same plane
2. The largest tensile stress exceeds the tensile strength σ_t

All stresses in the M-C criterion are effective stresses. If pore pressure is present in the rock, the effective principal stresses decrease (since $\sigma' = \sigma - p$), shifting the Mohr's circle to the left in the $\tau - \sigma$ -diagram by an amount equal to the pore pressure. This could lead to the possibility of intersection with the strength envelope and failure (Hudson and Harrison, 1997).

The Mohr-Coulomb failure criterion is a simple criterion of failure, which has proven to be fast and reliable for engineering purposes. According to Hudson and Harrison (1997), the criterion is especially significant and valid for discontinuities and discontinuous rock masses.

Generalized Hoek-Brown criterion

The original Hoek-Brown failure criterion was developed by Hoek and Brown in the late 70s to provide a reliable method for estimating the strength of jointed rock masses (Brown, 2008). The criterion is an empirically derived relationship, based on fitting of parabolic curves to tri-axial test data (Eberhardt, 2012). The original Hoek-Brown failure criterion for *intact rock* (Hoek and Brown, 1980) was expressed as:

$$\sigma_1 = \sigma_3 + \sigma_{ci} \left(m \frac{\sigma_3}{\sigma_{ci}} + s \right)^{0.5} \quad (3.3)$$

where σ_1 and σ_3 are the major and minor principal stresses at failure, σ_{ci} is the uniaxial compressive strength of the intact rock, and m and s are dimensionless constants which depend upon the properties of the rock.

Since the original criterion was presented, the criterion has been updated several times in response to the experience gained through its use and to meet the need for application to new problems (Hoek, 2007). The Generalized Hoek-Brown criterion for jointed rock masses presented by Hoek et al. (2002) is defined by:

$$\sigma'_1 = \sigma'_3 + \sigma_{ci} \left(m_b \frac{\sigma'_3}{\sigma_{ci}} + s \right)^a \quad (3.4)$$

where σ'_1 and σ'_3 are the major and minor effective principal stress at failure, σ_{ci} is the uniaxial compressive strength of the intact rock pieces, m_b is the Hoek-Brown constant m for the rock mass, and s and a are constants which depend upon the rock mass characteristics. The material constants m_b , s and a are defined as follows:

$$m_b = m_i \exp \left(\frac{GSI - 100}{28 - 14D} \right) \quad (3.5)$$

$$s = \exp \left(\frac{GSI - 100}{9 - 3D} \right) \quad (3.6)$$

$$a = \frac{1}{2} + \frac{1}{6} (e^{-GSI/15} - e^{-20/3}) \quad (3.7)$$

Here m_i is the value of the Hoek-Brown constant for intact rock and GSI is the Geological Strength Index. The value D is the disturbance factor. Its value depends on the degree of

disturbance of the rock mass by blast damage and stress relaxation. It varies from 0 for undisturbed rock masses to 1 for very disturbed rock masses (Hoek et al., 2002).

The Hoek-Brown criterion assumes isotropic rock and rock mass behaviour, and should only be applied to homogeneous rock mass or rock mass with a sufficient number of closely spaced discontinuities, with similar surface characteristics. In this case isotropic behaviour involving failure can be assumed (Hoek, 2007). In cases where the block size is of the same order as the structure being analyzed, or when one joint set is considerably weaker than the others, the criterion should not be used. This is illustrated in Figure 3.3, which shows the transition from a small intact rock specimen, through failure controlled by one or two discontinuities, to an isotropic jointed rock mass. Hoek (2007) argues that the Hoek-Brown criterion is applicable when considering large-scale rock masses, as the strength will reach a constant value when the size of the individual rock pieces is sufficiently small compared to the overall structure being analyzed.

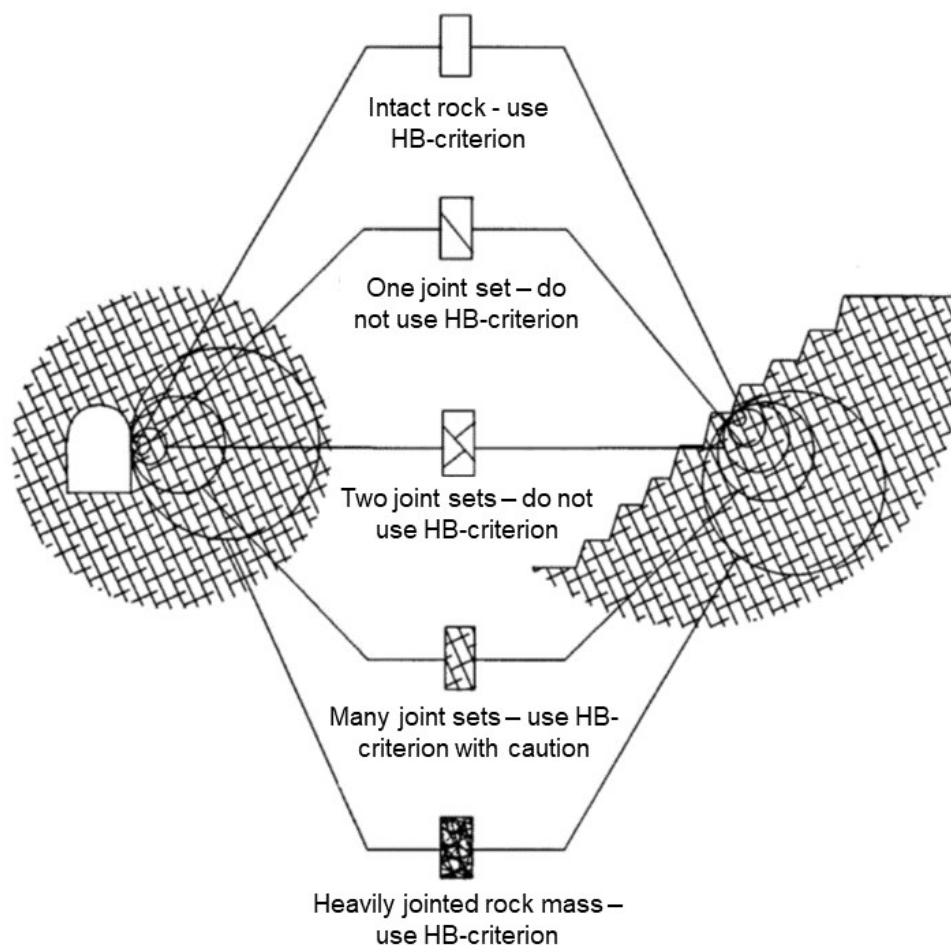


Figure 3.3: Applicability of the Hoek-Brown criterion (HB-criterion) from intact to heavily jointed rock mass. Modified from Hoek (2007).

3.2.2 Estimation of rock mass strength

The rock mass strength can be defined as the rock mass' ability to withstand stress and deformation (Panthi, 2006). Estimates of the rock mass strength are required in almost any types of analysis used for the design of underground excavations (Hoek, 2007). The strength and deformation of an intact rock sample are different from the strength and deformation of the rock mass. The rock mass strength is influenced by discontinuities, foliation or schistosity planes, and the orientation of these features relative to the direction in which the strength is assessed. The intact rock specimen is usually strong and homogeneous, with few discontinuities, and will therefore not represent the strength of the total rock mass (Panthi, 2006).

The intact rock strength is often estimated through testing of rock samples collected in field. Common test methods are the uniaxial compressive test, triaxial test and point load strength test (Nilsen and Thidemann, 1993). The strength of the rock mass is however difficult to estimate directly in field or by laboratory tests. Many authors have therefore suggested empirical relationships for the estimation of rock mass strength (σ_{cm}), presented in Table 3.1. Typically, these methods include the intact rock strength (σ_{ci}) and a rock mass characterization parameter, such as the Q-value or RMR (Rock Mass Rating).

Table 3.1: Indirect estimation of rock mass strength

Proposed by	Empirical relationship
Bieniawski (1993)	$\sigma_{cm} = \sigma_{cm} \times \exp\left(\frac{RMR-100}{18.75}\right)$
Palmström (1995)	$\sigma_{cm} = RMi = \sigma_{ci} \times JP$
Aydan et al. (1997)	$\sigma_{cm} = 0.0016RMR^{2.5}$
Hoek et al. (2002)	$\sigma_{cm} = \sigma_{ci} s^a = \sigma_{ci} \times \left[\exp\left(\frac{GSI-100}{9-3D}\right)\right]^a$
Barton (2002)	$\sigma_{cm} = 5\gamma(Q\frac{\sigma_{ci}}{100})^{1/3}$
Panthi (2017)	$\sigma_{cm} = \frac{\sigma_{ci}^{1.6}}{60}$ for brittle rock mass
Panthi (2017)	$\sigma_{cm} = \frac{\sigma_{ci}^{1.5}}{60}$ for schistose rock mass

Where JP is the joint parameter in the RMi system, s and a are material constants related to the Hoek-Brown failure criteria and γ is the rock mass density (g/cm^3)

3.2.3 Estimation of rock mass deformability

When the rock mass is subjected to load it will deform. The relationship between the applied load and the resulting deformation is characterized by a modulus. Hudson and Harrison

(1997) describe how the deformation in the rock mass is made up of two components: the deformation of the intact rock and the deformation of the discontinuities. Since jointed rock mass does not deform elastically, the use of *modulus of deformation* rather than modulus of elasticity is preferred (Bieniawski, 1978). ISRM (1975b) define the *modulus of elasticity* (E_{ci}) or *Young's modulus* as "the ratio of stress to corresponding strain below the proportional limit of a material", and the *modulus of deformation* (E_m) as "the ratio of stress to corresponding strain during loading of rock mass including elastic and inelastic behaviour".

The modulus of deformation can be measured in field by different methods, such as plate bearing, dilatometer test, flatjack test, hydraulic chamber etc. These test often provide values that differ considerably, giving rise to uncertainties and difficulties to assess the significance of the tests (Bieniawski, 1978; Nilsen and Palmström, 2000). Also, the tests are time-consuming and costly. Several authors have therefore proposed different empirical equations, where the modulus of deformation is estimated from other relevant parameters (see Table 3.2).

Table 3.2: Indirect estimation of the deformation modulus

Proposed by	Empirical relationship
Bieniawski (1978)	$E_m = 2RMR - 100$
Palmström (1995)	$E_m = 5.6RMI^{0.375}$
Hoek et al. (2002)	$E_m = \left(1 - \frac{D}{2}\right) \sqrt{\frac{\sigma_{ci}}{100}} \cdot 10^{\frac{GSI-10}{40}}$
Barton (2002)	$E_m = 10 \times Q_c^{1/3} = 10 \times \left(\frac{Q \cdot \sigma_{ci}}{100}\right)^{1/3}$
Hoek and Diederichs (2006)	$E_m = E_{ci} \left(0.02 + \frac{1-D/2}{1+e^{((60+15D-GSI)/11)}}\right)$
Panthi (2006)	$E_m = E_{ci} \times \frac{\sigma_{cm}}{\sigma_{ci}}$

3.2.4 Post-peak behaviour

When using numerical models to study the failure and deformation of rock masses, the post peak characteristics of the rock mass are required as input parameters (Hoek, 2007). The post-peak values, also known as residual values, are difficult to determine. There has been little work in literature that deals with the field scale behaviour of rock mass subjected to substantial failure or damage (Crowder and Bawden, 2004). Hoek (2007) suggests that the peak/residual relation is dependent on the quality and hardness of the rock mass, as illustrated in Figure 3.4. The figure indicates that good quality, hard rock mass experience large reduction of strength after yielding, while poor quality, soft rock mass experience a ductile behaviour.

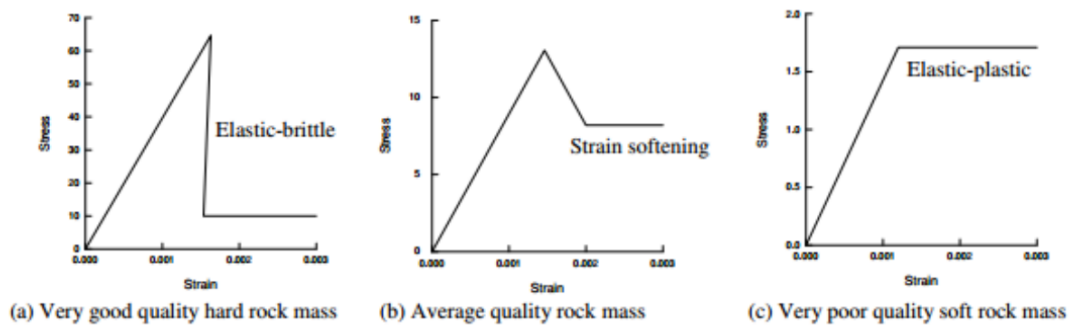


Figure 3.4: Post-peak characteristics for different quality rock masses (Hoek, 2007)

Based on the same guidelines, Crowder and Bawden (2004) summarize the failure mechanisms and post-peak behaviour of rock mass based on the GSI value, see Table 3.3. When choosing residual values for use in numerical modelling, it is important to keep in mind that these suggested behaviours are only general guidelines and, as Hoek (2007) points out, should only be used together with problem-specific judgment.

Table 3.3: Post-peak behaviour of rock mass. From Crowder and Bawden (2004)

Description	GSI	Failure mechanism	Post-peak behaviour
Massive brittle rock	70-90	Stress induced failure of intact rock	All strength lost at failure
Jointed strong rock	50-65	Failure of joint systems	Rock fails to "gravel"
Jointed intermediate rock	40-50	Strain softening	Loss of tensile strength, retains shear strength
Very weak rock	< 30	Already in residual state	Elastic-perfectly plastic behaviour

Estimate of residual strength from GSI

Cai et al. (2007) proposed a method to estimate the residual strength of rock mass based on the GSI classification system. They observed that the post-peak strength of fractured rock mass depends on the resistance along the developed failure surfaces or shear zones, and the degree of interlocking between the block volumes after failure. The procedure involves a reduction in the GSI value by reducing the two major controlling factors in the GSI system, the block volume and joint conditions. To obtain a residual GSI_r value, an evaluation of the residual block volume and residual joint conditions is done. For joint conditions, the major factor that is affected by deformation is the joint roughness. The residual block volume is normally controlled by the quality of the rock mass, and is normally in the range of blocky/disturbed to fully disintegrated, i.e. reduced to "gravel" (Cai et al., 2007).

The determination of GSI_r is illustrated in Figure F3 in Appendix F. The peak GSI value is reduced by the combination of degradation of the block volume and joint surface conditions

from peak to residual state. When utilizing the method with residual GSI_r , it is assumed that intact rock mass properties such as σ_{ci} and m_i remain unchanged. The residual strength parameters are calculated using the generalized Hoek-Brown criterion in the same way as with peak strength parameters. Also, the equivalent Mohr-Coulomb strength parameters can be calculated based on the Hoek-Brown parameters (Cai et al., 2007).

3.2.5 Strength anisotropy

Goodman (1989) defines strength anisotropy as the variation of compressive strength according to the direction of loading. Strength anisotropy is characteristic for rocks composed of minerals with parallel arrangements such as mica, chlorite, clay or hornblende. Hence, as a result of bedding, foliation, schistosity and banding, strength anisotropy is especially common in sedimentary and metamorphic rocks such as shales, slates, schists and banded gneisses (Goodman, 1989).

Figure 3.5 illustrates the effect of anisotropy on the uniaxial compressive strength of different rock types. The figure shows that the rock strength is lowest when the schistosity plane is inclined with an angle of around 30 degrees from the loading direction. The highest strength is obtained when the schistosity plane is oriented perpendicular to the loading direction. It is often difficult to determine the compressive strength of anisotropic rocks, as it is not always easy to drill cores of rock samples oblique to the schistosity plane. However, a reliable method to determine the grade of strength anisotropy is the point load test, where the point load strength is tested both normal to and parallel with the schistosity plane. From the maximum and minimum strength an anisotropy index can be defined, and the rock can be classified according to Table 3.4 (Panthi, 2006).

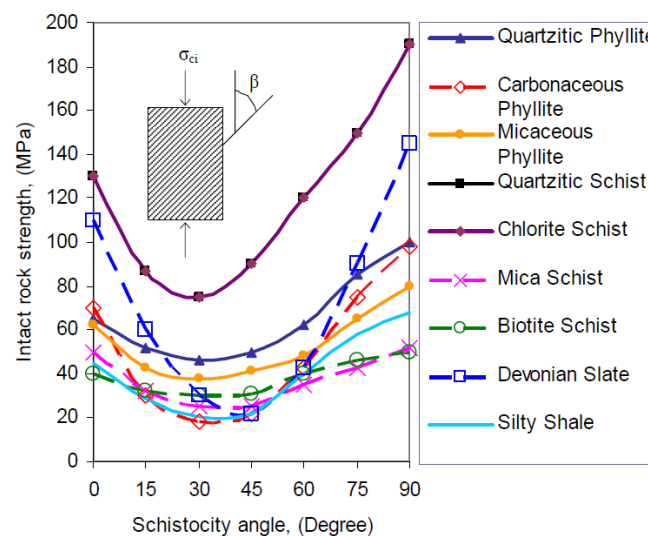


Figure 3.5: Uniaxial compressive strength at different angles to schistosity (Panthi, 2006)

Table 3.4: Classification of rock strength anisotropy (Panthi, 2006)

Classification	Strength anisotropy index I_a	Description
Isotropic rock	1-1.2	< 10 % platy/prismatic minerals, may be randomly orientated <i>Rock types: Igneous rocks and very high grade metamorphic rocks (diorite, granite, gabbro, quartzite, granitic gneiss, granulite, etc.)</i>
Slightly anisotropic	1.2-1.5	10-20 % platy/prismatic minerals, showing compositional layering. <i>Rock types: High grade metamorphic rocks and some strong sedimentary rock (quartz-feldspatic gneiss, mylonite, marble, migmatite, sandstone, limestone, etc.)</i>
Moderately anisotropic	1.5-2.5	20-40 % platy/prismatic minerals, with distinctly visible foliation plane. <i>Rock types: Medium-high grade metamorphic rocks (mica gneiss, quartzitic schist, mica schist, biotite, schist, etc.)</i>
Highly anisotropic	2.5-4.0	40-60 % platy/prismatic minerals, very closely foliated. <i>Rock types: Low - medium grade metamorphic rocks (phyllite, silty slate, etc.)</i>
Extremely anisotropic	> 4.0	>40-60 % platy/prismatic minerals, very closely foliated. <i>Rock types: Low grade metamorphic and argillaceous sedimentary rock (slate, carbonaceous phyllite, shale, etc.)</i>

3.2.6 Weathering and alteration

Weathering refers to the various processes of physical disintegration and chemical decomposition of the rock material as a consequence of exposure to the atmosphere and hydrosphere (Palmström and Stille, 2015). The physical disintegration involves mechanical breakdown of the rock mass, leading to fragmentation, opening of joints, formation of new joint surfaces and fracturing of individual mineral grains (Nilsen and Palmström, 2000). Chemical decomposition or alteration cause changes in the chemical and mineralogical composition of the rock mass. The process may cause discoloration of the rock, leaching or solution of calcite, anhydrite and salt minerals, and eventually decomposition of rock minerals into clay minerals (Nilsen and Palmström, 2000; ISRM, 1978b). According to ISRM (1978b), typically both the chemical and physical weathering processes act together. But depending on the climate regime, one or the other of these aspects may be dominant. The processes first affect the walls of discontinuities, resulting in changes in wall strength. As weathering processes progress, the rock mass weathering grade can be classified according to Table 3.5. In general, the degree of weathering usually decreases with depth below the surface.

According to Panthi (2006), weathering of the rock mass reduces properties such as strength, deformability, slaking durability (resistance against disintegration when hydrated) and fric-

tional resistance. Additionally, the weathering processes may significantly increase the permeability of the rock mass. Panthi (2006) presented a correlation between weathering grade and the reduction of compressive strength, shown in Figure 3.6. The figure indicates a variation in the degree of influence for different rock types. For a moderate weathering grade, the intact rock strength may be reduced by almost 40 % for sedimentary rocks, and almost 80 % for crystalline rocks. Similar trends may also be found regarding elasticity modulus (Panthi, 2006).

Table 3.5: Weathering grade classification according to ISRM (1978b)

Term	Description of rock mass conditions	Grade
Fresh rock	No visible sign of rock material weathering: perhaps slight discoloration on major discontinuity surfaces.	I
Slightly weathered	Discoloration indicates weathering of rock material and discontinuity surfaces. All rock material may be discolored by weathering and may be somewhat weaker externally than in its fresh condition.	II
Moderately weathered	Less than half of the rock material is decomposed and/or disintegrated to a soil. Fresh discolored rock is present either as a continuous framework or as corestones.	III
Highly weathered	More than half of the rock material is decomposed and/or disintegrated to a soil. Fresh discolored rock is present either as a discontinuous framework or as corestones.	IV
Completely weathered	All rock material is decomposed and/or disintegrated to a soil. The original mass structure is still largely intact.	V
Residual soil	All rock material is converted to soil. The mass structure and material fabric are destroyed. There is a large change in volume, but the soil has not been significantly transported.	VI

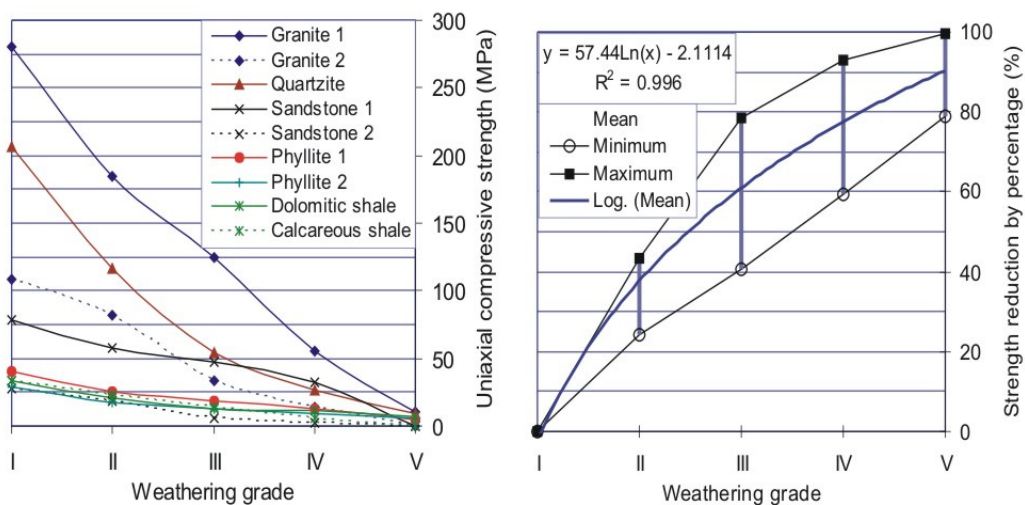


Figure 3.6: Compressive strength of rock (left) and strength reduction in percentage (right) as a function of weathering grade (Panthi, 2006)

3.3 Discontinuities

Nilsen and Palmström (2000) define a discontinuity as a structural or geological feature that alters the homogeneity of the rock mass. According to ISRM (1978b) is discontinuity a general term for any mechanical discontinuity in the rock mass that has zero or low tensile strength. It is a collective term for most types of joints, weak bedding planes, weak schistosity planes, weakness zones and faults. In an engineering context the discontinuities are possibly the single most important factor governing the mechanical properties of the rock mass (Hudson and Harrison, 1997).

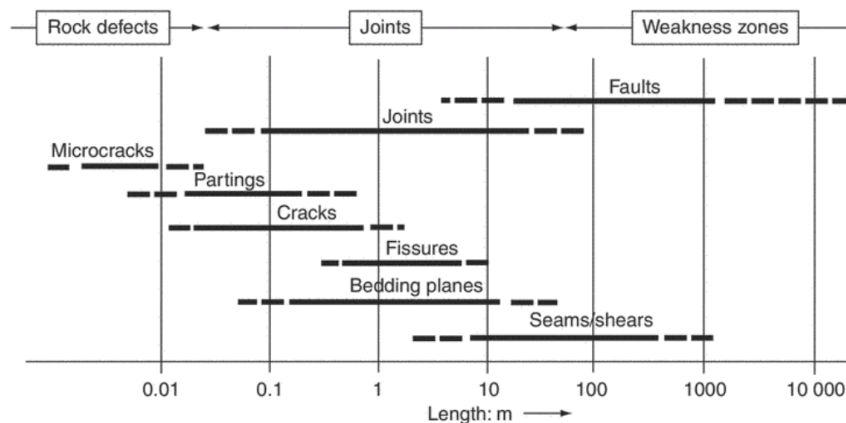


Figure 3.7: Size range of the main types of discontinuities (Palmström and Stille, 2015)

Most discontinuities are a result of tectonic activity in the Earth's crust, often forming families, sets or patterns related to their formation (Palmström and Stille, 2015). The extent of discontinuities varies from several kilometers down to a few centimeters. Large scale discontinuities include faults and weakness zones, while smaller scale discontinuities include joints, seams and cracks, see Figure 3.7. The different discontinuity types may have completely different significance to the stability of an underground excavation. Properties such as roughness, degree of weathering, filling material and permeability will vary greatly from one type of discontinuity to another, depending on their origin, age and formation history (Nilsen and Palmström, 2000).

3.3.1 Jointing of the rock mass

Joints are the most common discontinuities in the rock mass, and include a great variety of types. The terms used for the different joint types are generally chosen based on the size and composition (crack, fracture, seam etc.) or their origin (tectonic joints, exfoliation joints, bedding joints, foliation joints etc.) (Nilsen and Palmström, 2000). Joint of a certain, preferred orientation are called a joint set, and two or more joint sets in an area form a joint pattern or joint system.

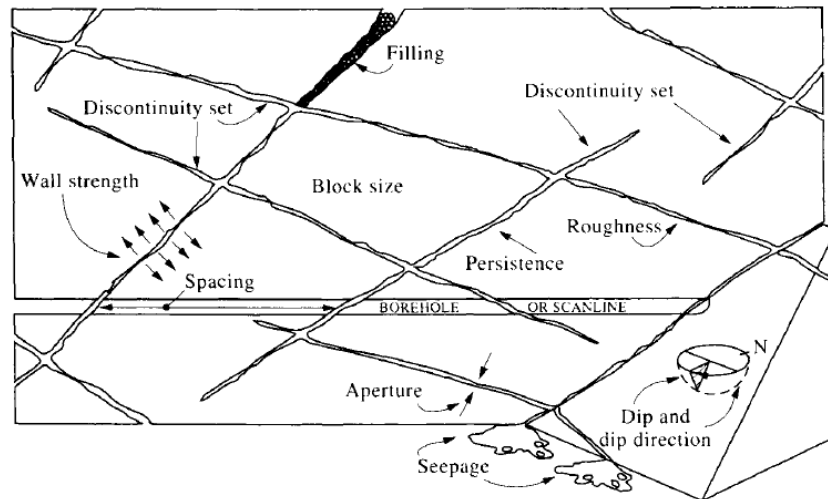


Figure 3.8: Discontinuity characteristics in the rock mass (Hudson and Harrison, 1997)

Joint characteristics

Joints have a number of defining characteristics. The most important geometrical and mechanical characteristics are illustrated in Figure 3.8. The joint surface roughness, wall conditions, aperture and filling, influence the shear strength along the joint planes, and also the susceptibility of water seepage. Other characteristics are joint orientation, spacing, persistence and number of joint sets. These features define the size and shape of the distinct blocks of the rock mass (Palmström and Stille, 2015). In the following, the most critical joint characteristics regarding underground stability are described.

Surface roughness: Roughness is described by ISRM (1978b) as large scale undulations (*waviness*) and small scale roughness (*unevenness* or *smoothness*). Both waviness and unevenness contribute to the shear strength along the joint plane. If the waviness undulations are interlocked and in contact they will cause dilation during shear displacement, as they are too large to be sheared off. The asperities of the unevenness tend to be damaged during shear displacement unless the wall strength is high and/or the stress levels are low.

Alteration and filling: Material separating the adjacent rock walls of discontinuities is called filling material. The filling can consist of several different minerals and materials, such as calcite, chlorite, clay or silt (ISRM, 1978b). The thickness of filling ranges from millimeters to decimeters. For unfilled joints, alteration of the rock walls may cause coating (less than 1 mm thick) (Palmström and Stille, 2015). Alteration and filling of the discontinuities is a result of processes of weathering, hydro-thermal alteration and shearing cycles of the rock mass. Gouge material may form on the discontinuity surface as a result of shear movement, while groundwater flow through open joints can transport and deposit foreign material between the structural planes (Panahi, 2006; Palmström, 1995). The main types of joint fillings and their properties are described in Table 3.6.

Table 3.6: Main joint filling characteristics and their properties. Modified from Nilsen and Palmström (2000)

Type of filling	Characteristics	Type and properties of material
No filling, clean joint	Healed or welded joints. The joint plane may often be regarded as a plane of reduced strength.	Healing through precipitation from solutions of quartz, epidote or calcite.
	Fresh rock walls	Unweathered or unaltered joint walls. May show staining (rust) on the surfaces.
	Altered or weathered rock walls	Weathering and alteration is often more pronounced along the joint surface than in the rock. Wall strength is considerably lower than of fresh rock found in the interior of the rock blocks.
Coating, thin layer of "paint" with some mineral	Coating will affect the shear strength of joints, especially if they are planar and have some wet coating of chlorite, talc or graphite.	Joint coating is not thicker than a few millimeters. It can consist of several different minerals, such as chlorite, mica, calcite, epidote, clay, graphite, zeolite.
Filling, thicker than coating	Chlorite, talc, graphite filling	Very low friction materials, especially when wet.
	Inactive clay materials filling	Weak cohesive materials with low friction.
	Swelling clay filling	Exhibit very low friction and swelling with loss of strength. Exerts considerable swelling pressure when confined.
	Calcite filling	May dissolve over time, particularly when porous and flaky, and strongly reduce the shear strength of the joint.
	Gypsum filling	May behave in the same way as calcite
	Filling of sandy or silty materials	Cohesionless, friction materials. A special occurrence is thick filling of altered or crushed (sand-like) materials that may run or flow immediately after exposure by excavation.
	Filling of epidote, quartz and other hard materials	May cause healing or welding of joints, resulting in increased shear strength.

Weathering and alteration often strongly change the roughness and frictional properties, and hence the strength of the joint surface (Nilsen and Palmström, 2000). The type of coating or filling as well as the thickness are significant for the joint friction. Joints with no filling or with only thin, hard filling are favorable for stability, while joints with thick, soft filling will result in low friction and poor stability (NGI, 2015). In some cases, precipitation from hydro-thermal solutions of quartz, epidote or calcite may cause healing or welding of joints, resulting in increased shear strength (Palmström and Stille, 2015).

Persistence Persistence is the areal extent or length of a discontinuity within a plane (ISRM, 1978b). Joint persistence can be distinguished into *continuous* and *discontinuous*. Continuous joints terminate at another joint, while discontinuous joints terminate in massive rock. This may be foliation partings, en echelon joints or smaller joints (Nilsen and Palmström, 2000).

According to Palmström (1995) there are often one dominant joint set present in the rock mass, being more continuous than joints of other sets. This is referred to as a *major* joint set. The other *minor* joint sets tend to terminate against the major set or in massive rock (ISRM, 1978b). The persistence of joints may also vary within one particular joint set. This is often the case for foliation joints where small joints or partings may occur between longer, continuous joints (Nilsen and Palmström, 2000).

Block size: Intersecting joints separate the rock mass into distinct blocks. The dimensions of these rock blocks are determined by the joint spacing, number of joint sets and persistence of the joints. The shape of the resulting blocks is determined by the number of joint sets and the joint orientations (ISRM, 1978b). The block size is an extremely important parameter in the rock mass behaviour. Rock mass composed of large blocks tends to be less deformable and has good arching and interlocking abilities. Small block sizes reduce the interlocking effect and increase the rock mass permeability and susceptibility to water seepage (Panthi, 2006).

3.3.2 Shear strength of joints

In order to analyze the stability of the rock mass in an underground opening, it is necessary to evaluate factors that influence the shear strength of the joints. The fictional conditions along the joints are generally defined by the roughness of the joint surface and the presence of joint filling. The shear strength of joints can be described by the Coulomb law:

$$\tau = \sigma_n \tan \phi \quad (3.8)$$

where σ_n is the normal stress along the joint and ϕ is the *apparent friction angle* of the joint

surface (Li, 2015a). The Barton-Bandis empirical joint model gives an expression to the apparent peak friction angle:

$$\phi = JRC \log_{10} \frac{JCS}{\sigma_n} + \phi_r \quad (3.9)$$

where JRC is the *joint roughness coefficient*, JCS is the *joint compressive strength* and ϕ_r is the residual friction angle corresponding to the residual strength after shearing (Li, 2015a). If the normal stress acting on the joint surface is known, the shear strength can then be estimated by:

$$\tau = \sigma_n \tan \left[JRC \log_{10} \frac{JCS}{\sigma_n} + \phi_r \right] \quad (3.10)$$

3.3.3 Faults and weakness zones

Nilsen and Palmström (2000) define a weakness zone as "a part of the rock mass where the mechanical properties are significantly lower than those of the surrounding rock mass". This includes structures such as faults, shear and shear zones, thrust zones, weak mineral layers etc. These zones require special attention as they can have a major impact on the tunnel stability as well as the excavation process (Panthi, 2006). Problems connected to such zones are for instance flowing and running ground, swelling pressure and high water inflow (Nilsen and Palmström, 2000).

Types of weakness zones

Nilsen and Thidemann (1993) divide weakness zones into two main categories: (1) zones of particularly weak beds or layers of sedimentary or metamorphic rock, and (2) zones of crushed and/or altered rock formed by faulting or other tectonic events. Many of the zones of weak material are regarded as weakness zones only if they are surrounded by other, stronger rock masses. In many cases the zone has a sharp boundary to the adjacent, stronger rocks. The material in these zones may consist of weak minerals such as clay, mica, talk, graphite, serpentine, etc. or may have become weak through weathering and alteration processes along rock layers, dykes, joints, seams etc. (Nilsen and Palmström, 2000).

Weakness zones formed by tectonic movements in the crust are often referred to as faults, faulting zones or fracture zones. These zones can vary greatly in composition, from heavily jointed to completely crushed rock, and with relatively small amounts of clay filling to highly weathered or hydrothermally altered, swelling clay gouge (Nilsen and Palmström, 2000). Figure 3.9 shows the structure of some fracture zones. Typically, the zones consist of a central core and a transition zone. The central core consists of highly fractured and

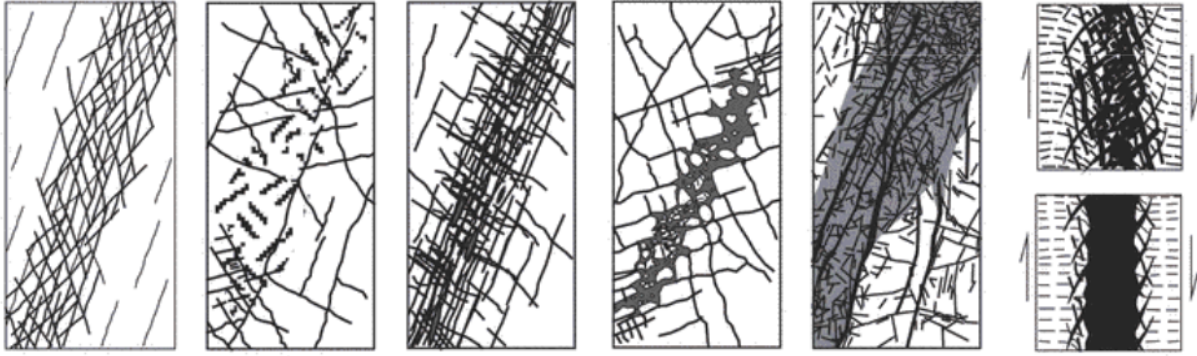


Figure 3.9: Some types of weakness zones. Shaded areas indicate altered rock, and black areas indicate filling or gouge (Palmström and Stille, 2015)

altered rock mass, with primarily clay or silt filling. The transition zone is made up of various fractures that decrease in frequency and size in the direction away from the central zone (Panahi, 2006). As a tunneling excavation approaches a zone of intense crushing, it will pass through rock mass of increasing jointing.

Gouge material

The filling material and gouge that can be found in faults and weakness zones normally constitutes a very complex material in regard to mineralization and physical properties (Nilsen and Palmström, 2000). The character of the filling material is an important factor affecting the stability of the zone. The typical behaviour of some types of filling and gouge material are described in Table 3.7.

Table 3.7: Various filling and gouge materials and their behaviour. Modified after Nilsen and Palmström (2000)

Dominant material in filling/gouge	Characteristic behaviour
Swelling clay	Swelling, sloughing and squeeze, low shear strength. This could cause rock falls, sliding, and in some cases collapses. The initial water content and later change of water content can be important for the mobilized swelling pressures.
Inactive clay	Slaking and sloughing caused by squeeze
Chlorite, talc, graphite, serpentine	Ravelling, low shear strength when wet.
Porous or flaky calcite, gypsum	May dissolve, leading to reduced stability.
Crushed rock fragments (gravel size) or sand-like filling	Ravelling or running. Fragments crushed to an almost cohesionless, sand-like material, can cause serious run or flow into the tunnel
Quartz, epidote	Durable, high strength. May act as a "welding" that increases stability

Faults containing swelling clay are a major risk to tunnelling, especially for hydropower tunnels. The reason is that during the tunneling works, existing clay may gradually dry out. The potential stability problem can then be seriously underestimated as the dry clay often has relatively high strength and it is often nearly impossible to distinguish swelling materials from non-swelling materials. When the tunnel later is filled with water, swelling may start and rock falls and slides may occur (Nilsen and Thidemann, 1993; Nilsen and Palmström, 2000). The swelling potential is dependent on several factors, such as amount and type of swelling minerals, amount and type of mobile cations, degree of consolidation of the material, access to water and degree of unloading after excavation (Nilsen and Palmström, 2000).

3.4 Rock stresses

The rock mass is unique as a construction material in the way that it is preloaded by in-situ stresses. Excavation in the rock mass will disturb and redistribute these pre-existing stresses in the vicinity of the underground opening (Hoek and Brown, 1980). In some cases, the induced stresses around the excavation may exceed the strength of the rock mass, resulting in rock failure and instability problems. In jointed rock mass may instabilities also occur if the stress level is too low and the normal forces acting on the joint surfaces are reduced (Nilsen and Palmström, 2000). Knowledge of the magnitudes and directions of the in-situ stresses and the induced stresses is therefore essential in the design and stability analysis of any underground excavation.

3.4.1 In-situ stresses in rock mass

From an engineering geological perspective it is the magnitudes and directions of the *principal stresses* that are of interest. According to Nilsen and Palmström (2000) the initial stress state in the rock mass is generally the resultant of the following components:

- *Gravitational stresses* – a result of gravity alone
- *Tectonic stresses* – mainly caused plate tectonics
- *Topographic stresses* – caused by surface topography
- *Residual stresses* – locked in stresses in the rock material from earlier stages of its geological history

The contribution from each of these components to the in-situ stress is difficult to determine. To evaluate the stress situation, the total stress can directly be measured by use of a stress cell, or estimated from topography, overburden and knowledge of the general stress conditions in the region (Nilsen and Palmström, 2000).

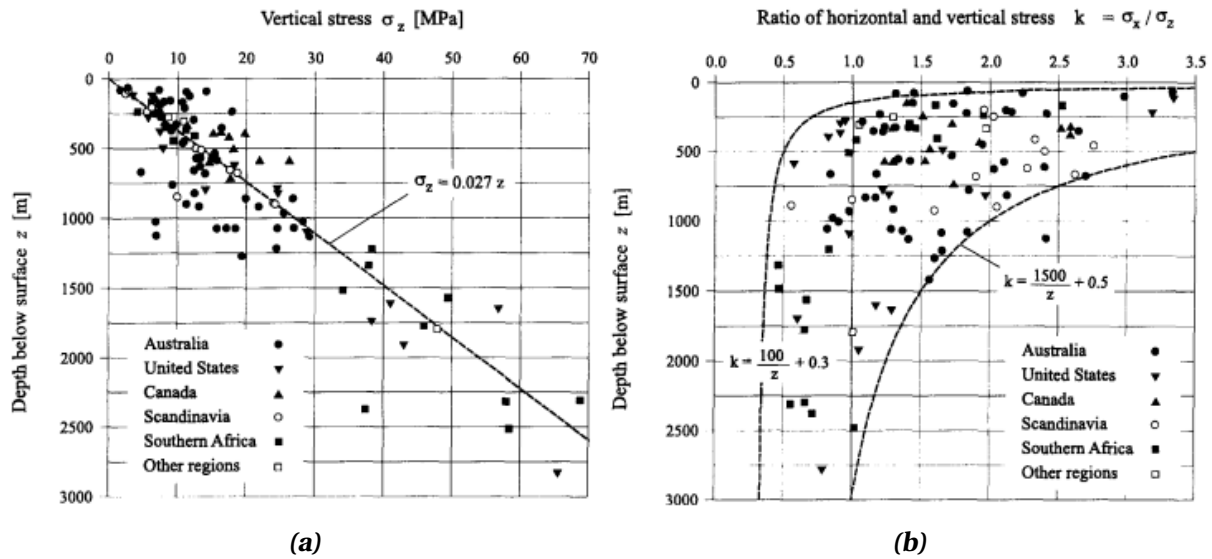


Figure 3.10: (a) Measured vertical stresses as a function of depth below surface, and (b) corresponding variation of horizontal-to-vertical stress ratio k . From Carranza-Torres and Fairhurst (2000), after Hoek and Brown (1980).

Vertical and horizontal stresses

The simplest directional component to estimate is usually the vertical stress. The magnitude of the vertical stress is normally given by the weight of the vertical rock column above the point of evaluation. This is expressed as follows:

$$\sigma_v = \gamma z \quad (3.11)$$

where σ_v is the vertical stress, γ is the unit weight of the overlaying rock mass (usually in the range of 20 to 30 kN/m³) and z is the depth below surface. Figure 3.10a show measurements of the vertical stresses, from underground construction and mining sites around the world, plotted against the depth. Although there is a significant amount of scatter, the figure indicates that the relationship of Equation (3.11) is a fair prediction (Hoek, 2007).

The horizontal stresses are more difficult to estimate. Often is the average horizontal stress assumed to be proportional to the total vertical stress:

$$\sigma_h = k \sigma_v = k \gamma z \quad (3.12)$$

Here σ_h is the horizontal stress, and k is the ratio of the average horizontal stress to the vertical stress. For a gravitational loaded rock, with no lateral strain, the factor k can be expressed as $k = \nu / (1 - \nu)$, where ν is the Poisson's ratio of the rock mass. However, this is seldom an accurate approach. Hoek and Brown (1980) plotted values of the factor k from

several measurements around the world, against depth below surface. The plot seen in Figure 3.10b, indicates that k tends to be high at shallow depths, while it decreases towards larger depths.

It is important to keep in mind that the plotted σ_h is the *average* measured horizontal stress, and that the horizontal stresses in different directions are seldom equal. These differences are probably due to topographic effects or local geological features (Hoek, 2007). In addition will tectonic stresses cause significant differences between the horizontal stresses. Hoek and Brown (1980) explain that a number of measurements from the Caledonian mountain range in Norway is not included in the plot, as these measurements are highly influenced by both topography and tectonic movements, showing a σ_h/σ_v -ratio that varies from zero to approximately 10. These large variations emphasize the difficulties to predict in-situ horizontal stresses from simple theoretical relationships. Hence, several authors underline the importance of carrying out stress measurements ahead of any underground excavation project (Nilsen and Thidemann, 1993).

3.4.2 Rock stresses surrounding a tunnel

When an excavation is made in the rock mass, the pre-existing stresses are disturbed and redistributed around the periphery of the excavation. The new induced stresses will depend on the magnitudes and directions of the principal stresses and the geometry of the opening (Nilsen and Palmström, 2000). Since the tunnel at Brattset is a circular TBM tunnel, only stress distribution around circular openings will be discussed.

In an isotropic rock mass the magnitude of the induced stresses around a circular opening is given by the *Kirsch Equations*. In an *isostatic* stress field ($\sigma_1 = \sigma_2 = \sigma$), the stresses around a circular opening depend on the distance from the excavation surface, and the magnitude of the tangential and radial stresses are given by:

$$\sigma_r = \sigma \left(1 - \frac{r^2}{R^2} \right) \quad (3.13)$$

$$\sigma_\theta = \sigma \left(1 + \frac{r^2}{R^2} \right) \quad (3.14)$$

where a is the radius of the circular opening, R is the distance from the circle centre (Li, 2015a).

The stress trajectories in Figure 3.11 show how the stresses are redistributed around the circular opening for an elastic material in isostatic stress conditions. At the excavation boundary it is shown that the tangential stress is twice the principal stress, while the radial stress is zero. Away from the boundary the stresses normalize, as the ratio R/r increases.

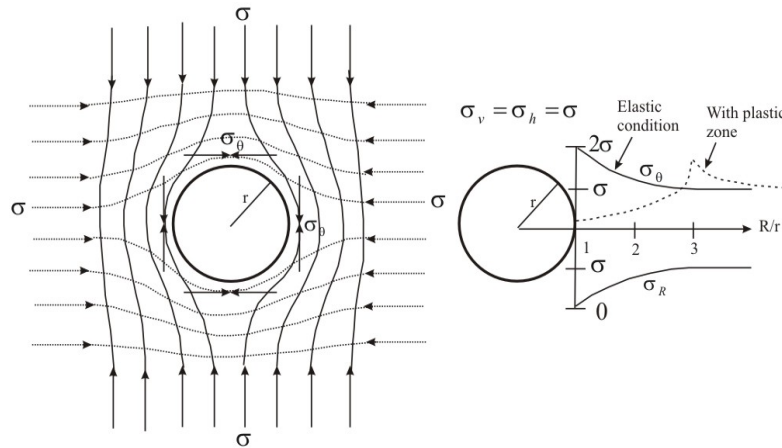


Figure 3.11: Stress distribution around a circular opening. Stress trajectories in rock mass (left) and tangential and radial stress distribution for elastic and non-elastic conditions (right) (Panthi, 2006).

As discussed, the in-situ stresses are rarely equal in all directions. The tangential stress will therefore vary around the periphery of the circular opening. According to Kirsch solution, the tangential stress reaches its maximum value $\sigma_{\theta max}$ where the σ_1 direction is tangent to the contour, and its minimal value $\sigma_{\theta min}$ where the σ_2 direction is tangent to the contour. The relation between the principal stresses and extremal tangential stresses expressed as follows:

$$\sigma_{\theta max} = 3\sigma_1 - \sigma_2 \quad (3.15)$$

$$\sigma_{\theta min} = 3\sigma_2 - \sigma_1 \quad (3.16)$$

According to Panthi (2006) the Equations (3.13) to (3.16) are only valid for homogeneous, isotropic and elastic rock mass, with widely spaced or tight joints. For weak anisotropic rocks, the tangential stresses will cause cracking and jointing close to the contour and the development of a plastic zone. The rock mass capacity to transfer stresses is reduced in this zone, causing the maximal stress to be moved further from the contour to where the elastic zone is reached. This is illustrated with the dotted line in Figure 3.11 (Panthi, 2006).

3.5 Significance of water

The excavation and operation of a hydropower tunnel will change the hydrogeological conditions of the area. In an unlined tunnel the joints of the rock mass are directly in contact with water that flow through the tunnel system. After filling of the water tunnels, the surrounding rock mass will become saturated. With high pressure tunnels and shafts there will also be possibilities for leakage and erosion of joints.

3.5.1 Hydraulic conductivity of rock mass

Hydraulic conductivity, also known as the coefficient of permeability, is the most common parameter for characterizing hydrogeological conditions. The conductivity of rock masses is mainly controlled by the degree of jointing and the character of the joints. Interlinked joint sets that have large aperture and are open or filled with permeable materials, have high hydraulic conductivity (Panthi, 2006). At depth there is a general reduction of joint aperture and an increase in joint spacing. As a result the conductivity decreases with depth below surface, as shown in Figure 3.12 (Nilsen and Palmström, 2000).

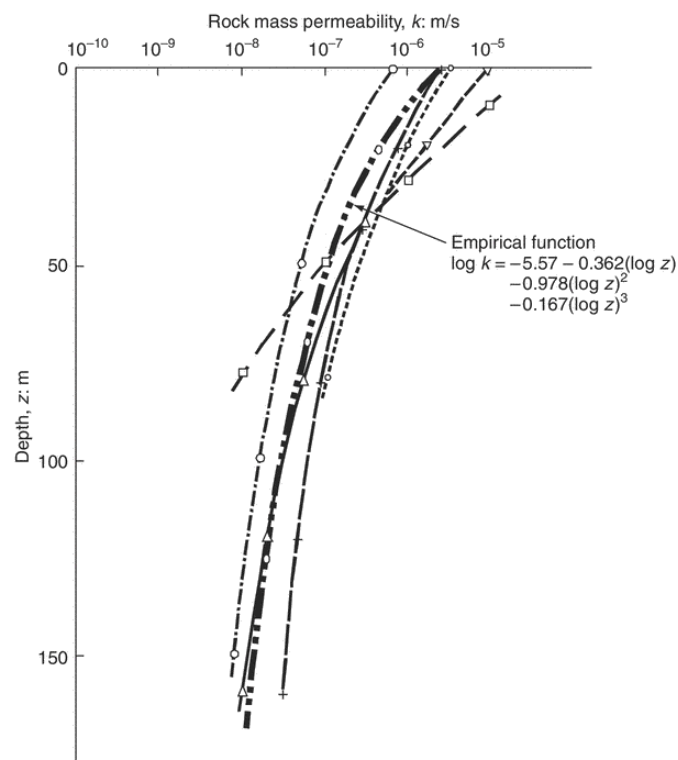


Figure 3.12: Hydraulic conductivity as a function of depth for Swedish test sites in Precambrian rocks (Palmström and Stille, 2015)

3.5.2 Effect of saturation upon rock mass strength and stiffness

The effect of an increase in water content on the rock strength and stiffness has been extensively studied over the years. The presence of water tends to reduce rock strength, a process also known as water-weakening (Wasantha and Ranjith, 2014). The weakening is a result of one or a combination of two effects: 1) mechanical effects, involving decrease of effective strength of the rock mass due to pore water pressure, leading to reduced internal friction and fracture strength (Goodman, 1989; Broch, 1979), and 2) chemical effects, related to the reduction of surface energy between the rock grains when they are in contact with water (Wasantha and Ranjith, 2014; Broch, 1979).

The influence of water on the rock mass strength is considerable, but due to large variations in texture and lithology of rocks, the extent of weakening effect among different rocks is highly varying. The strength reduction due to water is more significant in sedimentary rocks than in most igneous and metamorphic rocks. (Hadizadeh and Law, 1991) reported test results spanning from nearly insignificant reduction of the uniaxial compressive strength in quartzites, to 55 % reduction of strength in sandstones. Other studies have shown up to 90 % strength reduction shales in the most extreme cases (Wong et al., 2016). In a compilation of numerical results from several studies, Wong et al. (2016) found that measured reduction on Young's modulus E varies between less than 20 % for sandstones, around 50 % for shales and as high as 90-100 % for mudstones.

Broch (1979) observed a reduction of the point load strength index for different rock types, as presented in Figure 3.13. The figure indicates that fine-grained, nonporous rocks show little or insignificant changes, while the mica schist, a metamorphic and foliated rock type, shows a loss in point load strength varying between 40-70 %. The test results also reveal two mineralogical/petrographical features concerning the strength reduction of the different rock types (not including the nonporous rocks)(Broch, 1979):

1. The strength reduction increases with increasing amount of dark minerals, such as biotite, amphiboles and pyroxenes. In particular may biotite be of special importance
2. The strength reduction increases with increasing development of schistosity and anisotropy, such as from granites via gneisses to mica schist

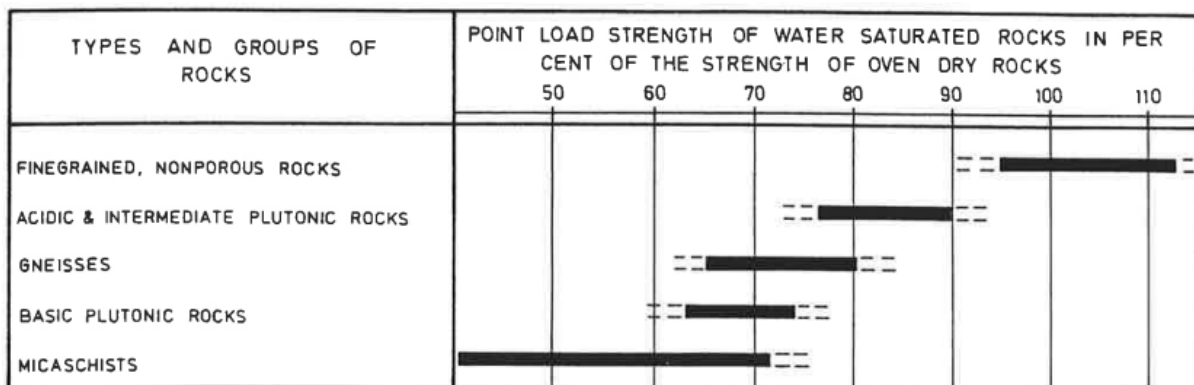


Figure 3.13: Changes in point load strength due to water saturation of various rock types (Broch, 1979)

Chapter 4

Instability issues in tunnels and underground caverns

4.1 Introduction

According to Nilsen and Palmström (2000), the rock mass is composed of rock blocks and fragments separated by discontinuities. Together these elements form a material whose properties are defined by their arrangement inside the rock mass, joint characteristics and possible joint filling. The orientation of an excavation in relation to rock mass structures, jointing, weakness zones and stress directions, have together with water conditions and stress magnitudes, major influence on the types and degree of instability problems that may occur (Nilsen and Broch, 2012).

Instability mechanisms in underground openings can basically be divided into two main groups. These are described by Hudson and Harrison (1997) and by Nilsen and Palmström (2000) as the following:

1. *Structurally controlled mechanisms*: Pre-existing blocks and fragments formed by discontinuities in the rock mass fall from the excavation periphery as a result of the excavation work. This includes a wide variety of mechanisms, such as block fall and sliding, loosening, raveling etc.
2. *Stress-controlled mechanisms*: When induced stresses around the excavation opening locally exceeds the rock mass strength. Failure may occur in the two main forms:
 - (a) Overstressing of *massive intact rock*. This may take place as spalling, popping, rockburst etc. in hard, brittle rocks and as squeezing in ductile, deformable rocks.
 - (b) Overstressing of *particulate materials*. This would be heavily jointed rocks, where squeezing or creep could occur.

4.2 Structurally controlled failure

Structurally controlled failures involve falling or sliding of pre-existing blocks in the rock mass into the tunnel. The blocks are formed by intersecting discontinuities in the rock mass, such as joints and bedding planes, and the free surface of the excavation opening (Hoek, 2007). The weight of the block or wedge is the driving force as the failure progresses, while the orientation of discontinuities in the rock mass relative to the tunnel contour is determining the shape and volume (Nilsen and Palmström, 2000), see Figure 4.1. The stability is mainly determined by the dip angles and the frictional conditions along the discontinuity planes that define the block, as well as the tangential stresses near the opening (Li, 2015a). The tangential stress has an interlocking effect on the discrete blocks in the rock mass, increasing the frictional resistance. Hence, in excavations at shallow depths, where stresses are low, failure are often entirely controlled by the discontinuities in the rock mass rather than the strength of the intact rock (Hoek, 2007).

Hoek (2007) demonstrates the importance of stabilizing identified blocks or wedges. Unless measures are taken to support loose wedges in the tunnel, the failure can develop rapidly. For each block falling or sliding, the interlocking and restraining forces around the opening reduce, allowing other blocks to fall. The failure process will not stop until natural arching in the rock mass is preventing further unravelling or until the opening is full of fallen material. The first block failing, allowing other blocks that were previously restrained to follow, is often termed as a *key block* (Goodman and Shi, 1985).

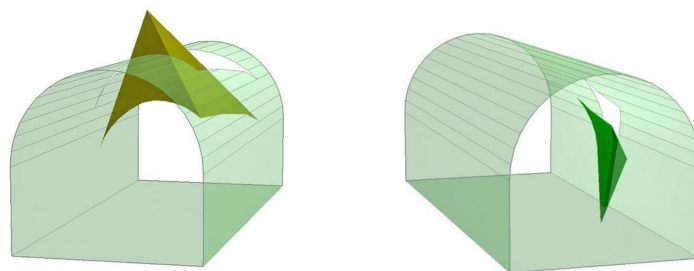


Figure 4.1: Block fall from roof (left) and sliding from sidewall (right) (Hoek, 2007)

4.3 Stress-controlled failure

Stress-controlled failures are initiated when induced stresses around the excavation locally exceeds the rock mass strength. As discussed in Chapter 3, redistribution of the in-situ stresses around the opening contour creates areas of stress concentration, which can cause overstressing of the rock mass. Stress induced instabilities may appear in two ways: 1) rock spalling or rock burst and 2) tunnel squeezing or deformation (Panthi, 2006). The first way is

likely to take place in massive, brittle rock, while the latter is related to heavily jointed rock mass or ductile, deformable rocks. While there are observations of rock spalling/bursting in the headrace tunnel of Brattset HPP, squeezing has not been an issue there and will not be further discussed.

4.3.1 Failure mechanisms in brittle rock mass

Several definitions of the term "rockburst" can be found in the literature. Hoek (2007) defines rock burst as "explosive failures of rock which occur when very high stress concentrations are induced around underground openings". He notes that the problem is particularly acute in deep level underground mining in hard brittle rock. Ortlepp and Stacey (1994) use the source of energy to define the failure mechanism, explaining rockburst as "the damage that occurs in a tunnel as a result of a seismic event, or which is directly associated with a seismic event". Diederichs (2014) divide the "seismic event" into three categories with associated damage:

1. Rock bulking due to fracturing
2. Rock ejection due to seismic energy transfer
3. Rockfalls induced by seismic shaking.

The first mechanism is most commonly observed, and is associated with sudden stress-induced failure at the tunnel perimeter with violent bulking, and in some cases with explosive ejection of rock fragments. This type of burst is by Ortlepp and Stacey (1994) referred to as *strainburst*, and is the mechanism that Hoek (2007) describes. According to Ortlepp and Stacey (1994) strainburst may take place at field stress as low as 15 % of the rock uniaxial compressive strength. Seismically induced rock burst (2. and 3.) are with few exceptions relevant only for deep mines, where very high stresses are present.

Strainburst is caused by fractures developing parallel to the tunnel contour, in the direction of the major tangential stress (Nilsen and Palmström, 2000). This may result in superficial spalling or rock bulking, with violent ejection of plate formed fragments, as illustrated in Figure 4.2. The rock fragments are usually thin with very sharp edges, see Figure 4.3, and the release volumes of each event are normally small (Ortlepp and Stacey, 1994; Diederichs, 2014). Spalling can develop without release until a buckling instability take place, releasing larger volumes (Figure 4.4b). If the developing spall fractures interact with an existing structure in the rock mass, a structurally controlled strainburst occur as illustrated in Figure 4.4c. Finally, if spalling slabs are restrained while the fracturing propagates into the rock mass, the combined dilation of the numerous fractures can lead to a sudden failure and release (Diederichs, 2014).

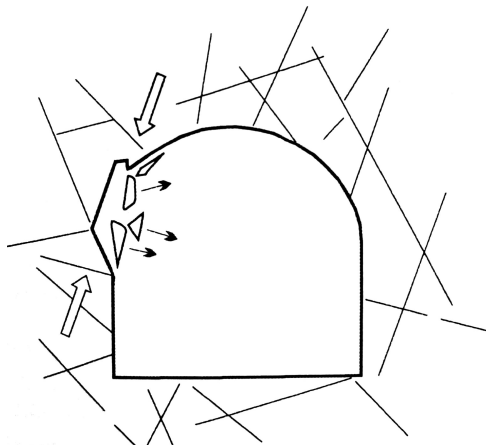


Figure 4.2: Strainburst: violent spalling resulting from locally stress concentration at contour (Ortlepp and Stacey, 1994)

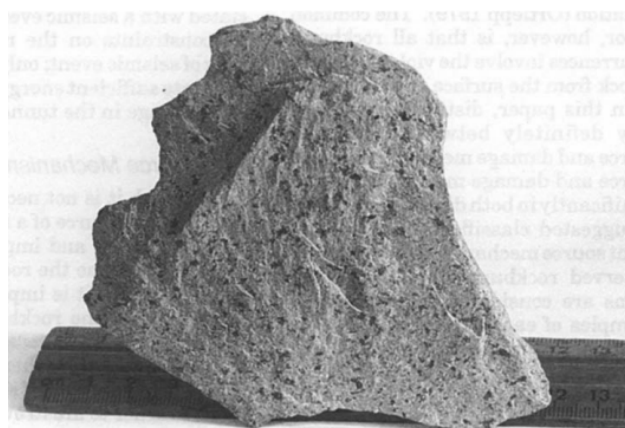


Figure 4.3: Fragment of andesitic rock from tunnel strainburst showing typical sharp edges and flaky slenderness (Ortlepp and Stacey, 1994)

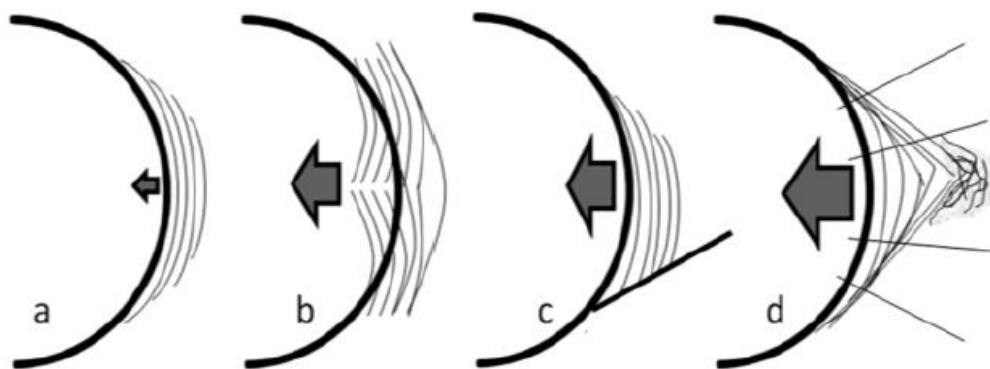


Figure 4.4: Increasing severity of stress induced failure in brittle rock mass. From non-violent spalling (a) to bursting through buckling (b), intersection with structure (c) and dilational yield (d) (Diederichs, 2014).

4.4 Failure in faults and weakness zones

Faults and weakness zones differentiate from the surrounding rock mass, with a structure, composition and properties that can be completely different from the adjacent rock mass. Weakness zones and faults may contain material that is altered by hydrothermal activity and other geological processes. The character of the gouge or filling material is an important factor that may have major impact of the stability of the zone. Problems associated with such zones are for instance flowing and running ground, swelling pressures and high water inflow (Nilsen and Palmström, 2000). According to Nilsen and Broch (2012), gouge filled weakness zones are one of the most common causes of instability problems in underground excavations in Norway. They further point out that the most severe instability problems are normally caused by zones containing swelling minerals.

The extent of the affected area is determined by the width of the weakness zone and its orientation relative to the tunnel alignment (Mao et al., 2011). Generally, a small angle between the zone and the tunnel wall will give a larger affected area, compared to a zone which is orientated perpendicularly to the tunnel axis. The effect of different strike and dip angles of a weakness zone illustrated in Figure 4.5. In addition will the access of water, frequency of such zones, competence of the side rock and the dimension of the tunnel be important factors when considering the stability of the tunnel and the necessary support measures for the weakness zone (Mao et al., 2011).

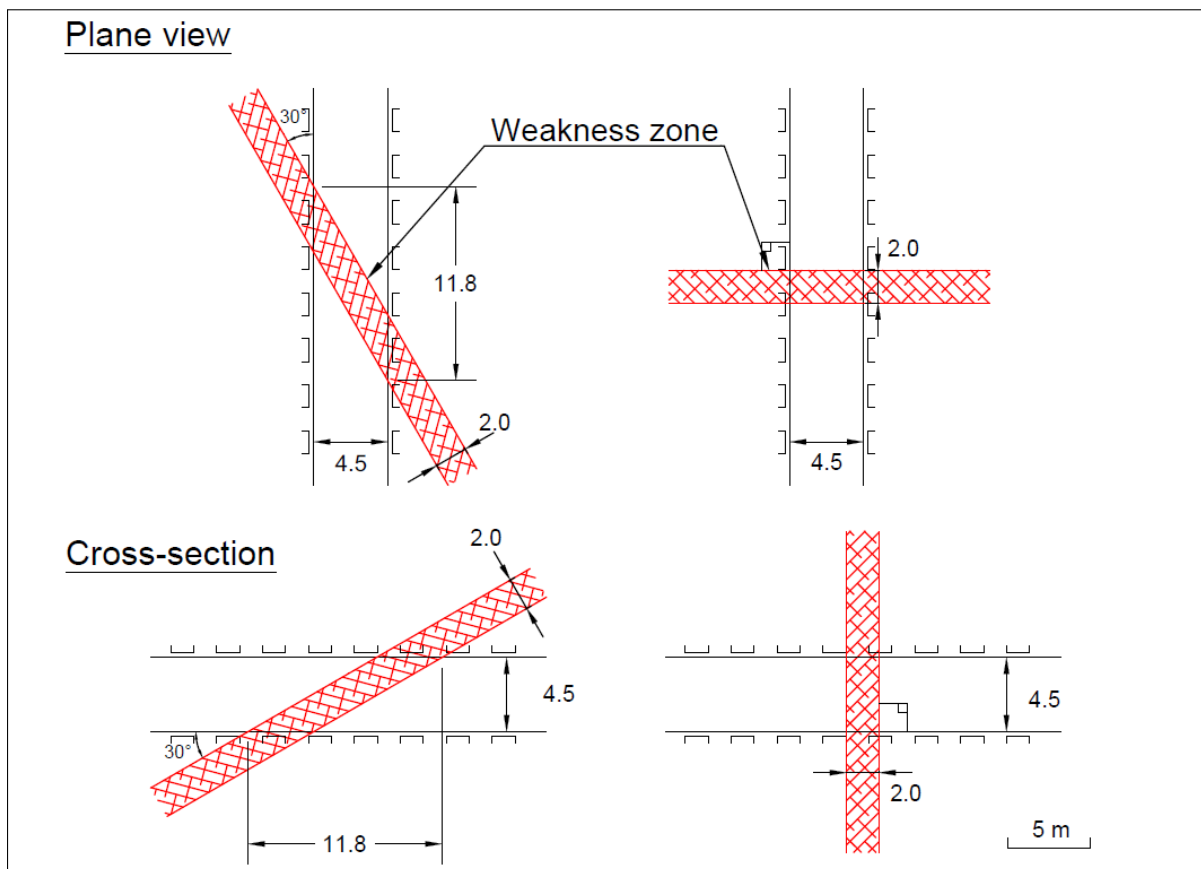


Figure 4.5: Effect of weakness zone orientation: A weakness zone that intersects the tunnel at a small angle (left) will affect a longer section of the tunnel than a zone that intersects at a large angle (right).

4.4.1 Swelling process and potential

ISRM (1975a) defines the swelling mechanism as "a combination of physico-chemical reaction involving water and stress-relief" and where "the physico-chemical reaction with water is usually the major contributor but it can only take place simultaneously with, or following, stress relief." Swelling clays are mainly from the group of smectites, a mineral group where sheet minerals such as montmorillonite, vermiculite and mixed-layer swelling minerals are

most common. These secondary minerals are often found in gouge fillings, and are usually originated from the alteration of in-situ rock forming minerals or from solution deposits (Selmer-Olsen and Palmström, 1989). The difference between swelling minerals and non-swelling minerals are illustrated in Figure 4.6, where the swelling particles have the ability to take up a release water in accordance to the external pressure they are subjected to.

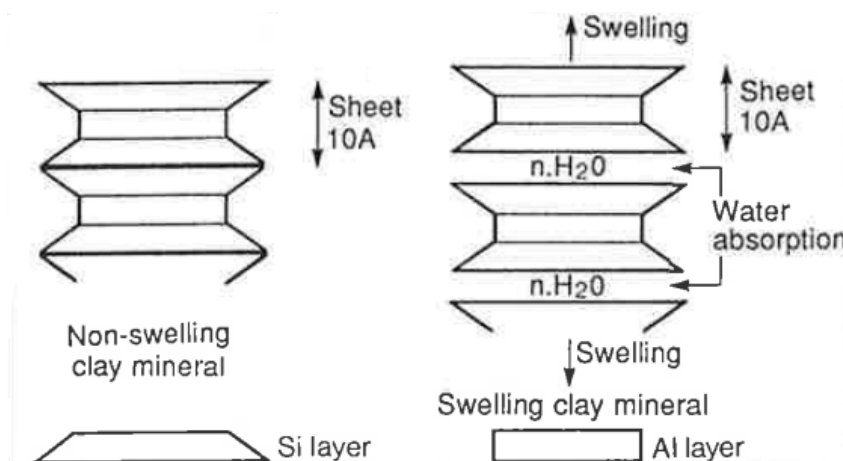


Figure 4.6: Structural difference between swelling and non-swelling minerals. The length is given in Angström, $1\text{A} = 10^{-7}\text{mm}$ (Selmer-Olsen and Palmström, 1989).

The swelling process may be divided into two stages: hydration and osmotic swelling. During hydration water molecules, due to their dipole moment, are adsorbed at the exterior surface of the clay particles. The swelling of this first stage can lead to a 100% volume increase of dry material. In the osmotic stage, the swelling is caused by water molecules taken up at the internal surfaces due to a higher concentration of ions here (Nilsen and Broch, 2012). The degree of swelling largely depends on the interparticle distance of the clay particles and the intraparticle distance between the expandable layers of the mineral, as well as the amount of clay particles and expandable layers (ISRM, 1975a).

Several methods can be used to determine the swelling potential, such as XRD analysis, free swelling test and tests of the swelling pressure test in the laboratory. The tests are performed on fine grained material and give a measure of the *swelling potential* (Nilsen and Broch, 2012). Measurements of swelling potential from different underground sites in Norway, are summarized in Table 4.1. Although swelling properties can be measured in the laboratory, the in-situ conditions are as well as important as the swelling potential of the material. The degree of consolidation of the material, the access to water and the degree of unloading after excavation will determine for the *in-situ swelling pressure* that can develop (Nilsen and Broch, 2012; Selmer-Olsen and Palmström, 1989).

Table 4.1: Measured swelling properties of fault clay in Norwegian tunnels. From Nilsen and Palmström (2000) and Nilsen and Broch (2012).

Project	% material < 20 μm	Free swelling %	Swelling pressure MPa
Sira-Kvina (Duge) hydropower plant	2	170	1.76
Rafnes water transfer tunnel	23	232	1.05
Rana hydropower plant	-	200	1.04
Øvre Otra (Ormsa) hydropower plant	5	195	0.95
Hjartøy sub-sea tunnel	10	450	0.95
Åbjøra (Trøndelag) hydropower plant	13	210	0.89
Ormsetfoss hp. plant (transfer tunnel)	10	167	0.62
Oslofjord sub-sea tunnel	34	167	0.55
Ormsetfoss hp. plant (headrace tunnel)	46	125	0.34
Nye Osa hydropower plant	12	140	0.30
Hanekleiv road tunnel	14	150	0.18

Chapter 5

Hydraulic transients in the waterway system

Since the change in the operational scheme of power plants the recent years, start-and-stop cycles has become more frequent. This has resulted in more unsteady flow in the waterway system, in form of hydraulic transients that arise from change in water discharge. To get an understanding of how these transients may affect the unlined shafts and tunnels, some basic theory will be reviewed in this chapter.

5.1 Hydraulic transients

During continuous operation of a hydroelectric power plant, the water flow in the waterway system is steady. A reduction or increase of the water discharge, such as closing or opening of valves, will cause unsteady motions. The transition from a steady flow regime to another are referred to as *hydraulic transient regimes* (Popescu et al., 2003).

Hydraulic transients can be divided into two categories, based on the different types of motions (Popescu et al., 2003):

- Water hammer: An elastic wave of rapidly varied motion, with large amplitudes and frequencies. The wave is largely influenced by the fluid compressibility.
- Mass oscillations: Slowly varied motion, with small amplitudes and frequencies. The mass transfer in the system is important. The elastic effects are negligible and the water can be treated as an incompressive solid.

The two phenomena may be treated separately as the period of the water hammer waves is much shorter than for the mass oscillations. This involves that the water hammer wave is already dampened out at the time the mass oscillations are starting to develop in the system (Guttormsen, 2006).

5.2 Water hammer

Water hammer is the pressure wave which occur due to a sudden change in discharge, such as opening or closing of a valve or start-up/shut-down of a pump or turbine (Popescu et al., 2003). In the closing of a valve, the kinetic energy in the flowing water is transformed to potential energy when the water velocity is reduced. The potential energy takes form as a rise in pressure and a pressure wave that travels rapidly in the waterway system (Guttormsen, 2006). The waves of positive and negative pressure are reflected at the end of the tunnel or at other free water surfaces in the system, and will travel back and forth until they are dampened out by friction (Munoz-Hernandez et al., 2013). The water hammer intensity is a function of the length of the pipeline (Jaeger, 1977). If the pipeline is relatively short, the pressure wave will return before the valve is fully closed and the pressure rise will be reduced (Guttormsen, 2006).

Water hammer may cause serious damage to turbines, valves and the waterway system. To reduce the damage potential of the pressure wave, the pressure amplitude needs to be minimized. This can be done in two different ways: 1) by increasing the time of regulation, or 2) by reducing the travel length of the wave. The first option may be unacceptable based on the requirements made to the regulation system (Guttormsen, 2006). Hence, the second option is the most practical, and can be solved by introducing a free water surface close to the regulation valve. This will involve the installation of a surge tank (or an air cushion chamber, which has the same function), with the purpose of reducing the reflection time compared to the valve closing time (Jaeger, 1977).

An infinitely large surge tank would reflect the pressure waves completely and retain a constant water level. In practice, a surge tank is limited in size, and the changes in flow velocity will always set up mass oscillations and the pressure waves will only be partially reflected (Jaeger, 1977).

5.3 Mass oscillations

With the introduction of a surge tank to reduce the water hammer intensity, the problem of mass oscillations occurs. While water hammer appears in the penstock only, mass oscillations are slow variations in the water flow in the pressure tunnel and surge tank (Popescu et al., 2003).

The development of mass oscillations are illustrated in Figure 5.1. The figure shows the first upsurge and down surge after fully closure of the valves. Before closure, the water discharge Q is constant and the system is in a steady state (a). The water level difference z_0 is due to headloss. When the regulation valves close, the water velocity drops to zero in the penstock

and the water flowing from the reservoir is forced up the surge tank (b). The water will rise in the surge tank until all the kinetic energy is transformed into potential energy, and the water masses accelerate back towards the reservoir (c). The oscillations have long periodicity and can be compared to the oscillations in communicating vessels. However, since the reservoir is much larger than the surge tank, the amplitude of oscillations in the reservoir becomes negligibly small compared to the oscillation in the narrow surge tank (Jaeger, 1977).

The oscillations will continue back and forth between the surge tank and the reservoir until they are dampened out by friction, usually within minutes (Guttormsen, 2006). Mass oscillations will also arise from valve opening. In this situation the first wave in the surge tank is a downsurge wave (Guttormsen, 2006). It should also be noted that the principle explained here is similar for cases with air cushion chamber (Popescu et al., 2003).

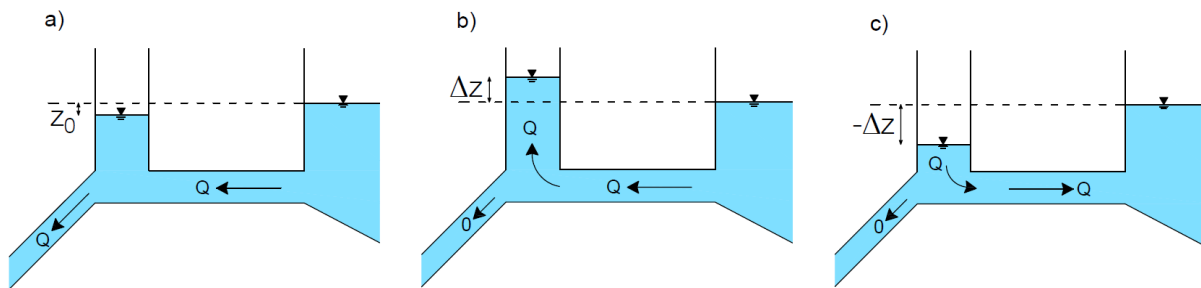


Figure 5.1: Principle drawing of mass oscillations in surge tank. Reproduced from Rasten (2014).

5.4 Pressure period and amplitude

The periods and amplitudes of the pressure fluctuations that develop from hydraulic transients can be estimated through simplified equations. These equations will be presented here. For further details and derivation of the equations, the reader is referred to literature, e.g. Guttormsen (2006) and Tuseth (2013).

The time it takes for the pressure wave of the water hammer to travel back and forth between the closing valve and the free water surface is called the reflection time, and is given by:

$$t_r = \frac{2L}{a} \quad (5.1)$$

where L is the length of the tunnel between the wave and surge tank or air cushion chamber, and a is the propagation speed of the wave. The period of the wave equals two times the reflection time:

$$T = 2 t_r = \frac{4L}{a} \quad (5.2)$$

As mentioned, the water hammer pressure is dependent of the valve closing time and the length between the valve and free water surface. If the valve closing time T_L is longer than the reflection time t_r , the maximum pressure amplitude can be calculated as follows:

$$\Delta h = \frac{a\Delta v}{g} \frac{2L}{a T_L} = 2 \frac{L}{g A_T} \frac{\Delta Q}{T_L} \quad \text{if } T_L > \frac{2L}{a} \quad (5.3)$$

where

- Δh = maximum amplitude water hammer
- a = pressure propagation speed
- g = acceleration of gravity
- Δv = change in water velocity
- L = distance between free water surface and valve
- A_T = tunnel cross sectional area
- T_L = valve closing time
- ΔQ = change in discharge

To reduce the water hammer effect at Brattset there is installed an air cushion chamber. However, the equations for estimating mass oscillations are in principle valid for surge tanks only. In order to calculate oscillation in a system with air cushion chamber an equivalent area A_{eq} is introduced. And by substituting the shaft area by A_{eq} , all surge shaft equations are valid. The equivalent area is given by:

$$A_{eq} = \frac{1}{\frac{1}{A_0} + \frac{nh_{p0}}{V_0}} \quad (5.4)$$

where A_0 is the area of the water surface inside the air cushion chamber, n is the polytropic index (normally 1.4 for air), h_{p0} is absolute air pressure in meter water head and V_0 is the air volume. Further, the maximum amplitude of mass oscillation is calculated from:

$$\Delta z = \Delta Q \sqrt{\frac{L/A_T}{g A_{eq}}} \quad (5.5)$$

where L the tunnel length between the air cushion chamber and the reservoir. Finally, the period of mass oscillations are given by:

$$T = 2\pi \sqrt{\frac{L A_{eq}}{g A_T}} \quad (5.6)$$

The presented equations ignore any effects of headloss. According to Guttormsen (2006) the reduction of the upsurge height due to friction is $\frac{1}{3}h_f$, where h_f is the headloss in meters. The effect is even less on downsurge. The friction along the tunnel at Brattset should be small, since the main part is drilled by TBM, which results in smooth tunnel walls. From Figure D.4, the gross head at highest reservoir level is calculated to be 272 m (519 - 247). T. H. Landløpet in TrønderEnergi Kraft AS stated in an email (22. May 2018) that no measurements for the headloss have been done at Brattset. In a report from calculations for the concrete plug just downstream the air cushion chamber, he had found that the water head at the plug was 267.21 m, indicating a headloss of 4.79 m. Since this is such a small amount (< 2 %), the given estimates should therefore be accurate enough for their purpose in this study. The value of headloss will however be used when calculating the air pressure inside the air cushion chamber in Chapter 9.

5.5 Effects of hydraulic transients on waterway systems

According to Helwig (1987), the transient water pressure surges due to water hammer are of such short duration that they will have minimal effect on the pore pressure within the rock mass, and not increase the risk of hydraulic jacking. The effects of mass oscillations are however not as well studied, and very little information can be found in literature. Bråteveit et al. (2016) carried out a series of inspections of unlined tunnels that is subjected to the new production pattern of increased frequencies of start-and-stop cycles (called "hydropeaking" in their paper). They concluded that the frequency of rock falls in unlined tunnels has increased with a factor of 3.4, and that costs related to head losses due to rock falls in the tunnel system have increased by 70 %. In accordance with findings presented by Thidemann and Bruland (1992), they also found that major rock falls are most frequently appearing in or near weakness zones containing swelling clay.

The tendencies to an increase in the number of instability issues after changes in the production pattern, have led to the belief that the mass oscillations may be slow enough for an increased pressure to develop inside the joints of the rock mass. The possible effect of this will be further studied in this thesis, through both analytical and numerical methods.

5.6 Hydraulic transients at Brattset HPP

The magnitudes of pressure fluctuations inside the tunnel system due to water hammer and mass oscillations are important input for the stability assessments. Using the equations presented above, the pressure amplitudes and periods are here calculated for the maximum change in discharge, assuming a *valve closure time of 7 seconds*. All necessary geometrical

parameters are summarized in Table 5.1 and the estimated amplitudes and periods are given in Table 5.2. It should be noted that these calculations are simplified, and does not consider any friction losses along the waterways. However, according to Guttormsen (2006), these estimates should still give values within an accuracy of 10 %.

Table 5.1: Dimensions of tunnels and air cushion chamber (AC)

Parameter	Description	Value	Source
T_L	Valve closing time	7 s	–
ΔQ	Maximum change in discharge	36 m ³ /s	Figure D.4
$L_{downstream}$	Tunnel length AC to turbine	400 m	(Broch, 2000)
$L_{upstream}$	Tunnel length AC to reservoir	16 827 m	Figure D.4
A_T	Tunnel cross sectional area	7/25/16/15.9 m ²	Figure D.4
A_0	Water surface area AC	900 m ²	Figure D.4
V_0	Air volume AC	7000 m ³	Figure D.4
h_{p0}	Absolute air pressure	247.74 m	Eq. (5.10)
A_{eq}	Equivalent area AC	19.7 m ²	Eq. (5.11)

5.6.1 Calculations of water hammer wave

According to Guttormsen (2006) the propagation velocity in tunnels has been measured to approximately 1200 m/s. Given the length $L = 400$ m, the water hammer period is:

$$T = \frac{4L}{a} = \frac{4 \cdot 400}{1200} = 1.33 \text{ s} \quad (5.7)$$

The tunnel area downstream the air cushion chamber is 25 m² for 355 m, while the last 45 m of steel penstock has a cross sectional area of 7 m². Assuming a valve closure time T_L of 7 s, the water hammer amplitude is calculated to be:

$$\Delta h = 2 \frac{L}{g A_T} \frac{\Delta Q}{T_L} = \frac{2}{9.81} \left(\frac{355}{25} + \frac{45}{7} \right) \frac{36}{7} = 21.6 \text{ m} \quad (5.8)$$

5.6.2 Calculation of mass oscillations

Also upstream the AC the cross-sectional area of the tunnel varies. In the headrace tunnel from the reservoir is the cross sectional area 15.9 m², in the pressure shaft 16 m² and in the pressure tunnel 25 m². The corresponding lengths are 15 891 m, 212 m and 679 m respectively. The weighted length - area ratio is calculated as follows:

$$\sum L/A_T = \frac{15891}{15.9} + \frac{212}{16} + \frac{724}{25} = 1039.8 \text{ m}^{-1} \quad (5.9)$$

The air pressure inside the air cushion chamber (AC) is given by the water level difference between the reservoir and water surface in the chamber and the headloss. Since the pressure is absolute, the atmospheric pressure, which is equivalent to 10.33 m, should also be included (Tuseth, 2013). The highest regulated water level at the reservoir is at el.519, and it is calculated that the water surface inside the AC is at el. 276.48, and the headloss is assumed to be 4.79 m. Thus, the absolute pressure is:

$$p_{h0} = 519 - 276.48 - 4.79 + 10.33 = 247.74 \text{ m} \quad (5.10)$$

The equivalent area of the AC is:

$$A_{eq} = \frac{1}{\frac{1}{A_0} + \frac{nh_{p0}}{V_0}} = \frac{1}{\frac{1}{900} + \frac{1.4 \cdot 247.74}{7000}} = 19.7 \text{ m}^2 \quad (5.11)$$

The maximum amplitude of the mass oscillations is:

$$\Delta z = \Delta Q \sqrt{\frac{L/A_T}{g A_{eq}}} = 36 \sqrt{\frac{1039.8}{9.81 \cdot 19.7}} = 83.5 \text{ m} \quad (5.12)$$

And the period is:

$$T = 2\pi \sqrt{\frac{L}{g} \frac{A_{eq}}{A_T}} = 2\pi \sqrt{1039.7 \frac{19.7}{9.81}} = 287 \text{ s} \approx 4.8 \text{ min} \quad (5.13)$$

The amplitude and period of the mass oscillations are illustrated in Figure 5.2. The peak-to-peak amplitude is the maximum pressure difference between upsurge and downsurge, and is assumed to be $2\Delta z = 167 \text{ m}$. Due to friction along the tunnel the oscillations will be dampened out after some time. Since just the maximum amplitudes are of interest here, it is not attempted to calculate the dampening due to friction.

Table 5.2: Estimated amplitudes and periods of water hammer and mass oscillations. Valve closing time $T_L = 7 \text{ s}$

	Water hammer	Mass oscillations
Maximum amplitude Δz	21.6 m	83.5 m
Equivalent rise in water pressure	0.21 MPa	0.82 MPa
Period T	1.33 s	287 s

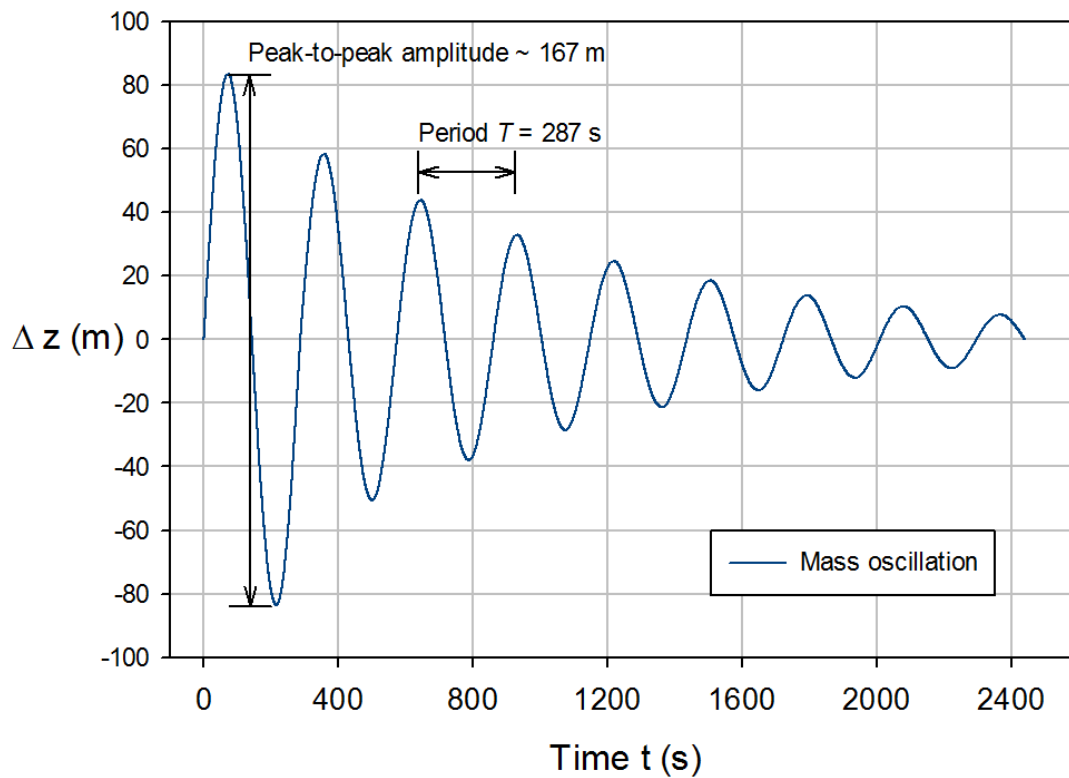


Figure 5.2: The peak-to-peak amplitude and period of calculated mass oscillations. The dampening factor is arbitrary, and is just added to the plot for illustrative reasons.

Chapter 6

Review of cases

To highlight the importance of long-term stability of hydropower tunnel systems, two cases of tunnel collapses will be reviewed in this chapter. The first is from Svandalsflona Hydropower Project, where a shaft collapse caused by failure in a weakness zone occurred after more than 30 years of operation. The second case that will be described is the collapse of Glendoe headrace tunnel in 2009, where failure of a weakness zone happened barely months after the power plant began operating.

6.1 Collapse of Svandalsflona pressure shaft

After collapse in a weakness zone in May 2008, inspections of the waterway system and removal of slide deposits from the shaft bottom took place from middle April to early May 2009. After removing considerable amounts of loose material on 8 May, a sudden burst flood came down the shaft on 9 May, resulting in the loss of two workers life. The reasons for this event will not be further discussed here, but are thoroughly described in Panthi (2014a). In relation to long-term stability of waterway systems, the reasons for the shaft collapse in 2008 are of great interest.

6.1.1 Project description and geology

The lay-out and the geological conditions of Svandalflona hydropower project (HPP) are described by Panthi (2014a). The Svandalsflona HPP is located in Hordaland county in Western Norway. It is a part of the Røldal/Suldal hydropower development scheme, which was developed in the 1970s. The scheme utilizes a reservoir capacity of about 830 m³ to generate 2757 GWh annually. Svandalsflona HPP came in operation in 1978, and has an installed capacity of 20 MW and a yearly production of 36 GWh. Three small lakes are utilized as reservoirs: vestre (west) Middy, østre (east) Middy and Stutakvelven lakes. Stutakvelven

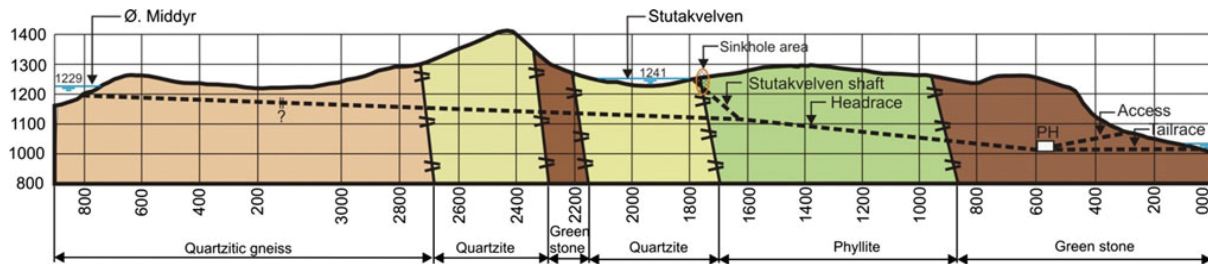


Figure 6.1: Longitudinal profile of the geology and the waterway system at Svandalsflona hydropower project. The weakness zone intersecting Stutakvelven shaft and the location of the sinkhole are indicated (Panthi, 2014a).

lake reservoir also function as a surge shaft, and is connected to the headrace tunnel with a 45° inclined shaft.

The geology in the area is complex. The project is situated mainly within three different geological formations. These are: (1) Precambrian basement (older than 700 million years), (2) Cambro-Silurian basement (between 350-570 mill. years old) and (3) overthrust nappes from the Caledonian orogeny (approx. 350 million years old). The geological set-up relative to the waterway system is illustrated in Figure 6.1. The underground powerhouse, access tunnel, tailrace tunnel and the downstream part of the headrace tunnel is situated within Precambrian greenstone and green schist. The middle part of the headrace tunnel, where also the Stutakvelven reservoir and shaft is located, passes through schistose phyllite and quartzite of the Cambro-Silurian basement rock and a small band of greenstone. The upper part of the headrace tunnel is aligned within quartzitic gneiss of the overthrust nappes rocks.

6.1.2 Rock mass conditions and support

The rock mass in the area is fractured due to the overthrusting activity, and a number of clay-filled fracture (weakness) zones with thickness less than 1 m were observed during tunnel inspection in 2009. At the time of construction major weakness zones were stabilized by full concrete lining, while low density bolting and occasional unreinforced and mesh-reinforced shotcrete were applied to satisfy stability where blocky and poor rock mass existed. The rest of the headrace tunnel were left unlined, in accordance with the traditional Norwegian support philosophy (Panthi, 2014a).

As indicated in Figure 6.1, a boundary weakness zone, separating quartzite and phyllite, outcrop close to the Stutakvelven reservoir. Panthi (2014a) describe the zone as highly fractured, made up of cubic-like rock material mixed with clay, silt and sand. The material had very low frictional and cohesion properties, and was highly permeable. This would lead to very low self-supporting capacity of the rock mass in the weakness zone. The weakness zone was

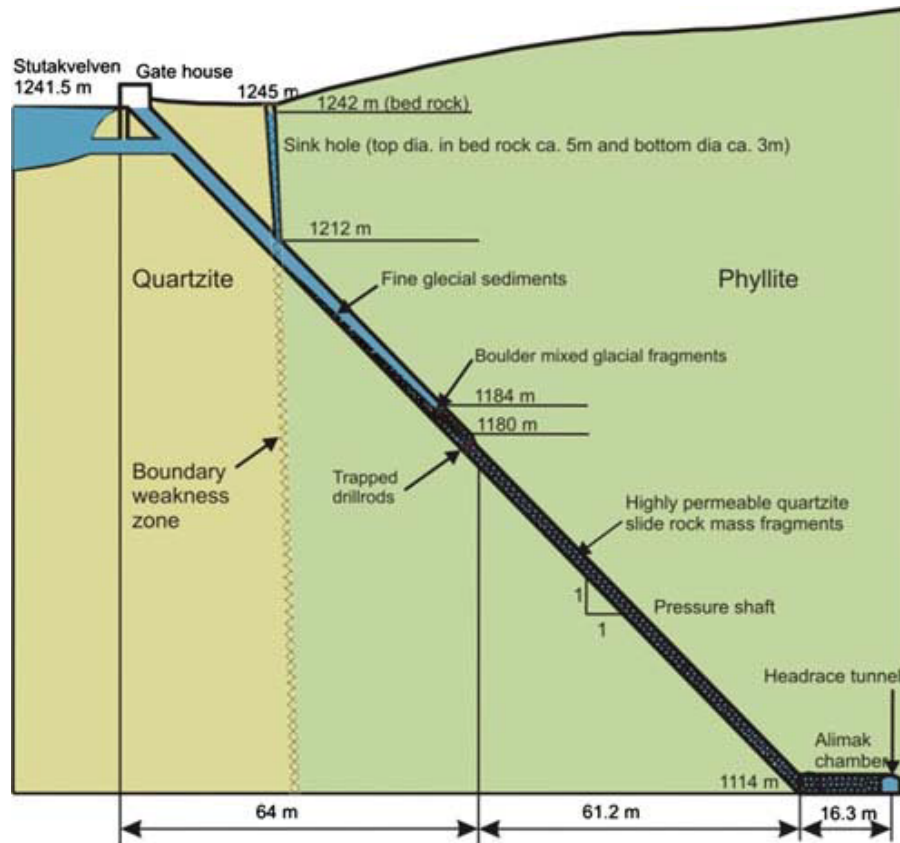


Figure 6.2: Assumed conditions at Stutakvelven inclined shaft after rock slide at weakness zone (Panthi, 2014a).

causing challenges during excavation of the inclined shaft. Initially the shaft was excavated from bottom up by raise climber. But as the weakness zone was encountered, this turned out to be difficult due to safety hazard and problems with securing the zone. The last 40 m of the shaft was then excavated from top to bottom, using traditional shaft sinking method. The weakness zone was permanently supported by concrete lining in the side wall and roof. In addition, the concrete walls were braced with concrete bracing beams.

6.1.3 Failure of weakness zone

In late May 2008, after almost 30 years of successful operation, a major rock fall appeared in the boundary weakness zone. This resulted in collapse of the inclined shaft and a sinkhole reaching up to the surface (see Figure 6.2). The rock mass fragments from the weakness zone and slide deposits from the upper part of the sinkhole caused blockage of the shaft and an abnormal water level at the Stutakvelven reservoir.

The weakness zone was supported by concrete lining, but as Panthi (2014a) points out, the lining quality was obviously not as good as what is expected for concrete lining installed with today's tunneling technology. As discussed, the rock mass in the weakness zone was

highly fractured and of very poor quality. In addition, the constant water flow through the shaft during production had caused saturation and weakening of frictional and cohesion properties. After almost 30 years of operation, the pressure from the extremely weak rock mass behind the applied lining became too high, leading to the failure.

6.2 Glendoe headrace tunnel collapse

Glendoe hydropower scheme is located near Fort Augustus, at the south west end of Loch Ness, in Scotland. Scottish & Southern Energy (SSE) is the owner of the project. The contractor joint venture was led by Hochtief and Pöyry was included as sub-contractor for the design of the civil works (Reynolds, 2017). The project was constructed between 2006 and 2008, and was the biggest hydroelectric scheme built in Scotland for many years (Wallis, 2009).

In August 2009, only eighth months after takeover, the plant was forced to shut down as a collapse had occurred in the main tunnel. SSE was anxious to start remedial works as soon as possible, since they were losing substantial amounts of revenue while the scheme was out of operation. In the discussions with the contractor, Hochtief, they were however unable to reach agreement. The main issue was liability, and which party to be responsible for the cost of repairs (Conacher, 2017). SSE then instructed another contractor to undertake the repair works, which included a bypass around the failed section. The works proved more expensive and took much longer than expected. The scheme was out of operation for three years, before it began producing electricity again in August 2012. SSE then brought a £130 million claim against Hochtief. Hearings proceeded for several years and in late December 2016 a court ruling was issued in favor for Hochtief (Reynolds, 2017).



Figure 6.3: Layout of the Glendoe hydropower scheme (Wallis, 2009)

Thorough description of the project and the course of events can be found in the full judgment of *SSE Generation Limited v. Hochtief Solutions AG & Another* (2016, CSOH 177) (hereafter referred to as "SSE v. H. 2016").

6.2.1 Project description

Glendoe hydropower scheme is designed to have an annually electricity production of 180 GWh. The net head is between 600 m and 606 m, and the scheme normally achieves its maximum output of 100 MW at 80 % valve opening. This is in part depending on the reservoir water level. The intention of Glendoe was to quickly generate electricity to cover peak periods of demand, and SSE expected the scheme to run for 20 % of the year (SSE v. H. 2016).

The layout of the Glendoe hydropower scheme is shown in Figure 6.3. Drill and blast was used for excavation of the underground powerhouse, access tunnel and a 7 km long aqueduct tunnel, while the tailrace tunnel and the 6.2 km headrace tunnel was mainly excavated by a 5 m diameter TBM. The headrace tunnel was designed with a steep inclination of almost 12 %, replacing the more common pressure shaft between a gentle headrace and lower tunnels (Wallis, 2009).



Figure 6.4: TBM excavation of the unlined headrace tunnel at Glendoe (Reynolds, 2017)

6.2.2 Rock mass conditions and support

The project is situated in an area of metamorphosed sedimentary rocks consisting of interbedded quartzites, quartz schists and quartz mica schists that are folded and sheared. The rock cover above the tunnels varies between 250 m and 350 m, and the anticipated strengths of the rocks range largely between 130 MPa and 150 Mpa (Wallis, 2009). The Barton Q-system was used for rock mass classification and as a reference for support design and measures (Reynolds, 2017). According to Conacher (2017), the engineering geology consultant expected 97.5 % of the rock to be "good" but warned that information was limited. One particular fault zone was identified during the pre-investigations, called the Congleann Fault Zone (CFZ), where poorer rock conditions were expected (Reynolds, 2017).

During the TBM excavation works, the rock conditions was reported as being dry and good, with very few weak sections. Even when boring through the CFZ area no particular challenges were encountered and the working crew reported barely noticing the fault (Conacher, 2017). From the beginning it was expected little groundwater, which also was confirmed during inspection of the tunnel after excavation. In SSE v. H. 2016 professor emeritus Einar Broch (NTNU), who inspected the headrace tunnel, is cited:

"My general impression was that the rock mass conditions in the tunnel are very good. It is one of the driest tunnels that I have ever inspected ... No major weakness zones were observed ... The weakness zones described in the Pöyry report are all small, and as far as I could observe, none of these may cause serious collapses. I thus regard the support measures recommended in the report as being more than good enough for a tunnel that is basically designed and built as unlined."

Broch had also taken samples at selected locations to check for swelling minerals. However, the tests did not indicate any potential problems (SSE v. H. 2016). Most of the headrace tunnel was left unlined, except from a steel lined section near the power station, a section of reinforced concrete to resist dewatering problems and support in form of shotcrete and rock bolts in various areas (SSE v. H. 2016).

6.2.3 Tunnel collapse

In early summer 2009 the operators detected odd water levels and power readings in the power plant. However, the operators assumed this was caused by calibration problems due to the newness of the site. The odd readings and low output of the turbines continued during the summer, and in early August sediment plumes were noticed discharged into Loch Ness. On 5 August the plant could not even reach 100 MW. The operating personnel decided to

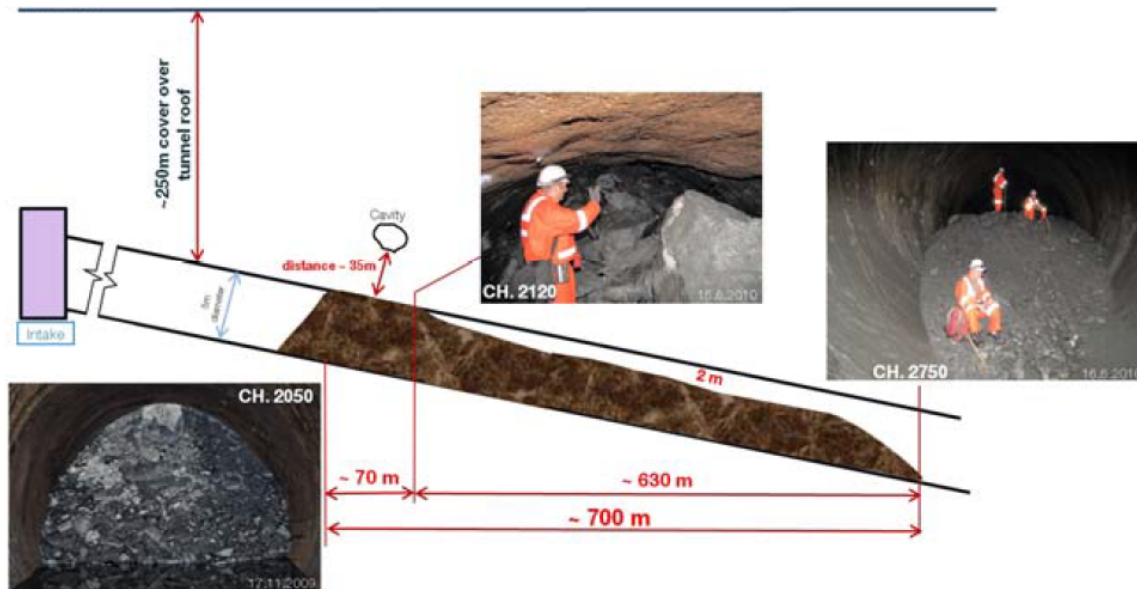


Figure 6.5: Illustration of assumed damage after collapse (not to scale). From Broch (2017).

shut down the turbines, followed by dewatering of the waterway system and an inspection. A major rock fall was detected on the walk through of the tunnel, approximately 2 km downstream the reservoir intake (see Figure 6.5). The rock debris had fallen from a breach in the crown, completely blocking the tunnel (SSE v. H. 2016).

In the court ruling it is judged that the reason for the collapse was "poor rock conditions coincided with insufficient shotcrete and rockbolts" (SSE v. H. 2016). It is further explained that the weak rock mass in the fault zone started to deteriorate after submersion, leading to reduction of strength and stability. The water would also wash out erodible rock and open up larger seams in the rock mass. As indicated in Figure 6.5, the eroded material was deposited over a significant length of the headrace tunnel. Finally, the tunnel lost stability and collapsed. The blocked zone had an extent of 71 m, and the collapse had developed progressively from at least 12 April 2009 (Conacher, 2017).

6.3 Lessons learned from case studies

According to Panthi (2014a), most of the collapses along hydropower waterway systems seen in the last decade happened during operation, i.e. at full hydrostatic pressure. The construction of unlined waterway tunnels and the over-time operation change the engineering geological conditions of the rock mass. At Svandalsflona the high permeability of the weakness zone allowed water to flow from the pressure shaft and through the weak rock mass. With pressure oscillations due to fluctuating production pattern, the water could possibly flow back and forth within the weakness zone, and over time cause significant reduction in the frictional and cohesional properties of the material.

In SSE v. H. 2016, the weakening of the rock mass in the Congleann Fault Zone is considered to be a result of a "slaking" process that developed as the rock mass was submerged into water. Palmström and Stille (2015) define slaking as the deterioration and breakdown of the rock due to hydration and changes in temperature. The process can cause cracking and heaving, and will greatly alter the mechanical properties of the rock mass. In the long term, this may dramatically influence the behaviour and stability. Additionally, the high water velocity and pressure within the tunnel could have washed out erodible rock mass, opening up larger seams and thus contributed to the failure (SSE v. H. 2016).

The examples provided in this chapter illustrate the importance of geological investigations and careful interpretation of the geological conditions, in all stages of the design process. Uncareful judgment about the stability conditions or compromises in the support measures may result in tunnel collapses and cause severe consequences, including large economic losses, contractual disputes and serious accidents.

Chapter 7

Brattset Hydropower Project

7.1 Project description

Brattset Hydropower Project (Battset HPP) is situated in Rennebu municipality in Sør-Trøndelag county, approximately 70 km south of Trondheim. Brattset began operating in 1982 and have an annual production of 402 GWh (NVE, 2017). It is one of five hydropower projects developed by KVO (Kraftverkene i Orkla) in the Orkla River, indicated in Figure 7.2. KVO is owned by Statkraft (48,6 %), TrønderEnergi Kraft (35 %), Eidsiva (12 %) and Nord Østerdal Kraftlag (4.4 %). The production is operated by TrønderEnergi from their office at Berkåk (TrønderEnergi, 2017).



Figure 7.1: The machine hall at Brattset HPP. Brattset is open to the public and take often in visitors. Here are students from Engineering Geology at NTNU getting a tour in the power-house area in 2016.



Figure 7.2: The five hydropower projects in Orkla. From south to north: Ulset, Litjfosse, Brattset, Grana and Svorkmo. Brattset HPP in the centre of the map, south of Berkåk. Modified from Kvaal and Wale (2000)

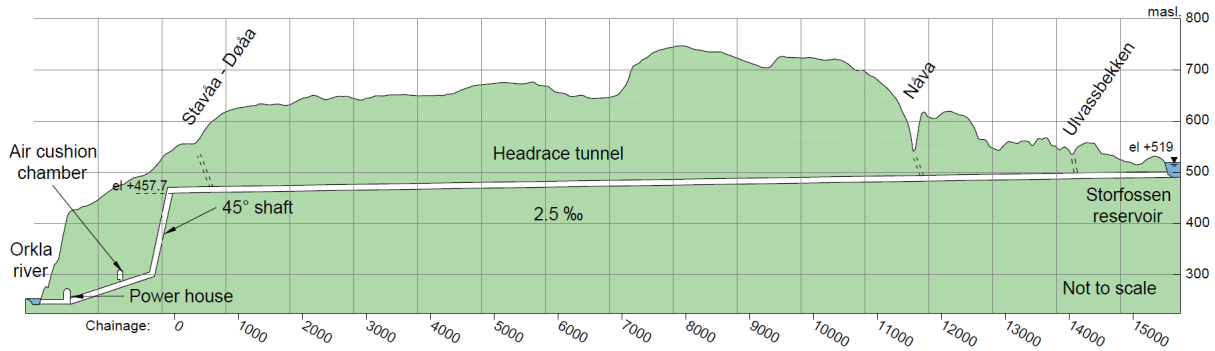


Figure 7.3: Longitudinal profile of the waterway system of Brattset hydropower project

7.2 Project layout

The Brattset HPP utilizes the 270 m river drop between the intake at Storfoss reservoir and the outlet at Brattset. The project layout is illustrated in Figure 7.3. The project consists of a headrace tunnel and tailrace tunnel, an inclined shaft and an underground powerhouse. Along the waterway the rivers Ulvassbekken, Nåva, Stavåa and Døåa are lead into the head-race tunnel through dams, shafts and tunnels.

7.2.1 Intake area

The intake is located in Orkla river, at the Storfoss reservoir. The Storfoss dam is a concrete buttress dam about 200 m wide and 25 m tall (measured from maps). The reservoir has a storage capacity of 1.7 million cubic meters, and the water elevation is regulated between 503 and 519 masl. (16 m) (TrønderEnergi, 2017).



Figure 7.4: The Storfoss dam and reservoir at the intake of Brattset HPP

7.2.2 Headrace tunnel

The headrace tunnel is 16.7 km, where about 15.2 km is full-face drilled by TBM with a diameter of 4.5 m (cross sectional area is 15.9 m²). The remaining excavation is done by drill and blast. The overburden varies between 100 and 230 m. From the intake at 497 masl. the headrace tunnel has a declination of 2.5 ‰ towards the sand trap at the top of the pressure shaft (Sjeggedal and Holter, 1998). The pressure shaft has an inclination of 45°. On the layout drawings the chainage numbering (ch.), in meters, starts at the top of the inclined shaft, increasing upstream. Two adit tunnels leads into the headrace tunnel: Skamfer adit at ch. 90 and Næverdal adit at ch. 12 330. The brook intakes of the smaller streams are located at the following chainages: Stavåa and Døåa at ch. 785; Nåva at ch. 11 845; Ulvassbekken at ch. 14 312.

7.2.3 Powerhouse area

The powerhouse area at Brattset consists of machine hall, transformation hall, penstock, sand trap, air cushion chamber, tailrace tunnel and access tunnels. The air cushion chamber has a volume of 9000 m³ and a storage pressure of 2.5 MPa (Broch, 2013). Two Francis turbines, each with an effect of 40 MW, are installed in the power plant. The water is discharged into the Orkla river through a 415 m long tailrace tunnel, where the water level is regulated between 244 and 247 masl.

7.3 Rock support

The headrace tunnel and the pressure shaft are unlined. According to Flønes (1982) the reason for choosing TBM as excavation method for the headrace tunnel was that it was estimated to reduce the construction time by 1/2 year and the need of rock support by 75 %. Flønes confirmed the estimations, and presented that as of 31.10.81, after 10 815 m of excavation, no bolting had been carried out from the TBMs yet, 4 zones and faults had been supported by steel sets and mesh and a few sections had been shotcreted. In total, approximately 15 % of the tunnel was supported, where only 1 % was installed at the face.

7.4 Engineering geological conditions

Engineering geological conditions along the headrace tunnel were studied during the Project work, through desk study and field work. An engineering geological map was produced and is presented in Appendix D, showing field locations and measurements. In the following section the findings from the study will be briefly presented.

7.4.1 Geological setting

Brattset HPP is situated in the Trondheim Nappe Complex in the central-southern part of the Scandinavian Caledonides. The Trondheim Nappe Complex is a part of Upper Allochthon which occur in a NE-SW trending depression in central parts of Trøndelag, and consist of late Cambrian to Ordovician rocks. The nappe complex as a whole, was thrust over the underlying nappes and basement rocks during Silurian time (Gee et al., 1985; Nilsen and Wolff, 1989). The rock types in the area are mainly phyllite and mica schist in the Gula Nappe, and green phyllite, tuffite, greenstone and amphibolite in the Støren Nappe. The igneous activity in the Caledonian mountain belt has led to several large intrusions in the area, appearing as plutons and dykes of trondhjemite and granodiorite. Looking at the Quaternary map from the project area in Figure 7.6, it is observed that the soil cover above the headrace tunnel consists generally very thin till deposits or the bedrock is exposed.

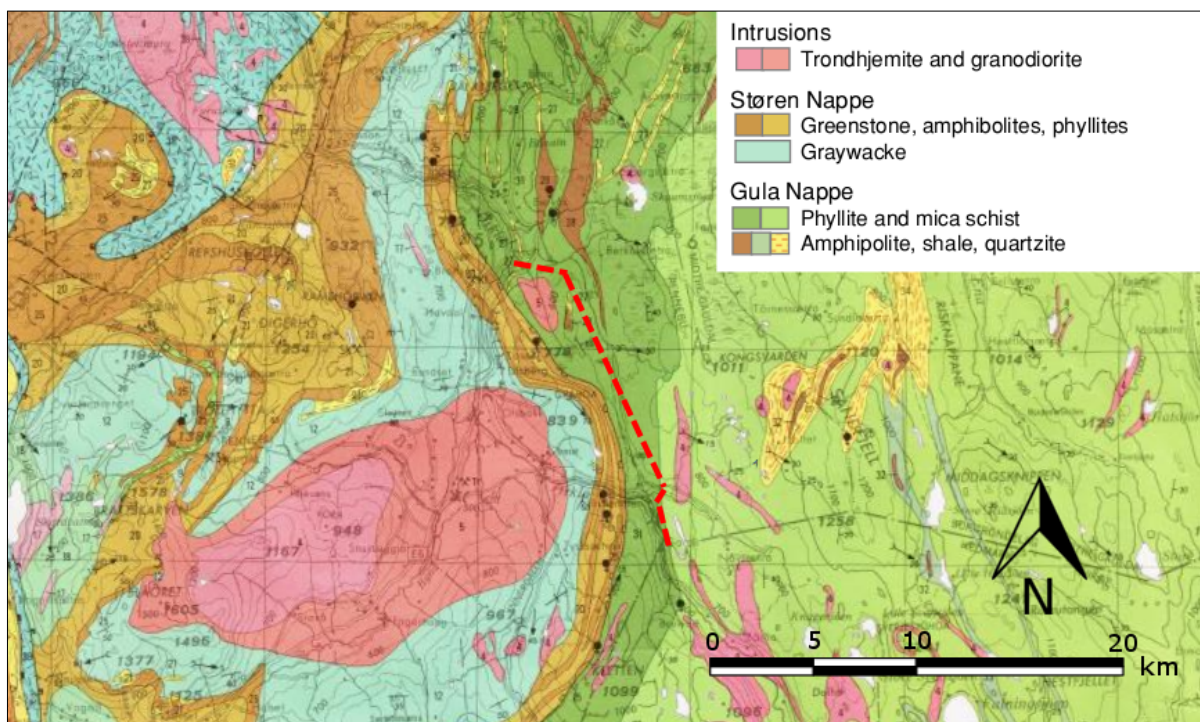


Figure 7.5: Geological map of project area. Brattset headrace tunnel (red dotted line) is situated in phyllite unit from the Gula Nappe, close to the border to the Støren Nappe. Modified from Nilsen and Wolff (1989).

7.4.2 Rock mass conditions

The headrace tunnel runs through a unit described as "gray phyllite, biotite phyllite and schist" by the bedrock map of Nilsen and Wolff (1989). During field work it was observed large variations in composition and structure of the phyllite. From a lightly colored quartzitic phyllite to a darker phyllite containing more chlorite. Since the area has been subjected to

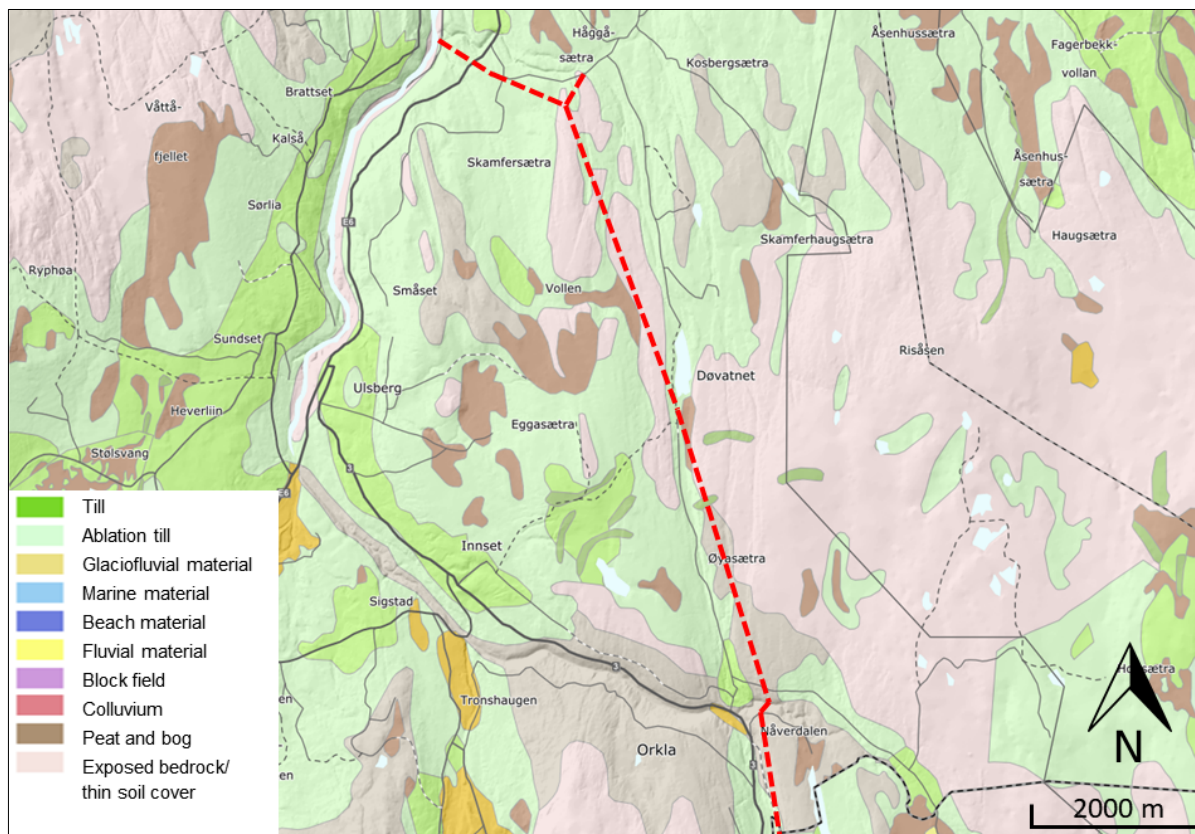


Figure 7.6: Quaternary geological map of project area. The soil cover along the headrace tunnel (red, dashed line) consists of exposed rock/thin soil cover and thin layer of ablation till. Modified from NGU (2018).

folding and faulting it is reasonable to expect alternating layers of the different compositions of phyllite along the tunnel alignment, and possibly intermediate variations. Along the headrace tunnel there was also observed extensive intrusions of quartz keratophyre within the phyllite.

Phyllite

The quartzitic phyllite is observed in road cuts at upper parts of the headrace tunnel, close to the intake at Storfossen (Figure 7.7). The rock mass has a light grey color and has a tightly held, distinct foliation. Quartz-filled veins and quartz lenses are observed following the foliation, together with small scale folding patterns. The rock mass seems to be medium strong to strong. Jointing varies from one set plus random joints to three joint sets. Foliation joints are developed along the foliation plane, forming the most prominent joint set with a spacing of 10-40 cm. These joints are rough and planar to undulating, with thin mineral filling. The most distinct tectonic joint set has smooth undulating surfaces with a joint spacing of 1-2 m. It is observed some chlorite filling in the joints, and close to the surface there are open joints with about 5 mm to 2 cm aperture.



Figure 7.7: Quartzitic phyllite at location 1, close to Storfossen intake



Figure 7.8: Phyllite with band of quartz keratophyre at location 3, close to Ulvassbekken

The darker colored phyllite is observed at the upper parts of the headrace tunnel, from Ulvassbekken and past the adit tunnel at Næverdalen, and at the brook intake of Stavåa-Døåa. Two joint set plus some random jointing are registered in the phyllite, where the most pronounced set is following the foliation plane. The joint spacing is generally 0.5-10 cm. Some surfaces show red colors from rust. At some sections the rock mass is very schistose, this is most likely due to volcanic activity. Dykes and sills of quartz keratophyre are penetrating the rock mass, and adjacent to these keratophyre bands the phyllite show an increased schistosity and is very weak.

The two subunits of phyllite have a distinct foliation, and the majority of joints are developed along this plane, see Table 7.1 and Figure 7.9. As seen in the rosette plot in Figure 7.10, the foliation runs parallel to the tunnel axis with moderate to steep dip angles, varying between 35-58°. Other joint sets are oriented at high angles to the foliation joints.

Table 7.1: Strike and dip mean values

Symbol	Structure	Unit	Strike (mean)	Dip (mean)	Quantity
▲	Foliation	Phyllite	N157°E	42°NE	12
◆	J1	Phyllite	N076°E	76°SE	2
◆	J2	Phyllite	N080°E	28°N	1
Total					15

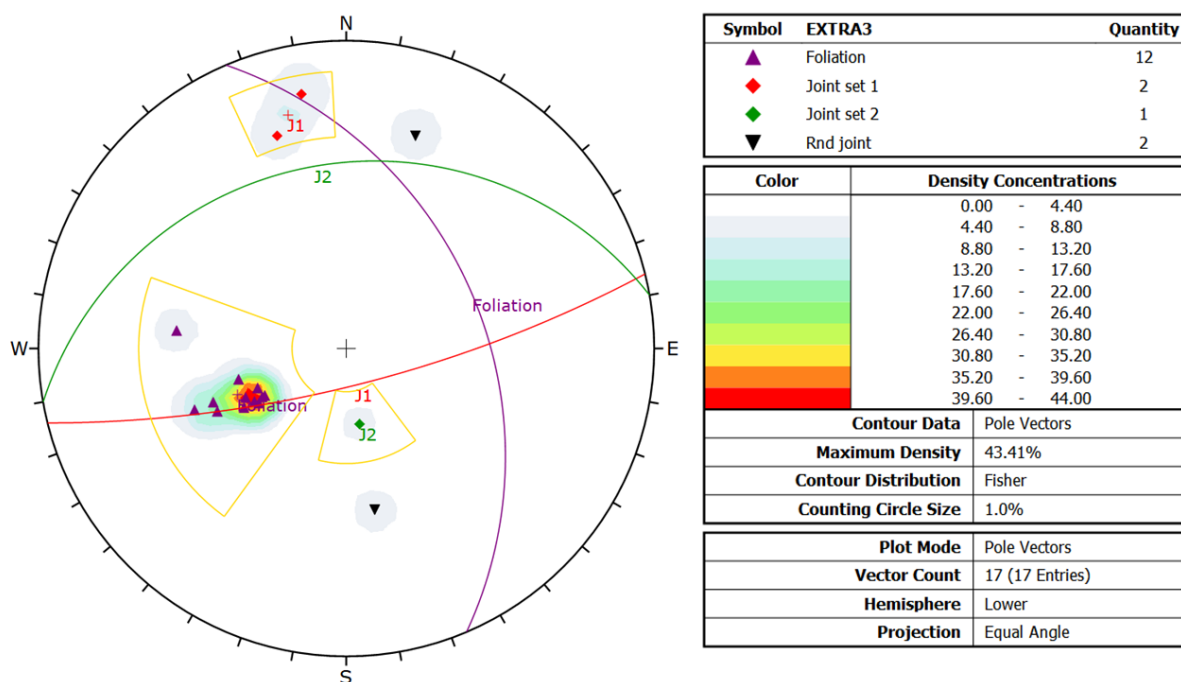


Figure 7.9: Stereonet plot of phyllite, showing poles to measured strikes and dips of foliation and joints, and the mean planes.

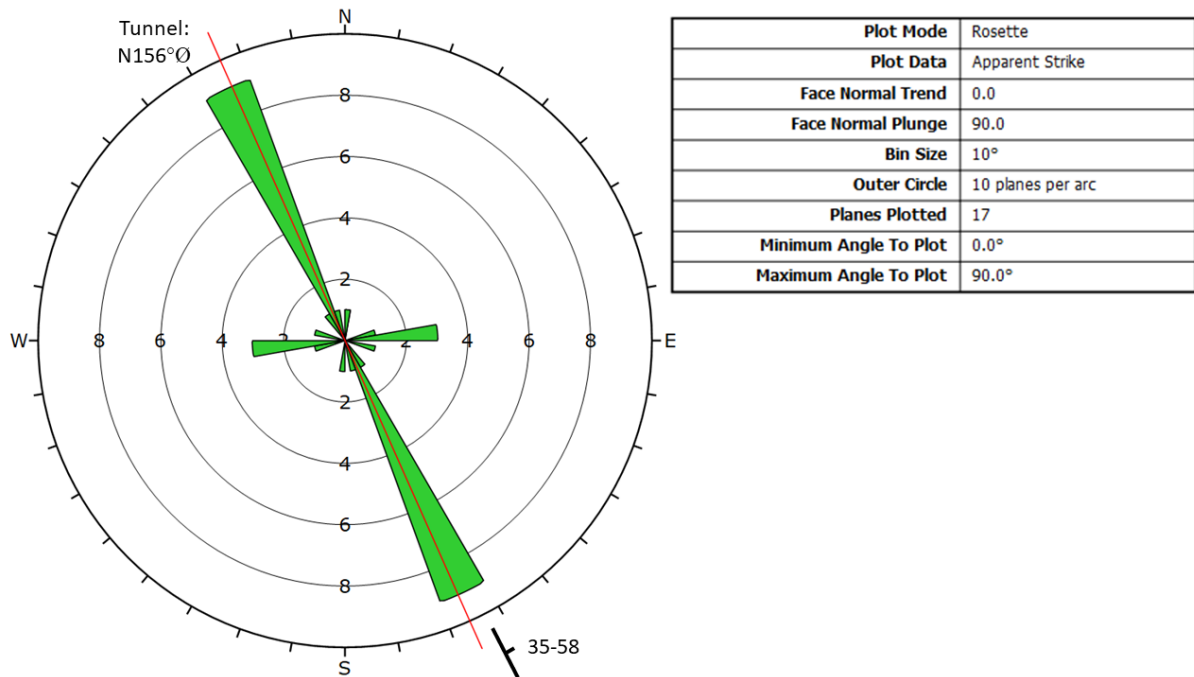


Figure 7.10: Rosette plot of phyllite. The tunnel alignment (red line) is approximately parallel to the strike of the foliation, which is the dominant structure.

Quartz keratophyre

Bands of quartz keratophyre are observed intruding the phyllite. This is a hydro-thermal altered felsic rock type. The rock mass is fine grained with a lightly gray color. The band thickness varies from 0.5-5 m. The quartz keratophyre is more brittle than the surrounding rock mass and shows a blocky structure (see Figure 7.11).



Figure 7.11: Large intrusion of quartz keratophyre at location 3, close to Ulvassbekken

7.4.3 Rock mass quality

There is a large number of rock mass classification systems that have been developed to serve as a tool in the design and support of underground excavations. Among the most frequently used systems are RQD, Q, RMR, RMi, NATM and GSI (Stille and Palmström, 2003). In Norwegian tunneling practice the Q-system is the most commonly applied system. The Q-system was developed at NGI (the Norwegian Geotechnical Institute) by Barton et al. (1974) between 1971-74, and has continuously been reviewed and updated by NGI. It classifies the rock mass with respect to stability in underground openings, and recommend rock support design (NGI, 2015).

The Q-value describes the quality of the rock mass, based on six parameters different parameters. These parameters can be determined by geological mapping in a tunnel or a cavern, or from field mapping or core logging. The numerical value of the index Q is calculated by Equation (7.1):

$$Q = \frac{RQD}{J_n} \cdot \frac{J_r}{J_a} \cdot \frac{J_w}{SRF} \quad (7.1)$$

where the 6 parameters are:

RQD = Degree of jointing (Rock Quality Designation)

J_n = Joint set number

J_r = Joint roughness number

J_a = Joint alteration number

J_w = Joint water reduction factor

SRF = Stress reduction factor

Each parameter is determined by using tables that gives numerical values based on the observed conditions. The calculated Q-value varies on a logarithmic scale from 0.001 to 1000, where high values indicate good stability and low values indicate poor stability (NGI, 2015). In pairs, the parameters describes the three most important factors for underground stability: $\frac{RQD}{J_n}$ describes the degree of jointing or block size; $\frac{J_r}{J_a}$ describes the joint friction, or inter-block shear strength; $\frac{J_w}{SRF}$ describes the active stress situation (NGI, 2015). Since geological formations are rarely homogeneous, determining the parameters as a range of values, rather than an accurate value, will often give a more correct classification. The Q-value would then be expressed as an interval (Nilsen and Palmström, 2000).

During the field work, Q-values were determined at exposed rock in road cuts. Two evaluations were done for the quartzitic phyllite and one evaluation each for the dark phyllite and the quartz keratophyre. Stress and water parameters were assumed for tunnel depth near the field location. Results are given in Table 7.2. Detailed notes from the assessment are given in Appendix B.

Table 7.2: *Q-value estimation of observed rock units*

Rock type	Quartzitic phyllite	Quartzitic phyllite	Q. keratophyre	Phyllite
Location	1	2	5	5
RQD	70	60-70	80	10
J_n	1	9	6	6
J_r	1.5	2	1.5	2
J_a	4	4	1	1
J_w	1	0.7-1	0.8	1
SRF	1	1	1	4
Q-value	26.3	2.3-3.9	16	3.3
Description	Good	Poor	Good	Poor

7.4.4 In-situ rock stresses

Measurements of the rock stresses have been carried out for the project during construction. Both 3D overcoring tests and hydraulic splitting test have been conducted (Hansen and Hanssen, 1988). The test results are presented in Table 7.3. The direction of the major principal stress in the project area could not be found in available literature. Hence, the indicated stress orientation in the stress map of Norway from Myrvang (2001) has been adopted. The assumed directions of the major and minor principal horizontal stresses and the tunnel alignment are shown in Figure 7.12.

Table 7.3: *Measured in-situ stresses and shut-in pressure (Hansen and Hanssen, 1988)*

	Air cushion chamber
Theoretical σ_v , MPa	5.0
Measured σ_v , MPa	5.7
σ_1 , MPa	15.6
σ_2 , MPa	6.1
σ_3 , MPa	2.7
P_s (shut-in pressure), MPa	5.1
Internal water pressure at measuring point, MPa	2.4
Direction σ_H (Myrvang, 2001)	N040°E

The hydraulic fracture test gave a higher value for σ_3 (5.1 MPa) than the value measured in the overcoring test (2.7 MPa). It can also be noted that the result from the overcoring test is nearly equal to the internal water pressure at the measuring location (2.4 MPa). According to Neupane (2017) the increase in water pressure during load rejections and with the factor of

safety of design in mind, it is evident that the minor principal stress must be higher than 2.7 MPa, since the plant has been operating without major problems over many years. Hence the result from the hydraulic fracture test is regarded as a good estimate for σ_3 , and will be used in the further analysis.

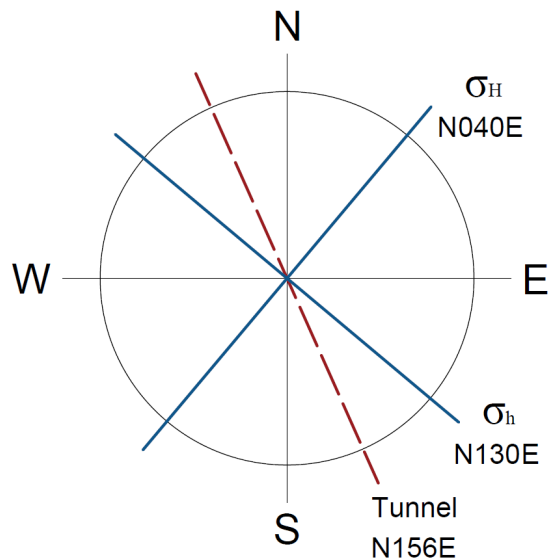


Figure 7.12: Directions of the major and minor horizontal stresses and the tunnel alignment

7.5 Instability issues along the headrace tunnel

Inspections of the headrace tunnel was carried out both in 2008 and in 2015. One of the main tasks of the Project work was to study the inspection reports, with associated pictures and sketches, and identify the different instability issues that had been observed. The most important registered stability issues were compiled into the map presented in Appendix D, and were categorized into four different modes:

1. Collapse in weakness zone
2. Stress induced spalling and buckling
3. Block and wedge fall caused by intersecting joints and seams
4. Block fall caused by joints and stress induced fracturing

7.5.1 Collapse in weakness zone

At the northern end of the headrace tunnel, close to the Skamfer adit, one prominent depression in the terrain is observed on satellite imagery. This is interpreted as a weakness zone. The zone is intersecting the tunnel line with an acute angle (see Figure 7.13). The out-crop at the surface is slightly curved, indicating that the zone is steeply dipping towards the north-east.

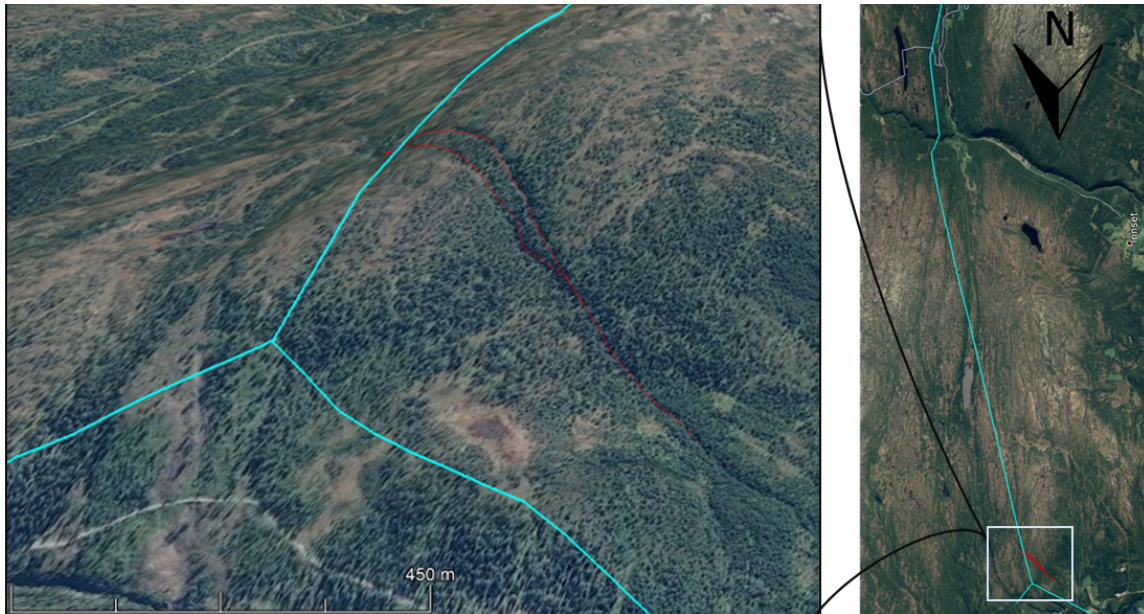


Figure 7.13: Weakness zone (red line) that intersects the headrace tunnel (blue) in the downstream end, from Google Earth V7.3.0.3832. (2017).

In 2008 a major collapse occurred in a weakness zone, approximately 1200 m upstream the Skamfer adit. This is most likely the same weakness zone as the one observed in the satellite imagery. A detailed drawing of the failure is presented in Figure D.3 in Appendix D. The collapsed zone was 1 meter wide, intersecting the tunnel at an angle of approximately 40° .

According to Dr. Krishna Panthi (discussion during Project work), there was detected swelling material in the zone after the failure. Swelling clay and the mobilization of swelling pressure would be a critical cause of the failure. The zone had been supported to a certain extent during the construction works, but the installed support measures were not designed for the swelling pressure and the deformation that developed. Although the zone was only 1 m wide, the unfavourable orientation of the zone lead to a large affected area and a 6 m long section that needed lining in the repairing works.

7.5.2 Stress induced spalling and buckling

Several occurrences of spalling and buckling are reported from the headrace tunnel. Blindheim (1982) describes tendencies to buckling behaviour in very schistose phyllite during the excavation works. The buckling occurred in the lower tunnel wall and abutment, as shown in Figure 7.14. Although this lead to some falling rock mass from the upper wall and crown, it did not cause any construction delays. From the inspection in 2015 there are also reported incidents of rock spalling. The reported volumes of failed rock are generally small, and seemed to be mainly located in the quartzitic phyllite. In some areas the spalling appeared quite fresh (Midtlyng, 2015).

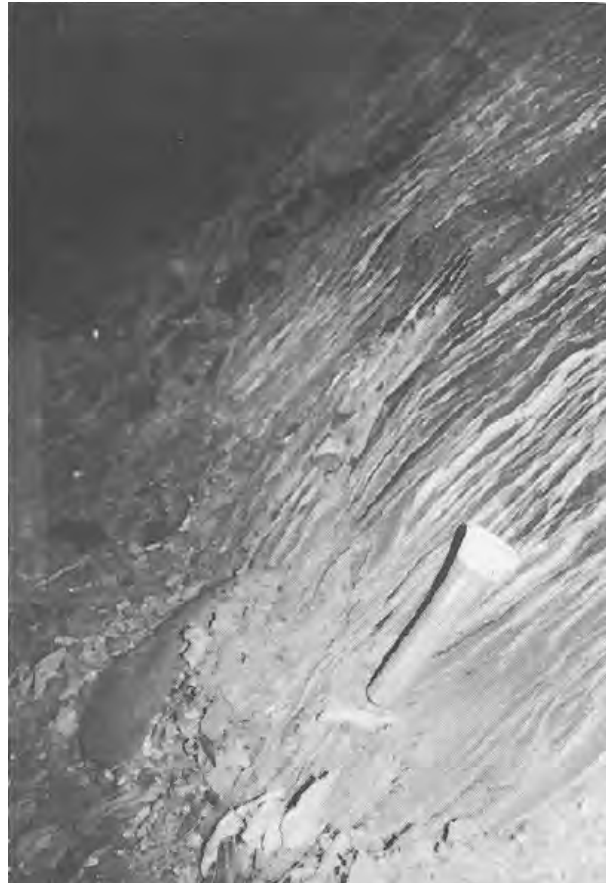


Figure 7.14: Buckling behaviour in schistose phyllite during construction of Brattset head-race tunnel. Here buckling appears in the lower wall (Blindheim, 1982).



Figure 7.15: Block fall from tunnel roof, downstream the pressure shaft (Landløpet, 2015).

7.5.3 Block fall caused by intersecting discontinuities

From the inspections in 2008 and 2015, there were reported of several block falls along the tunnel. The described volumes are relatively small, with blocks of 1 m³ or less. The block falls seems to occur in both the phyllite and the quartz keratophyre, and the distinct blocks and wedges are formed by intersecting discontinuities in the rock mass.

The most prominent discontinuity set in the phyllite is the foliation plane. Along the foliation joints there are also observed several cases of gouge filling in seams. These planes have low friction and may be an important factor to the occurrence of these failures. In the quartz keratophyre there are observed three pronounced joint sets, forming nearly cubic block in the rock mass. It is believed that many of the observed rock "dices", as Midthlyng (2015) terms the fallen blocks, are of the quartz keratophyre.

7.5.4 Block fall caused by joints and induced fracturing

From both tunnel inspections there are reports of a few serious block falls, with volumes up to 15 m². In 2008, a serious failure with several large blocks was observed in the upstream end of the headrace tunnel, at chainage 10 400. In 2015, at the same location, a new large block fall was reported. At chainage 9000 another large block fall was observed in 2015, where it in 2008 had been observed a large clay-filled seam. Several similar seams have been observed in the tunnel. They are following the schistosity plane in the rock mass, giving an unfavorable orientation with longitudinal extension parallel to the tunnel axis and with moderate to steep dip angles into the tunnel.

Figure 7.16 show a photo taken of one event that was discovered in 2015. The estimated volume is 15 m³, with large rock slices of 3-6 m³. A very distinct sliding plane is steeply dipping into the tunnel, and the failed rock mass is deposited on the tunnel floor. The slice shaped blocks indicate that stress related mechanisms may be involved in the failure, in addition to a joint or seam as the sliding plane.

It is believed that the compressive stress in the vicinity of the tunnel contour is causing fractures to develop in the tunnel crown. Since the confining pressure in the rock mass near the tunnel opening is low, the compressive tangential stress may cause the rock to fail in an extensile manner (Diederichs, 2014). These cracks will form parallel to the major compressive stress and at some point, intersect with existing discontinuities in the rock mass. As the fracturing process continue the cracks coalesce and a continuous joint may eventually be formed. The intersecting discontinuities now form a large volume, with the potential to fall or slide into the tunnel.



Figure 7.16: Large block fall on Ch. 10 400 in 2015. The large volumes may have been caused by fracturing in the roof that developed and intersected a joint or seam in the tunnel wall (Landløpet, 2015).

Chapter 8

Laboratory investigations

Rock samples of phyllite and quartz keratophyre were collected during field work, with the purpose of rock mechanical testing in laboratory. Testing of the quartz keratophyre was carried out by Neupane (2017), and the results from his work will be given here. The phyllite sample was tested during the thesis work by the author, and procedures and results from the laboratory investigations will be presented in this chapter.

Mineralogical content is determined through X-ray powder refraction. As the phyllite turned out too weak and schistose for preparation of cores for UCS testing, intact rock mass strength is indirectly estimated through point load test. Testing is generally performed according to ISRM's suggested methods, which will only be briefly presented here. The reader is referred to the ISRM standards for detailed description of the testing procedures, ISRM (1985) and ISRM (1978a). As a standard procedure during the laboratory work, the density of the phyllite was measured by use of pycnometer. The density was found to be 3.13 g/cm^3 , equivalent to a unit weight of 30.7 kN/m^3 .

8.1 X-Ray Powder Diffraction (XRD)

In order to characterize the rock mass, determination of the mineralogical composition and texture should be carried out. The most common methods of mineral analysis are with thin sections and X-ray diffraction techniques (ISRM, 1978a). Since only an approximate mineralogical composition of the phyllite is necessary for further work, only X-Ray powder diffraction (XRD) was conducted during the thesis work.

According to Mitchell and Soga (2005), the method is based on diffraction of X-ray waves from the crystal lattice of minerals. When X-rays strike a crystal, the incident rays will be reflected from different atomic planes in the crystal lattice, spaced at a distance d . At a certain angle θ , the path length difference between the reflected rays is equal to an integral number of the wave length $n\lambda$, and interference occur. These conditions can be expressed as

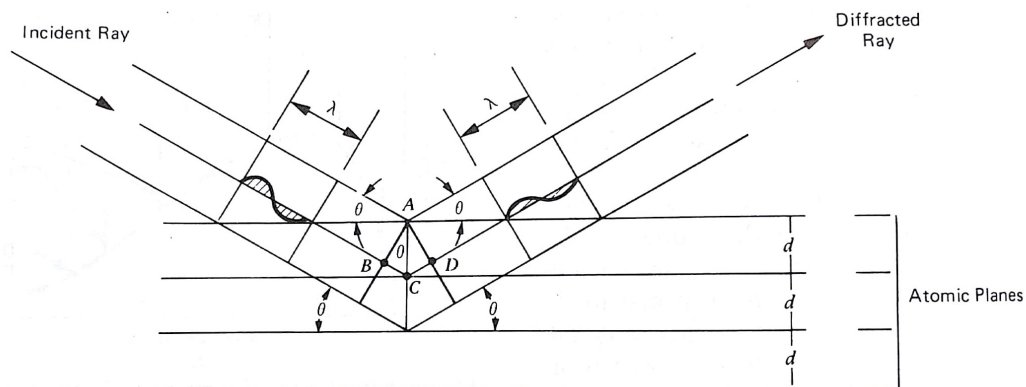


Figure 8.1: Geometrical conditions for X-ray diffraction (Mitchell and Soga, 2005)

$n\lambda = 2d \sin\theta$, known as *Bragg's Law*, see Figure 8.1. Since no mineral has the same space between the atomic planes, the angles at which diffraction occur can be used for mineral identification.

8.1.1 Procedure and results

The sample was prepared by grinding a representative rock piece into a fine powder. The powder was packed into a sample holder, where the upper surface was carefully flattened. The sample was then placed into the X-ray instrument. As the sample and deflector go through a range of angles, the intensity of the diffracted x-rays is continuously recorded. Identification and quantification of the mineral components were done by comparing the peak positions in resulting plot to standard reference patterns.

The plot of the X-ray patterns from the XRD analysis is given in Appendix E, and the mineralogical content is presented in Table 8.1. The result indicates that the phyllite is mainly composed of amphibole, chlorite and plagioclase. Minor components are clinozoisite, feldspar, pyroxene and quartz. The high content of amphibole will explain the relatively high density of the phyllite.

Table 8.1: Results from XRD analysis of phyllite

Mineral/mineral group	%
Quartz	2
Plagioclase	10
Feldspar	4
Pyroxene	2
Chlorite	11
Amphibole	63
Clinozoisite	8

8.2 Point load index test

The point load test is an index test for strength classification of rock materials. The test may also be used to predict other strength parameters with which it is correlated to, such as uniaxial compressive and tensile strength (ISRM, 1985). A test specimen (core, cut block or irregular lump), preferably with diameter ranging between 15-100 mm, is placed inside the test apparatus and applied concentrated load through a pair of spherical truncated, conical platens. Requirements for specimen shape and load directions are illustrated in Figure 8.2. The load is steadily increased such that failure of the test specimen occurs within 10-60 sec. The test is only valid if the fracture surface passes through both loading points, as illustrated in Figure 8.3. If not, the test should be rejected as invalid.

The failure load, P , is recorded, and based on the test specimen measured diameter, the point load index I_s is calculated by Equation (8.1) (ISRM, 1985):

$$I_s = \frac{P}{D_e^2} \quad (8.1)$$

where D_e is the "equivalent core diameter", and is given by:

$$D_e^2 = D^2 \quad \text{for diametral test}$$

$$D_e^2 = 4A/\pi \quad \text{for axial, block and lump test}$$

and $A = WD$ minimum cross sectional area of a plane through the loading points

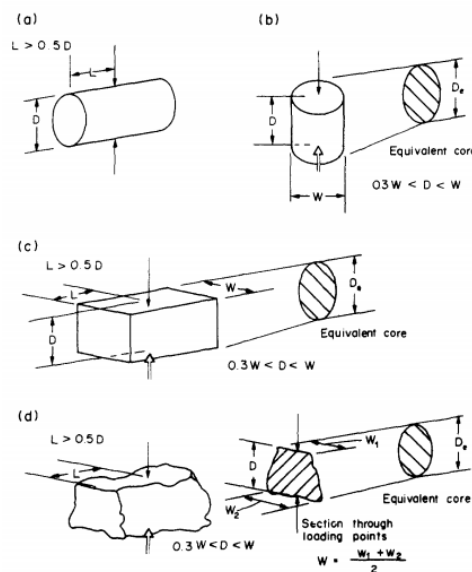


Figure 8.2: Specimen shape requirements for (a) diametral test, (b) axial test, (c) block test and (d) irregular lump test (ISRM, 1985).

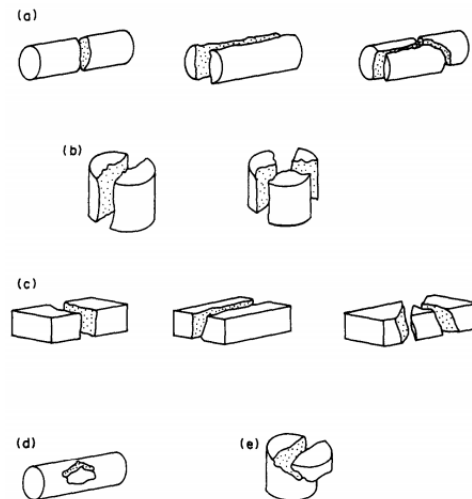


Figure 8.3: Valid and invalid failure modes for point load test: (a) valid diametral tests, (b) valid axial tests, (c) valid block tests, (d) invalid diametral test, (e) invalid axial test (ISRM, 1985).

I_s varies as a function of D_e , so a size correction must be applied to obtain a unique point load strength value. The size corrected point load strength index $I_{s(50)}$ to the standard diameter $D = 50$ mm is given by:

$$I_{s(50)} = F \cdot I_s \quad (8.2)$$

where the correction factor F is given by:

$$F = \left(\frac{D_e}{50} \right)^{0.45} \quad (8.3)$$

When a rock sample is anisotropic it should be tested in the directions which give the smallest and greatest strength values. In general, this is in the directions parallel and normal to the anisotropy plane (ISRM, 1985).



Figure 8.4: Blocks prepared for point load testing

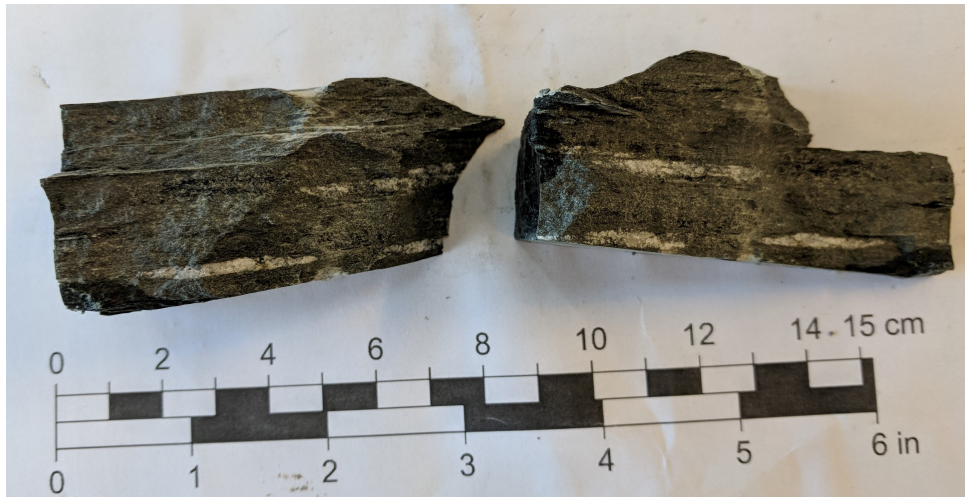


Figure 8.5: Fracture surfaces from testing normal to the foliation plane

8.2.1 Procedure and results

The phyllite sample was cut into blocks, with cutting surfaces orientated parallel and normal to the foliation plane (see Figure 8.4), with sizes varying between 30x20 mm and 50x40 mm. The blocks were submerged into water for four days before testing. 40 tests were carried out with loading perpendicular to the foliation plane, and 18 tests were done parallel with the foliation. 20 tests were considered as invalid, as the fracture plane did not pass through both of the loading points.

The test results are given in Appendix E. The mean size-corrected point load index $I_{s(50)}$ is calculated as the average from the valid tests, where the two highest and the two lowest values are deleted (ISRM, 1985). The obtained mean values and anisotropy index from the testing are given in Table 8.2.

Table 8.2: Results from point load index test, size corrected values

	Mean (MPa)	St. dev. (MPa)
Mean $I_{s(50)}$, perpendicular	10.2	2.3
Mean $I_{s(50)}$, parallel	3.4	1.9
Anisotropy index I_a	3.0	–

Comment on the test results

The phyllite proved to be very strong in the direction normal to the foliation plane, while the strength in the direction parallel to the foliation was governed by the strength of the weakness planes. The anisotropy index indicate that the phyllite is more than three times stronger normal to than along the foliation, and is classified as *highly anisotropic* according to Table 3.4.



Figure 8.6: Fracture surfaces from testing parallel with the foliation plane

All the invalid tests were of those done in the direction perpendicular to the foliation plane. The majority of these specimens broke along the foliation plane instead of through the loading points, again indicating the high grade of strength anisotropy. All the test done in the parallel direction resulted in perfect fracture surfaces along the foliation, see Figure 8.6.

The samples were submerged in water for four days before testing. However, during the fracturing of the samples it was observed that the blocks seemed dry within and that water had migrated only a few mm into the blocks. This indicates that the rock is impermeable and will need longer to be fully saturated. The result from the point load test is therefore considered as the point load strength of dry rock.

According to ISRM (1985) the point load strength can be correlated to the uniaxial compressive strength of intact rock. On average the UCS is 20-25 times higher than the point load strength. However, for very anisotropic rocks the ratio can often vary between 15 and 50, and errors up to 100 % are possible if an arbitrary ratio is chosen. Hence, in this case the obtained results from the point load test need to be used with great caution in the determination of an input strength for the stability analysis. The result should be compared to previously measured strength values on similar rock mass, and only work as a guiding figure when choosing input for the analysis.

8.3 Results from testing of quartz keratophyre

Laboratory testing of the quartz keratophyre samples has been conducted by Mr. Bibek Neupane. The results from UCS testing are summarized in Table 8.3, and the result from XRD analysis is given in Table 8.4.

The results from UCS testing indicate that the quartz keratophyre is strong and hard. The major mineralogical components are plagioclase and quartz, while minor components are muscovite and biotite.

Table 8.3: Results from UCS test of quartz keratophyre. Testing conducted on 6 cores

Parameter	Lowest	Average	Highest
UCS, MPa	101.8	135.3	159.4
E modulus, MPa	58 410	62 150	66 170
Poisson's ratio	0.25	0.29	0.37
Density, kg/m ³	2650	2655	2660

Table 8.4: Results from XRD analysis of quartz keratophyre, average of two samples

Mineral/mineral group	%
Quartz	32
Plagioclase	64
Muscovite	2
Biotite	2

Chapter 9

Establishment of input parameters

Engineering geological conditions at Brattset HPP and the observed instability issues inside the headrace tunnel have been presented in the previous chapters. In order to carry out stability assessments of these instabilities, some additional information is required. In this chapter rock mass properties, joint conditions and water pressure are evaluated and prepared for use in stability assessments. Finally, to determine the in-situ stress conditions an elastic stress analysis is carried out.

To estimate the required parameters for the Mohr-Coulomb and the Hoek-Brown failure criteria, the *RocData* software will be applied. RocData is a useful program where strength envelopes and other physical parameters can be determined for various failure criteria (Rocscience Inc., 2017). Several estimations for rock mass strength and deformation modulus were presented in Chapter 3. It is decided to employ the formulas of Hoek and Diederichs (2006) and Hoek et al. (2002), which are incorporated into RocData, and the formulas of Panthi (2006) and Panthi (2017), which are well suited for anisotropic rock mass.

9.1 Estimation of rock mechanical properties

In the following section rock mechanical properties of the rock relevant to stability assessments are evaluated, based on laboratory results, literature and field observations. The obtained values are summarized in Tables 9.1 and 9.2. While the quartz keratophyre appears consistent through the area, some variations in the quality and mineralogical composition of the phyllite are observed. It is however assumed that the rock mechanical properties of the phyllite is approximately constant and that the rock mass behaviour is largely governed by the conditions of the present joints at the different locations.

Laboratory testing of the quartz keratophyre was conducted by Neupane (2017). As a conservative approach, it is chosen to apply the lowest obtained test values for the strength and

stiffness input. As little rock mechanical information was possible to obtain from laboratory testing of the phyllite, typical values are found in literature. A collection of test results from the rock mechanics laboratory at NTH/NTNU/SINTEF (Li, 2015b) lists rock mass properties of phyllites and quartzitic phyllites from different locations in Norway, including one phyllite from Berkåk close to Brattset HPP.

9.1.1 Compressive strength

The values for uniaxial compressive strength of phyllites presented by Li (2015b) are in the range of 26 to 176 MPa, where the lowest values belong to phyllites and the highest values come from quartzitic phyllites. The point load test that was carried out on the phyllite sample from the project area, resulted in a relatively high point load strength index (perpendicular to the foliation plane). It is then reasonable to assign a strength value from the upper part of the suggested range. Due to saturation of the rock mass after water filling of the tunnels, the initial rock strength is expected to be reduced. As discussed in Chapter 3, the strength reduction is significant for schistose rock and rock composed of dark minerals. Depending on the mineral composition (high content of amphiboles) and grade of schistosity, it is assumed a strength reduction of 30-50 % in the phyllite, while in the quartz keratophyre a reduction of about 10 %.

9.1.2 Elastic parameters

Measurements of elastic parameters for phyllite and quartzitic phyllite are also found in Li (2015b). Regarding the intact deformation modulus E_{ci} , the majority of the measured values range between 23-55 GPa. For Poisson's ratio ν , the values are between 0.10-0.15. Unlike for the compressive strength of the rocks, no significant difference between phyllite and quartzitic phyllite is observed for the elastic parameters.

9.1.3 Hoek-Brown parameters

Parameters that need to be determined for the Hoek-Brown failure criteria are GSI , m_i and D . These parameters are also useful for estimating Mohr-Coulomb parameters through the RocData software. Since the tunnel is drilled by TBM, the disturbance of the surrounding rock mass is minimal. Hence, the disturbance factor D is 0 (Hoek, 2007).

Based on results from field mapping, GSI values for the phyllite and the quartz keratophyre are estimated. The quartz keratophyre consists of distinct cubical blocks and has generally rough, unweathered surfaces. The GSI value is therefore set to 70 ± 5 , as illustrated by a red hatch in C.1, Appendix C. The phyllite varies from a blocky structure to a more schistose structure with no distinct blocks. Also the surface conditions vary, from rough and slightly

weathered, to smooth and moderately weathered. Hence, the GSI value is chosen to be in the range 45-65 (green hatch).

Table 9.1: Estimated mechanical properties of quartz keratophyre (10 % strength reduction in saturated rock)

Parameter	Description	Value	Unit	Source
$\sigma_{ci,dry}$	Intact rock strength, dry	101.8	MPa	(Neupane, 2017)
$\sigma_{ci,sat}$	Intact rock strength, saturated	91.6	MPa	
GSI	Geological strength index	70	–	Figure C.1
m_i	Material constant	25 ± 5	–	(Hoek, 2007)
D	Disturbance factor	0	–	(Hoek, 2007)
E_{ci}	Intact deformation modulus	58.4	GPa	(Neupane, 2017)
ν	Poisson's ratio	0.25	–	(Neupane, 2017)
γ	Specific weight	26.5	kN/m ³	(Neupane, 2017)

Table 9.2: Estimated mechanical properties of phyllite (assuming 30-50 % strength reduction in saturated rock)

Parameter	Description	Value	Unit	Source
$\sigma_{ci,dry}$	Intact rock strength, dry	60-140	MPa	(Li, 2015b)
$\sigma_{ci,sat}$	Intact rock strength, saturated	30-98	MPa	
GSI	Geological strength index	45-65	–	Figure C.1
m_i	Material constant	7 ± 3	–	(Hoek, 2007)
D	Disturbance factor	0	–	(Hoek, 2007)
E_{ci}	Intact deformation modulus	23-55	GPa	(Li, 2015b)
ν	Poisson's ratio	0.10-0.15	–	(Li, 2015b)
γ	Specific weight	30.7	kN/m ³	Lab testing
I_a	Strength anisotropy index	3.01	–	Lab testing

Determination of the rock mass constant m_i is done according to Hoek (2007). The quartz keratophyre is an isotropic, medium to fine-grained volcanic rock. In the determination of the rock mass constant m_i , it is then reasonable to assume similarities to andesite, rhyolite and dacite, whose typical m_i values are in the range $25 \pm (3 - 5)$. The suggested m_i value for phyllite is 7 ± 3 . However, these values are obtained from testing normal to bedding or foliation. Since the phyllite is highly anisotropic, the value will be significantly different if failure occur along a weakness plane (Hoek, 2007). The expected failure mode should therefore be considered before assigning a m_i value to the phyllite.

9.1.4 Dilation parameter

Dilatancy is a measure of how much volume increases that occurs when the rock material is sheared, and is a required input parameter for plastic materials in RS^2/RS^3 . According to Rocscience Inc. (2018[a]), the dilatancy for a Mohr-Coulomb material is an angle that generally varies between zero and the friction angle. For Hoek-Brown materials, the dilatancy is defined by a parameter that generally varies between zero and m .

Low dilation angles/parameters are generally associated with soft rock masses while high dilation angles/parameters are associated with hard brittle rocks. Rocscience Inc. (2018[a]) suggests that a good starting estimate of the dilatancy is $0.333 m$ or 0.333ϕ for soft rocks and $0.666 m$ or 0.666ϕ for hard rocks. Since the rock mass in this study are of medium hard, a good estimate would be round 0.5ϕ or $0.5 m$.

9.2 Joint properties

9.2.1 Shear strength parameters

As it has been pointed out, the behaviour of moderately jointed rock mass is mainly governed by the joint properties. The joint characteristics of quartz keratophyre and phyllite were mapped during field work and classified based on the Q-system. In Barton and Bandis (1990) relationships between Q-system parameters and input parameters in the Barton-Bandis empirical model are described. The mapped J_a and J_r values may be correlated with the residual friction angle (ϕ_r) and the joint roughness coefficient (JRC) and in this model. The third parameter in Barton-Bandis model is the joint compressive strength (JCS), which is a measure of the joint wall strength.

4. JOINT ALTERATION NUMBER	(J_a)	(ϕ_r)
(a) <i>Rock wall contact</i>		(approx.)
A. Tightly healed, hard, non-softening, impermeable filling i.e. quartz or epidote	0.75	(-)
B. Unaltered joint walls, surface staining only	1.0	(25-35°)
C. Slightly altered joint walls. Non-softening mineral coatings, sandy particles, clay-free disintegrated rock etc.	2.0	(25-30°)
D. Silty-, or sandy-clay coatings, small clay fraction (non-soft.)	3.0	(20-25°)
E. Softening or low friction clay mineral coatings, i.e. kaolinite or mica. Also chlorite, talc, gypsum, graphite etc., and small quantities of swelling clays.	4.0	(8-16°)

Figure 9.1: Relationships between the Q-system parameter J_a and residual friction angle ϕ_r (Barton and Bandis, 1990)

Relation between J_r and JRC_n Subscripts refer to block size (cm)		J_r	JRC_{20}	JRC_{100}
I	rough	4	20	11
	smooth			
	slickensided			
Stepped				
IV	rough	3	14	9
	smooth			
	slickensided			
V	rough	2	11	8
	smooth			
	slickensided			
Undulating				
VII	rough	1.5	2.5	2.3
	smooth			
	slickensided			
Planar				
VIII	rough	1.0	1.5	0.9
	smooth			
	slickensided			
IX	rough	0.5	0.5	0.4
	smooth			
	slickensided			

Figure 9.2: Relationships between J_r in the Q -system and JRC_n (Barton and Bandis, 1990)

The relationships between J_a and ϕ_r are given in Figure 9.1 and for J_r and JRC, in Figure 9.2. Barton and Bandis (1990) suggest that the JCS value of fresh, unaltered joints equals σ_{ci} of the rock mass. However, according to Nilsen and Broch (2012) the correlation between JCS and σ_{ci} of the rock mass is inaccurate, and JCS should be determined with a Schmidt rebound hammer in field. Since no Schmidt rebound hammer were used during field work at Brattset, the estimated σ_{ci} value is assumed to represent the JCS of fresh, unaltered joints in the absence of other figures. Further, it is here assumed that the reduction in joint wall strength due to weathering and alteration proceeds in the same fashion as for rock masses, see Table 3.5 and Figure 3.6.

9.2.2 Joint stiffness

One of the required parameters in RS^2 is the joint stiffness (normal and shear). The joint stiffness describes the stress-deformation characteristics of joints, both in normal and tangential direction (Barton, 1972). The normal stiffness, K_n , can be estimated by the intact rock modulus E_{ci} , rock mass modulus E_m and joint spacing L . In the same way can the shear stiffness, K_s , be estimated from the intact shear modulus G_i , rock mass shear modulus G_m and the joint spacing. The following relations apply (Goodman, 1989):

$$K_n = \frac{E_{ci} \cdot E_m}{L(E_{ci} - E_m)} \quad (9.1)$$

$$K_s = \frac{G_i \cdot G_m}{L(G_i - G_m)} \quad (9.2)$$

where the shear modulus modulus G is calculated by the following equation, given Young's modulus E and Poisson's ratio ν :

$$G = \frac{E}{2(1 + \nu)} \quad (9.3)$$

9.3 Water pressure in joints

During constant operation of the plant, the flow regime inside the headrace tunnel is steady, such that the water pressure within the rock mass and inside the tunnel is equal and in equilibrium. Frequent start-stop sequences as well as fluctuating operation regime, give rise to water hammer and mass oscillations, which result in fluctuations in the water pressure along the tunnel system.

As discussed in Chapter 5, mass oscillations arise within the headrace tunnel upstream the air cushion chamber. According to Dr. Krishna Panthi (discussion with supervisor, 24.05.18), these pressure fluctuations should in principle cause an increase in the water pressure acting on the joints, influencing the stability of hanging rock blocks. In addition, due to the dynamic conditions during mass oscillations, the buoyancy from the water flow inside the tunnel is also active, which in principle aggravates the instability of the hanging block. However, to simplify the calculations the, the effect of buoyancy is ignored here. Hence, only the differential pressure that arise inside the joints will be considered in the stability assessments. Amplitude of the hydraulic transients at Brattset were calculated in Chapter 5, and the maximum differential pressure is given by the peak-to-peak amplitude:

$$\Delta u = 2\Delta z \gamma_w = 2 \cdot 83.5 \text{ m} \cdot 9.81 \text{ kN/m}^3 = 1.6 \text{ MPa} \quad (9.4)$$

9.3.1 Distribution of load

Consider the rise in water pressure in a joint due to an upsurge wave, and the following downsurge wave that creates a pressure drop inside the headrace tunnel. It is difficult to predict the response along the joint, whether the joint pressure drops instantly or if there is a delay. Assuming that there is some delay, the worst case pressure will then be given by the differential pressure in Equation (9.4).

The load distribution along the joint is illustrated in Figure 9.3. Due to the elevation given by the height of the joint (h_j), the pressure at the end of the joint is slightly lower than at the tunnel contour. However, compared to the peak-to-peak amplitude of the mass oscillations (167 m), the pressure difference due to the joint height is considered negligible (1-3 m). The water pressure acting on the joint can therefore be regarded as an evenly distributed load in the stability analyzes.

It is of interest to compare the water pressure situation during mass oscillations to the pressure situation during drainage of the tunnel. Considering the same joint, the hydrostatic head at the specific tunnel location before draining would be H , as illustrated in Figure 9.4. The pressure at the tunnel contour equals $H - h_t$, where h_t is the water head when the water level is at the tunnel crown. As the water head inside the tunnel is gradually lowered to the height of the tunnel, i.e. $H = h_t$, the differential pressure at the tunnel contour becomes $\Delta u = 0$. The time it takes to drain the tunnel is of such length that partly draining of the joint also occur. Thus, the pressure on the joint wall can be regarded as a triangular distributed load, where the pressure at the end of the joint equals to the pressure before draining (considering the joint height), $\Delta u = (H - h_t - h_j)\gamma_w$.

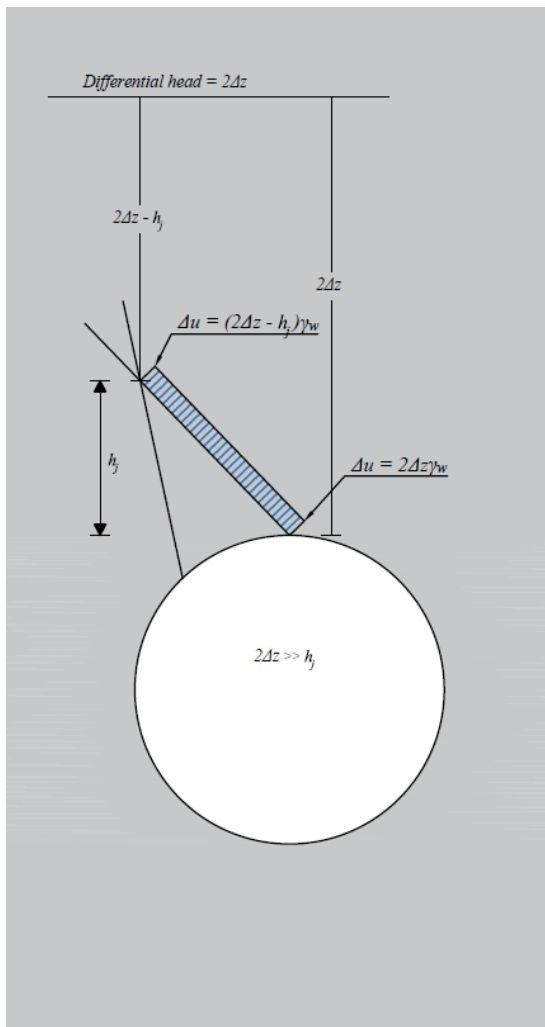


Figure 9.3: Differential pressure in joint due to mass oscillations

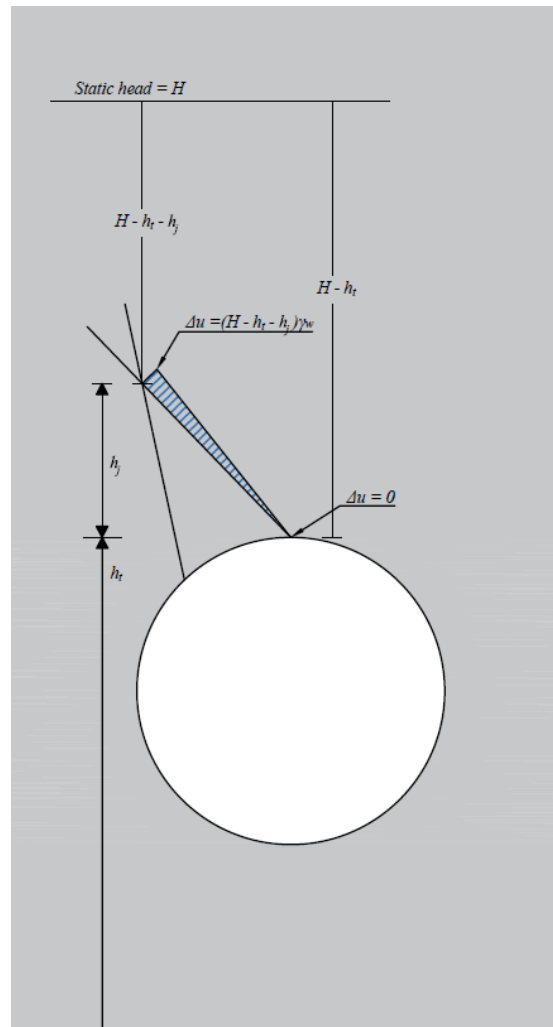


Figure 9.4: Differential pressure in joint due to draining

9.4 Estimation of in-situ stress conditions

The only known values for the in-situ rock stresses in the area are obtained from the air cushion chamber location (Hansen and Hanssen, 1988). Based on these values a stress analysis may be carried out, in which the stress ratio k can be determined. Such an analysis was performed by Neupane (2017), and the same procedure is followed here.

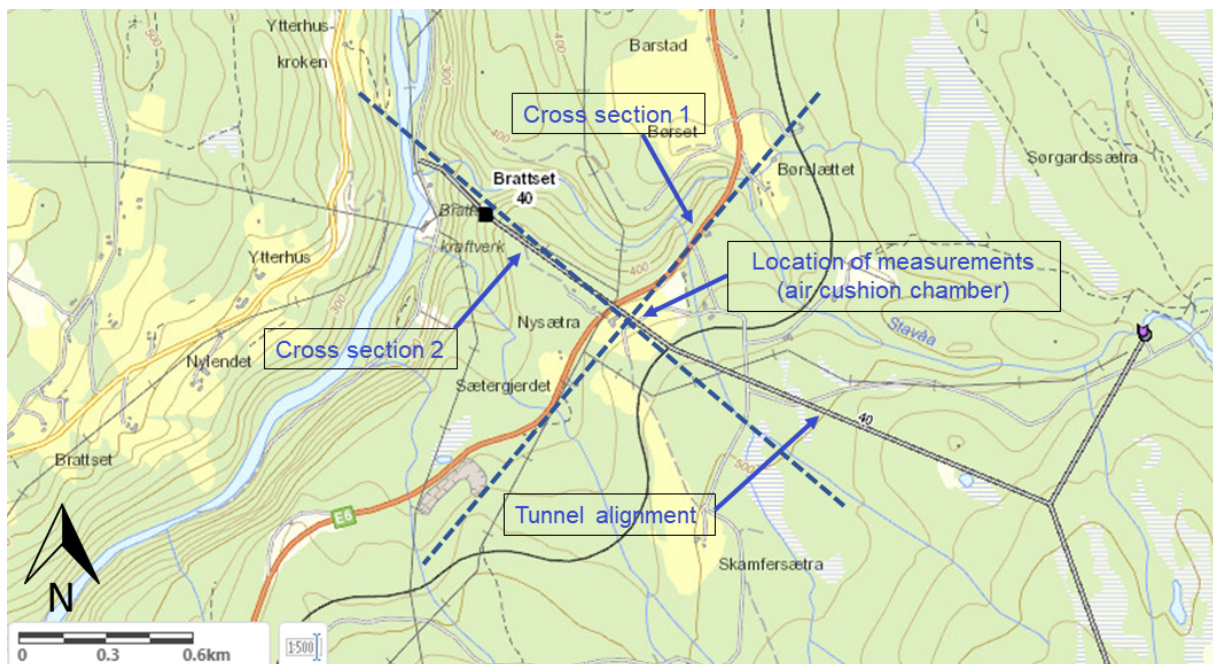


Figure 9.5: Location of cross section in stress condition analysis. Modified from NVE (n.d.)

9.4.1 Model set up

The analysis is problem is solved with a 2D topographical model. Two cross sections, one parallel and one normal to the direction of the assumed maximal horizontal stress. The location of the cross sections, tunnel and stress measurements are indicated in Figure 9.5. The topographical profiles are imported from Kartverket (2018), and the topographical model of cross section 2 is shown in Figure 9.6. The bottom boundary of the model is restrained in both X and Y direction, the sides are restrained in the X direction only, while the top surface is free to move in both directions. Further is gravity type field stress chosen, with the use of actual ground surface since the model profile has variable elevation.

In order to study the stresses in the rock mass, the material is assumed to be elastic. In this way the stresses can develop without any failure occurring in the material. It is assumed that 10 % of the rock mass consists of quartz keratophyre, while the rest is phyllite (Flønes, 1982). In laboratory the unit weight of the phyllite is found to be 30.7 kN/m^3 , and 26.5 kN/m^3 for the quartz keratophyre. As observed during the desk study, the soil cover in the area is very thin

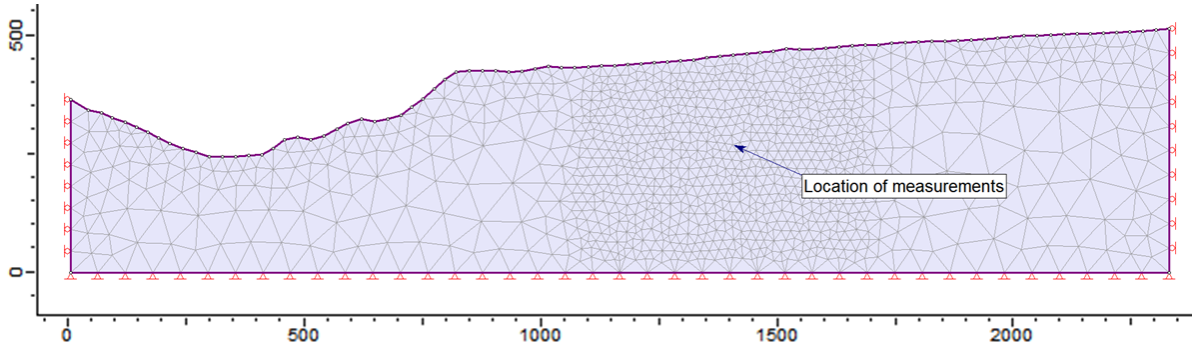


Figure 9.6: Topographical model of cross section 2 and stress measurements location

or not existing. The topographical model can therefore be assumed to consist completely of rock material. The average weight of the material in the model is hence assumed to be approximately 30 kN/m^3 , or 0.03 MN/m^3 .

9.4.2 Results

The two models were run with various loading conditions, with the aim to achieve the measured stresses at the location of the air cushion chamber. The result from one of these simulations is shown in Figure 9.7. The chosen rock mass density and location of the air cushion chamber in the model resulted in a vertical stress equal to the measured value, indicating adequate assumptions. Table 9.3 show the results from a number of trials, with different stress ratios in both maximum and minimum horizontal stress directions, and the obtained stresses at the point of the air cushion chamber.

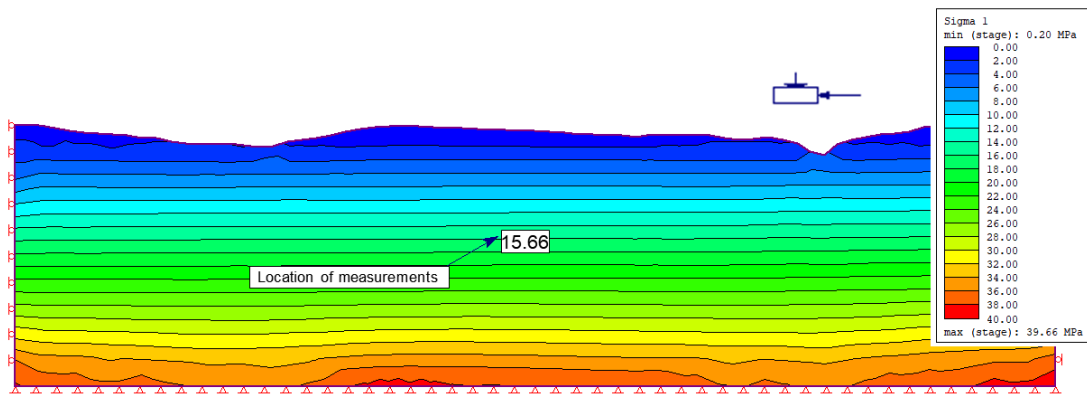


Figure 9.7: Simulation of stress conditions in cross section 1 (σ_1). Applied stress ratios are 2.85/1.10.

In cross section 1, a model with the ratios 2.85 and 1.10, of σ_H/σ_v and σ_h/σ_v respectively, gives the results closest to the measured values. In cross section 2 the most fitting ratios are 2.75 and 1.08. Stress trajectories in cross section 1 show that the major principal stress σ_1 is horizontal and not significantly affected by topography. In cross section 2, inclined

stress trajectories at the measuring point indicate that the stress directions are affected by the valley side, with the moderate principal stress σ_2 plunging towards the valley bottom. In this case the observed σ_3 value is smaller than the vertical stress, which corresponds well with the measured values. Consequently, the ratio of σ_h/σ_v from cross section 2 (1.07) gives the most realistic values, while the σ_H/σ_v ratio should be within 2.75-2.85. These are the values that will be used for determining the stress conditions in the further analyses of the instability issues along the headrace tunnel.

Table 9.3: Result of stress analysis with different stress ratios. The ratios giving results closest to the measured values are emboldened. Material density = 0.03 MN/m^3

	Stress ratio k		Modelled stresses			
	σ_H/σ_v	σ_h/σ_v	σ_v	σ_1	σ_2	σ_3
Cross section 1, parallel to maximum horizontal stress	2.80	1.10	5.71	15.38	6.10	5.71
	2.85	1.10	5.71	15.66	6.09	5.71
	2.90	1.10	5.71	15.93	6.09	5.71
Cross section 2, normal to maximum horizontal stress	2.75	1.05	5.71	15.60	6.05	5.21
	2.75	1.07	5.71	15.59	6.10	5.26
	2.75	1.10	5.71	15.59	6.20	5.33
Measured values (goal)			5.7	15.6	6.1	5.1

9.4.3 Application in further analysis

The obtained stress ratios in the stress analysis will be used to calculate the stress magnitudes at different locations along the headrace tunnel. The vertical stress can be determined by the following equation (Li, 2015a):

$$\sigma_v = \gamma z \tag{9.5}$$

where γ is the average unit weight of the overlaying rock mass and z is the tunnel depth. From the obtained value of σ_v , the maximum and minimum horizontal stresses can be calculated using the stress ratios determined above.

When modelling in two dimensions, the model cross section will be made normal to the tunnel axis. Since the horizontal stresses are not aligned normal and parallel to the tunnel alignment, they have to be resolved into the equivalent in-plane and out-of-plane stresses, as illustrated in Figure 9.8. This can be solved either by using the stress transformation tool

in RS^2 , or by the following equations (Li, 2015a):

$$\sigma_{in-plane} = \sigma_H \cos^2 \alpha + \sigma_h \sin^2 \alpha \quad (9.6)$$

$$\sigma_{out-of-plane} = \sigma_H \sin^2 \alpha + \sigma_h \cos^2 \alpha \quad (9.7)$$

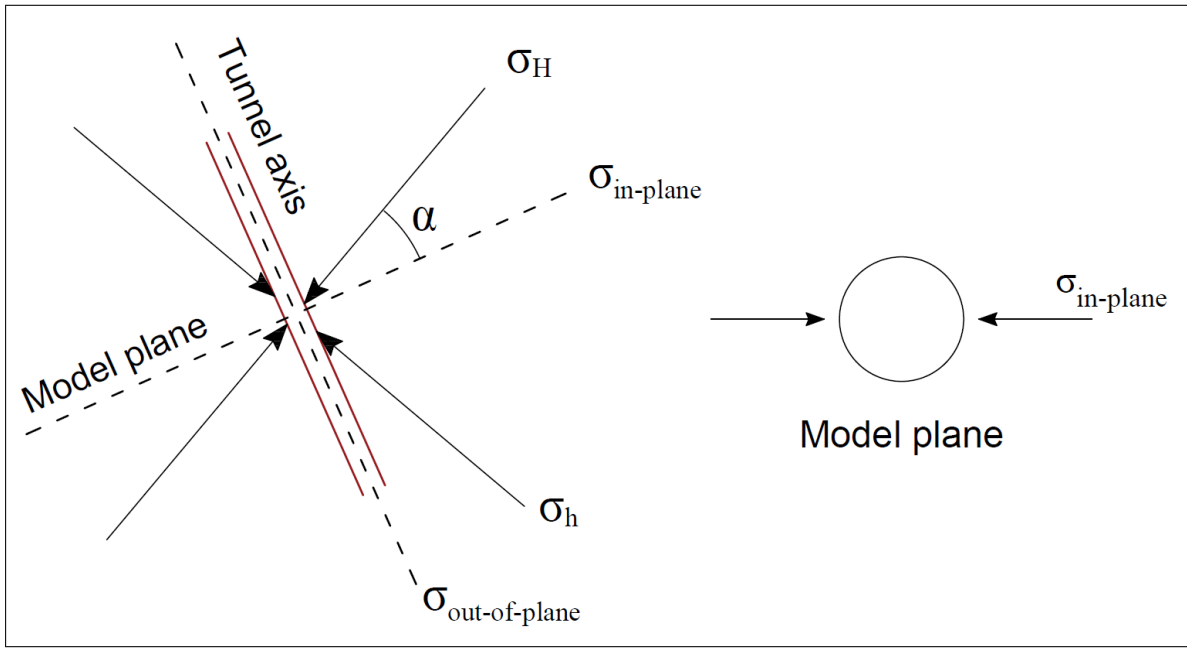


Figure 9.8: Resolving horizontal stresses into the model plane. α is the angle between the maximum horizontal stress and the model plane.

Chapter 10

Stability analyzes

10.1 Introduction

In this chapter stability analyzes of the identified instability issues in the headrace tunnel at Brattset are carried out. Both empirical and analytical methods, as well as numerical modelling, have been applied to analyze four different modes of failure. The empirical methods involve estimations of the potential to spalling, and the analytical analysis is carried out as a limit equilibrium analysis. Finally, numerical modelling has been used to analyze instability issues in both two and three dimensions. Although several of the identified issues are observed at multiple locations along the tunnel, one typical location is chosen for each of the different issues for use in the analyzes. Also, since the headrace tunnel is mainly unlined, the analyzes are carried out without any form of installed support. The exception is the numerical analysis of the weakness zone, where a shotcrete layer is applied on the tunnel wall to simulate the support that was installed during construction of the tunnel in 1980-82.

10.1.1 Software for numerical modelling

The software applied for the numerical modelling in this thesis is provided by Rocscience Inc. Modelling in 2D is carried out as plane strain analysis in RS² version 9. RS² is a two-dimensional finite element program, which can be used for analyzing a wide range of engineering structures in rock and soil (Rocscience Inc., 2018[a]). It is assumed that the reader has basic knowledge of the various functions and features of the program. The applied features and options will therefore only be described briefly. For further details on the usage of the program, the reader is referred to the RS² Webhelp page (Rocscience Inc., 2018[a]).

For modelling in 3D, the program RS³ is used. RS³ is a finite element program for 3D analysis, with functions and a user interface that is very similar to RS². In the same way as for RS², the user is referred to the RS³ Webhelp page for further details (Rocscience Inc., 2018[b]).

Table 10.1: Identified instability issues and analysis method

#	Description	Involved rock mass	Chainage	Tunnel depth	Method
1	Stress induced spalling/buckling	Phyllite	3800	183 m	Empirical/analytical
2	Wedge fall, caused by intersecting discontinuities	Quartz keratophyre	9700	233 m	Limit equilibrium
3	The effect of schistosity to buckling	Phyllite	3800	183 m	2D numerical
4	Block fall caused by joints and induced fracturing	Phyllite	10 400	231 m	2D numerical
5	Collapse in weakness zone	Phyllite and weathered material	1200	155 m	3D numerical

10.2 Potential to stress induced instability

Several methods have been proposed for evaluating the potential for stress induced instabilities in underground excavations. Panthi (2017) presented four commonly used methods for prediction of rock bust activity in underground tunnels and mines. Of these, two will be further discussed and applied here to assess the potential of spalling in the headrace tunnel at Brattset: *Stress potential classification by the Q-system* and the *maximal tangential stress and rock spalling strength approach*. Later in this chapter, the spalling behaviour will also be analyzed by numerical modelling.

10.2.1 Stress potential classification by the Q-system

In the Q-system Barton et al. (1974), instability issues associated with stresses are taken into account by the SRF parameter (Strength Reduction Factor). The parameter is estimated based on three input parameters: compressive strength of intact rock σ_{ci} , the major principle stress σ_1 and the maximum tangential stress $\sigma_{\theta max}$. The classification of the spalling potential in the Q-method is based on experience from several underground projects in Norway and abroad (NGI, 2015).

In Table 10.2 the different stress conditions are presented as ratios between the input parameters, with the corresponding stress induced instabilities for competent rock mass. In order to assess the potential issues by this method, one should perform laboratory testing of intact rock and the in-situ stress conditions of the area should be known (Panthi, 2017).

Table 10.2: Potential stress problems in competent rock mass, based on the Q-system (NGI, 2015)

Potential stress induced instability	σ_{ci}/σ_1	$\sigma_{\theta max}/\sigma_{ci}$	SRF
Low stress, near surface, open joints. May cause loss of confinement	> 200	< 0.01	2.5
Medium stress, favourable stress conditions	200-10	0.01-0.3	1
High stress, usually favourable to stability. Unfavourable orientation of stresses compared to jointing/weakness planes may cause issues	10-5	0.3-0.4	0.5-5
Moderate spalling and/or slabbing after > 1 hour	5-3	0.5-0.65	5-50
Spalling or rock burst after a few minutes	3-2	0.65-1	50-200
Heavy rock burst and immediate dynamic deformation	< 2	> 1	200-400

10.2.2 Maximal tangential stress and rock spalling strength approach

The excavation process leads to loss of confinement of the rock mass adjacent to the tunnel, which increase the susceptibility to spall fracturing (Diederichs, 2014). Martin and Christiansson (2009) suggested that cracking is initiated in crystalline rocks at stress levels of around 40-60 % of the intact uniaxial compressive strength, providing a lower bound limit for the rock mass spalling strength (σ_{sm}). According to Diederichs (2014), spalling damage occur at tunnel walls at stresses around 0.4-0.6 times the intact laboratory strength, while Panthi (2006) proposes that one can assume that the rock mass spalling strength is likely to be lower than 50 % of the mean uniaxial compressive strength (UCS). For rock mass influenced by schistosity Panthi (2017) suggests that the spalling strength σ_{sm} can be replaced by the rock mass strength σ_{cm} , which is expressed by:

$$\sigma_{cm} = \frac{\sigma_{ci}^{1.5}}{60} \quad (10.1)$$

To estimate the depth impact of spalling/rock burst in the wall of a circular tunnel, Martin and Christiansson (2009) proposed the following equation:

$$S_d = r \left(0.5 \frac{\sigma_{\theta max}}{\sigma_{sm}} - 0.52 \right) \quad (10.2)$$

where the r is the tunnel radius and S_d is the depth of spalling measured from the boundary of the tunnel, as illustrated in Figure 10.1.

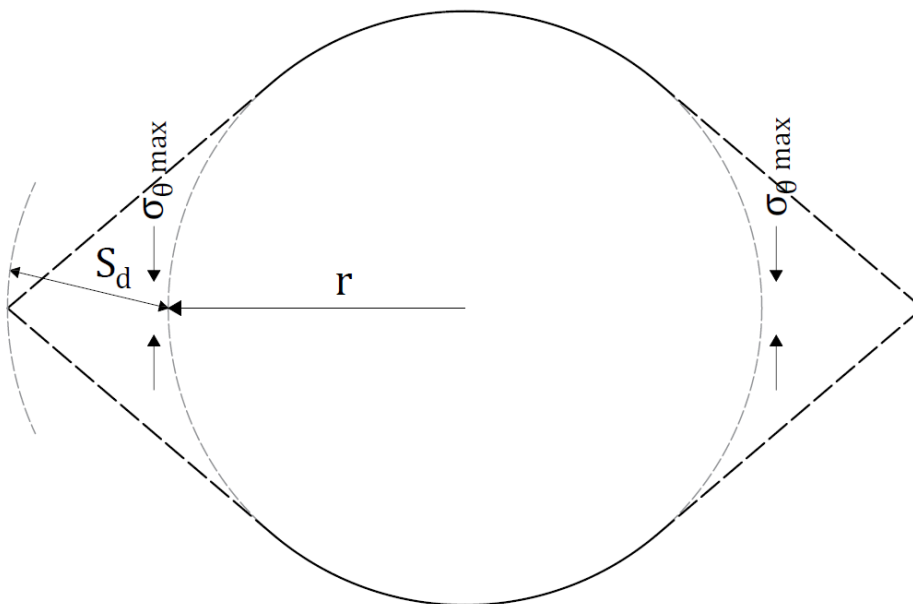


Figure 10.1: Potential depth impact in the wall of a circular tunnel caused by a major induced tangential stress. Parameters are related to Equation (10.2).

10.2.3 Stress conditions

In order to perform an assessment of the spalling potential, the stress situation at the specific location must be determined. Stresses at the tunnel location is calculated according to Equation (9.5) and the chosen stress ratios. From running an elastic stress analysis in topographic model at chainage 3800, it was found that the stresses at the tunnel location are not affected by topography. This means that the horizontal stresses can be regarded as principal stresses. The maximum tangential stress is calculated from the resolved component of the principal stresses acting normal to the tunnel axis and the vertical stress. The stress conditions used in the analysis are summarized in Table 10.3.

Table 10.3: Calculated stresses at chainage 3800

Parameter	Description	Value	Unit	Source
z	Tunnel depth	183	m	
γ_0	Average overburden unit weight	0.03	MN/m ³	
σ_v	Vertical stress	5.5	MPa	Eq. (3.11)
k	Stress ratio	2.8 / 1.07		Table 9.3
$\sigma_H = \sigma_1$	Major horizontal stress	15.4	MPa	
σ_h	Minor horizontal stress	5.8	MPa	
σ_{XX}	In-plane horizontal stress	13.6	MPa	Eq. (9.6)
σ_Z	Out-of-plane horizontal stress	7.1	MPa	Eq. (9.7)
$\sigma_{\theta max}$	Maximum tangential stress	35.3	MPa	Eq. (3.15)

10.2.4 Results

It is chosen to analyze the spalling potential for what is assumed to be a strong, unsaturated phyllite and for a weaker, saturated phyllite. This is done to study any differences in the spalling potential from the time when the tunnel was just excavated and until the tunnel has been operated over longer time. The buckling and spalling behaviour is by Blindheim (1982) described to appear in schistose phyllite. It is therefore assumed that the phyllite is of low to moderate quality and strength parameters are assigned values in the lower part of the presented ranges in Table 9.2. The reduction of intact rock strength due to saturation is assumed to be 30 %. The results from using the two methods are presented in Tables 10.4 and 10.5.

Table 10.4: Result from spalling potential analysis by Q -system

	σ_{ci} (MPa)	σ_{ci}/σ_1	$\sigma_{\theta max}/\sigma_{ci}$	Spalling potential
Unsaturated phyllite	90	5.8	0.39	High stress, usually favourable. Unfavourable jointing/weakness planes may cause issues
Saturated phyllite	63	4.1	0.56	Moderate spalling after > 1 hour

Table 10.5: Result from spalling potential analysis by S_d . Tunnel radius r is 2.25 m, σ_{sm} is estimated according to Equation (10.1).

	σ_{ci} (MPa)	σ_{sm} (MPa)	Depth impact S_d (m)
Unsaturated phyllite	90	14.2	1.6
Saturated phyllite	63	8.3	3.6

10.3 Limit equilibrium analysis of wedge fall

Structurally controlled failures have been reported from multiple locations along the head-race tunnel. Many of these are blocks and wedges have been sliding or falling from the tunnel wall and crown, respectively. In this analyze the limit equilibrium method will be applied on a wedge falling from the crown.

The limit equilibrium analysis is a commonly applied method in engineering geology practice (Nilsen and Broch, 2012). The method involves a simplified geometrical model of a single block or wedge, with mathematical calculations to determine the critical point of failure. This critical point is referred to as the point of equilibrium and is the state where driving forces acting on the block or wedge are equal to the resisting forces along the discontinuity planes (Wyllie and Mah, 2004).

The ratio between the resisting and driving forces is expressed by *Factor of safety (FS)*. If the factor of safety is below 1.0, the driving forces exceed the resisting force and wedge fall occur. If the factor of safety is larger than 1.0, the resisting forces exceed the driving forces, and the wedge is stable (Wyllie and Mah, 2004). It is however always a degree of uncertainty associated with the input parameters in such an analysis. Thus, in rock engineering practice it is often required that the factor of safety is above a fixed value larger than 1.0, to account for the uncertainties. Nilsen (1999) suggests some commonly used values of the factor of safety for different construction types:

- Short term stability (e.g. temporary walls in a quarry): $FS \geq 1.3$
- Long term stability (e.g. permanent walls in a quarry): $FS \geq 1.5$

In order to obtain workable solutions, it is necessary to do a series of simplifying assumptions. These are explained by Goodman and Shi (1985), and can be summarized as follows:

1. All joint surfaces are assumed to be perfectly planar
2. All joints extend entirely through the volume of interest, no joint is to terminate inside the block and no new cracking is involved in the block movement
3. The blocks defined by the joint surfaces are assumed to be rigid. No block deformation and distortion are introduced
4. Discontinuities and excavation surfaces are determined as input parameters

The aim of the analysis is to study the stability of the block for different joint conditions. The effect of weathering to the rock strength and the reduction of friction angle due to alteration will be compared. The effect of water pressure inside the joint will also be considered.



Figure 10.2: Jointing in quartz keratophyre. The three joint sets are nearly orthogonal, forming cubical blocks.

10.3.1 Model geometry

The quartz keratophyre intrusions generally show three pronounced joint sets. The joint sets are oriented nearly orthogonal to each other, such that cubic blocks are formed in the rock mass, as illustrated in Figure 10.2. The reported volumes from block falls range from 0.5 m³ to 2 m³ (Skoglund, 2008; Midtlyng, 2015). In the equilibrium analysis, it is therefore chosen to consider a block formed by three joint sets, with 1.5 m spacing in the model plane.

The model geometry is illustrated in Figure 10.3. The considered wedge is located in the tunnel crown, and is defined in the plane by two intersecting joint sets, dipping 60°NE and 60°SW. The third joint set, which is assumed to be vertical, strikes normal to the tunnel axis and defines the block depth d to be 1 m into the plane. The geometry of the block is chosen to be symmetrical about the centre line, to simplify the calculations. In the analysis, the curvature of the tunnel wall is ignored, such that the block is shaped as a triangle. The necessary measures are given in Table 10.6

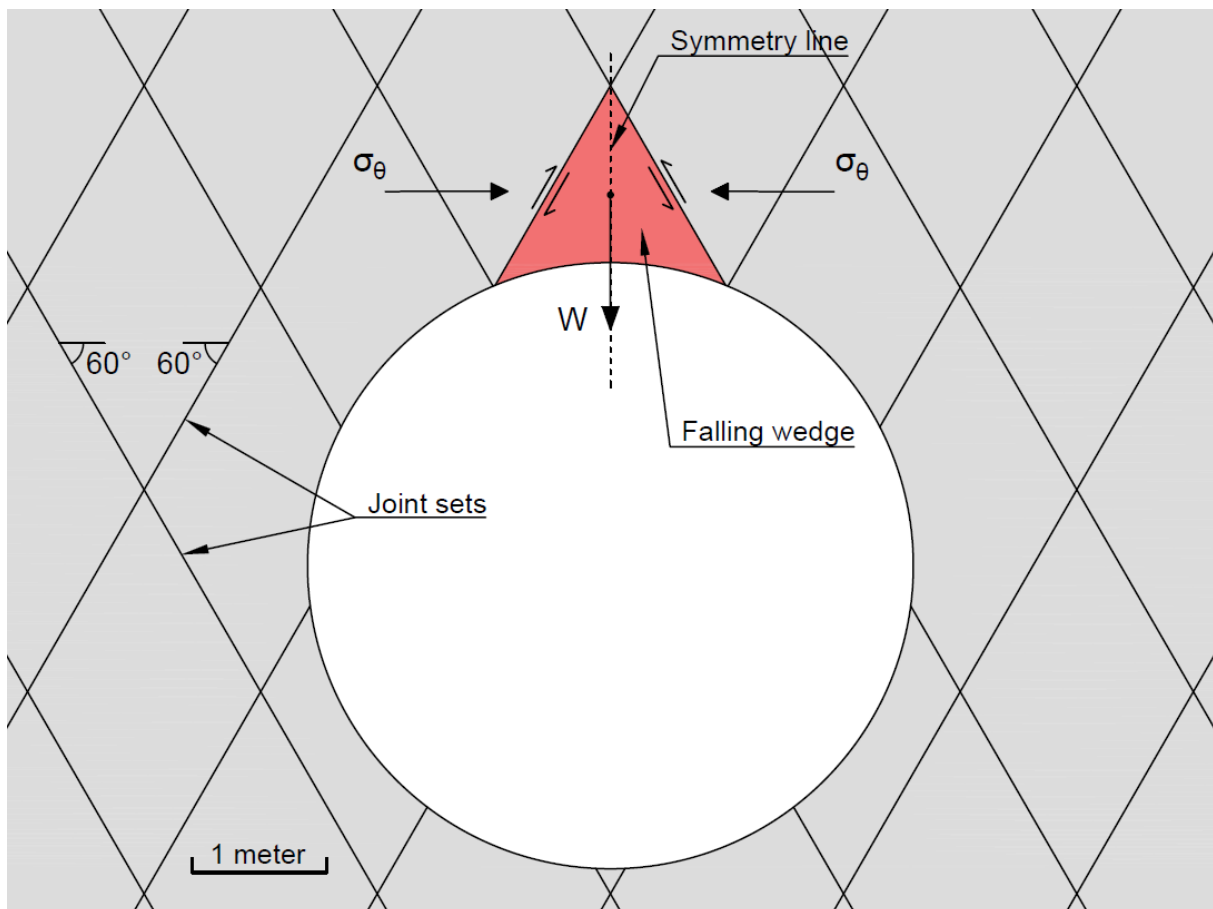


Figure 10.3: Model geometry of wedge fall analysis

Table 10.6: Wedge measures

Parameter	Description	Calculation	Value	Unit
L	Joint spacing		1.50	m
β	Joint dip		60	deg
α	Calculation angle	$90 - \beta$	30	deg
d	Edge depth		1.00	m
l	Edge length	$L / \cos \alpha$	1.73	m
A	Edge area	$l \cdot d$	1.73	m ²
h	Wedge height	$L \cos \alpha$	1.50	m
V	Volume	$d h^2 \tan \alpha$	1.30	m ³
γ_r	Unit weight		26.5	kN/m ³
W	Wedge weight	$\gamma_r V$	34.4	kN

10.3.2 Identification of forces

The forces involved in the limit equilibrium analysis are normal and shear forces (N, U, S), as well as the wedge weight (W). Since no specific support measures are involved in the stability issues at Brattset, any anchor forces are ignored. The forces acting on the wedge are illustrated in Figure 10.4. By resolving the driving and resisting forces into components parallel with the direction of movement, the point of equilibrium can be expressed as follows (Elsworth, 1986):

$$\text{Driving forces} = \text{Resisting forces} \tag{10.3}$$

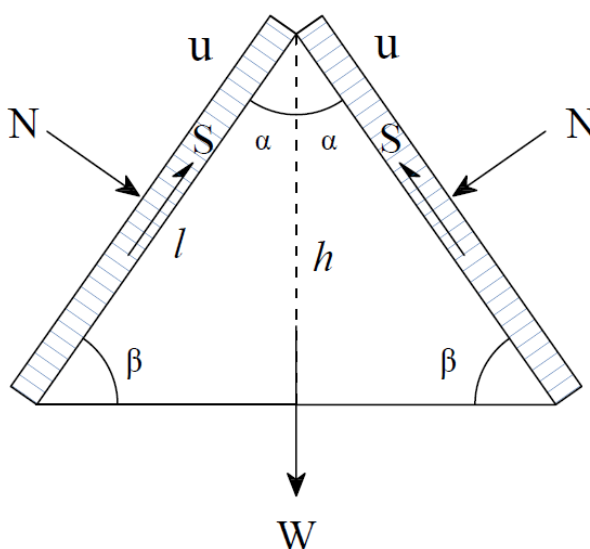


Figure 10.4: Forces acting on the wedge

Driving forces

The resultant force acting vertically, in the direction of movement, is termed the driving force. According to Nilsen and Broch (2012) the driving force is due to gravity (weight of the block), water pressure in joints and seismic activity. In addition will the normal force due to the in-situ stresses, have a component in the vertical direction. Seismic activity will not be considered here. Hence, the driving force is defined by the wedge weight, water pressure in joints and the vertical component of the normal forces (Elsworth, 1986):

$$D = W + 2U \sin \alpha + 2N \sin \alpha \quad (10.4)$$

The water pressure in the joints is assumed to arise from mass oscillations inside the tunnel system. To simulate the most critical pressure that may occur, the peak-to-peak amplitude of 167 m is adopted, such that the modelled force from pore water pressure is:

$$U = u \cdot A = 1.64 \text{ MPa} \cdot 1.73 \text{ m}^2 = 2.8 \text{ MN} \quad (10.5)$$

Since the principal stresses in the vicinity of the tunnel are horizontal, the maximum tangential stresses will be located in the crown and in the floor. The radial and axial stresses are low compared to the tangential stress, and are assumed to be of little importance regarding the block stability. Hence, only the tangential stress will be included in the analysis. The tangential stress is found by inserting the in-plane horizontal stress into Equation (3.14), see Table 10.7. The normal force N on each edge of the wedge, caused by the tangential stress, is given by (Li, 2015a):

$$N = \sigma_n^\theta \cdot A = \sigma_\theta \cos^2 \alpha \cdot A \quad (10.6)$$

Table 10.7: *Calculated stresses at chainage 9700*

Parameter	Description	Value	Unit
z	Tunnel depth	233	m
γ_0	Average overburden unit weight	0.03	MN/m ³
σ_v	Vertical stress	7.0	MPa
k	Stress ratio	2.8 / 1.07	
σ_H	Major horizontal stress	19.6	MPa
σ_h	Minor horizontal stress	7.5	MPa
σ_{XX}	In-plane horizontal stress	17.2	MPa
σ_θ	Tangential stress	44.8	MPa

Resisting forces

The shear force S along the discontinuity planes will counteract the driving forces and defines the resisting force. The joint surfaces exhibit a frictional resistance, which is controlled by the shear strength τ . At the point of equilibrium, the shear strength of the joints equals the shear stress (Elsworth, 1986). Hence, if the shear force S is replaced by the resisting force R in Equation (10.3), the factor of safety FS against block fall can be defined as the ratio:

$$FS = \frac{\text{Resisting forces}}{\text{Driving forces}} = \frac{2 R \cos \alpha}{W + 2(U + N) \sin \alpha} \quad (10.7)$$

where $R = \tau \cdot A$.

The shear strength of unfilled joints is governed by the joint roughness, the compressive strength of the joint wall and the normal stress acting on the joint surface. The relation is defined by the Barton-Bandis empirical model (Barton and Bandis, 1990):

$$\tau = \sigma_n \tan \left[JRC \cdot \log \frac{JCS}{\sigma_n} + \phi_r \right] \quad (10.8)$$

here JRC is the joint roughness coefficient, JCS is the joint compressive strength and ϕ_r is the residual friction angle. These values need to be determined by a combination of field and laboratory work. Since the gravity force of the wedge and the pore water pressure reduce the normal stress on the discontinuity plane, σ_n is given by (Li, 2015a):

$$\sigma_n = \sigma_n^\theta - \sigma_n^w - \sigma_n^p = \sigma_\theta \cos^2 \alpha - \frac{W \cos \alpha}{A} - \frac{U}{A} \quad (10.9)$$

Input parameters for Equation (10.8) are given in Table 10.8. The given values are estimated for strong, unweathered joints. Weakening of the joint will be simulated by reducing the values of JRC, JCS and ϕ_r in the calculation.

Table 10.8: *Input parameters in the Barton-Bandis model for strong joint*

Parameter	Description	Value	Source
JRC	Rough, planar	2.5	Figure 9.2
JCS	UCS of rock	102 MPa	(Neupane, 2017)
ϕ_r	Unaltered, $J_a = 1$	35°	Figure 9.1
σ_n	Normal stress on joint	31.9 MPa	Equation (10.9)

10.3.3 Results

In this limit equilibrium analysis, the effect of altered joint conditions are studied. The shear strength of joints is estimated by the Barton-Bandis empirical model, where the joint roughness coefficient (JRC), joint compressive strength (JCS) and residual friction angle ϕ_r are the governing parameters. The contribution to stability of each parameter is studied by reducing the value of the shear strength parameter, one at a time. The following ranges are applied:

1. Reduction of JRC from rough, planar joint to slickensided, planar joint, (2.5 – 0.5)
2. Reduction of JCS from intact (UCS) to extremely weathered (90 % strength loss), (102 – 10.2 MPa)
3. Reduction of ϕ_r from unaltered joint to joint with softening or low friction clay filling, ($35 - 12.5^\circ$)

Keeping all input parameters but JRC, JCS and ϕ_r constant, the resisting and driving forces are calculated as described. For a strong, unweathered joint the acquired factor of safety is 1.15, see Figure 10.5. Although this value does not meet any of the requirements suggested above, the wedge is so far considered stable.

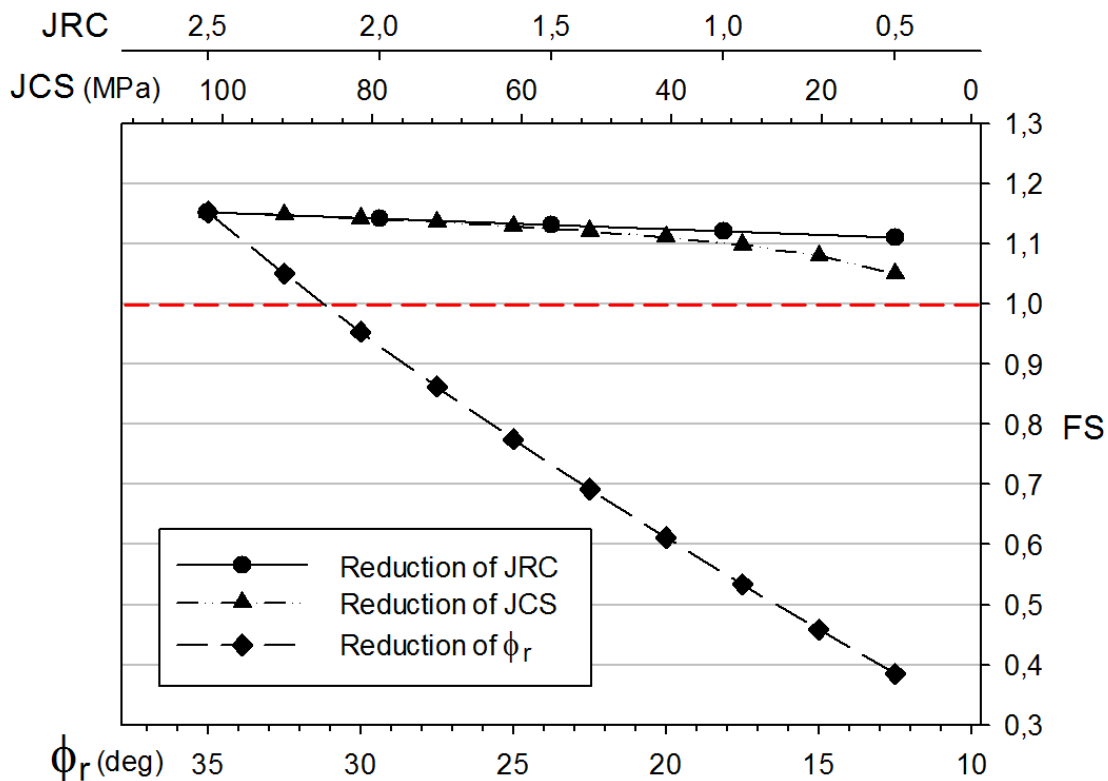


Figure 10.5: Results from limit equilibrium analysis of block fall. The change in factor of safety for reduced JRC, JCS and ϕ_r .

In Figure 10.5 consequences of modified joint conditions is illustrated. As seen in the figure, the factor of safety (FS) is not significantly affected by reduction of JRC or JCS, respectively, and FS remains larger than 1.0 for all values in the given ranges. Reduction of ϕ_r gives a significantly larger effect. Already with a slightly altered joint ($\phi_r = 25 - 30^\circ$) the factor of safety becomes below 1.0 (FS = 0.78-0.95), and the wedge is in an unstable state. Further alteration of the joint gives an additional decrease of the FS.

10.4 Spalling and buckling in schistose phyllite

The susceptibility to stress induced issues are also studied through numerical modelling. In this case the rock mass is assumed to be saturated, such that the spalling/buckling behaviour can be compared to what has been observed in the headrace tunnel during the last inspections.

10.4.1 Model set up

Two cross sectional models of the tunnel are created in RS². The external boundaries of the models are placed with sufficient distance from the tunnel, and restrained in both X and Y direction. Both continuum and discontinuum modelling are carried out. The first model is a continuum model, where the rock material is regarded as one homogeneous mass. In the discontinuum model, a joint network is introduced to serve as the foliation in the phyllite. The model geometries are shown in Figure 10.6. The foliation joints are inserted into the model with the mean dip of 42° and a joint spacing of 20 cm.

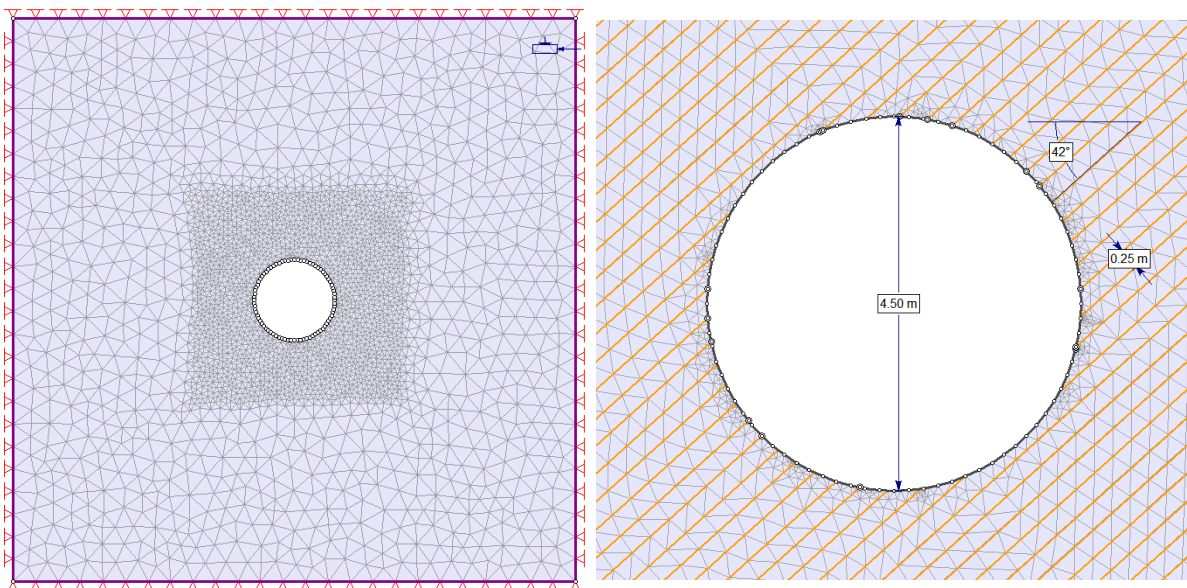


Figure 10.6: Model geometry for spalling analysis in RS². Full continuum model (left), and detailed discontinuum model (right), looking upstream.

10.4.2 Input parameters

Stress conditions

Stresses at the tunnel location are calculated above, in the empirical analysis above, and can be found in Table 10.3. The resolved stresses for the model are given below:

Table 10.9: Resolved stresses at chainage 3800

Parameter	Description	Value	Unit
σ_v	Vertical stress	7.0	MPa
σ_{XX}	In-plane horizontal stress	13.6	MPa
σ_Z	Out-of-plane horizontal stress	7.1	MPa

Rock mass and joint properties

The studied rock mass is the same as the saturated phyllite presented in the spalling potential analysis above. The phyllite has low to moderate quality, and the strength parameters are chosen from the lower part of the presented ranges in Table 9.2. The Baron-Bandis model is applied for the joint slip criterion. Since it was observed some thin chlorite filling during field work, ϕ_r is set to 15, and the joint wall strength is assumed to be 50 % of σ_{ci} . According to Blindheim (1982) there was observed a few occurrences of slickensided foliation planes in the schistose phyllite, hence the JRC value is set to 0.5. Rock mass deformation modulus and parameters for the Mohr-Coulomb criterion are calculated using RocData, and residual values are found based on the method of GSI_r proposed by Cai et al. (2007). Input rock mass and joint properties are given in Tables 10.10 and 10.11, respectively.

Table 10.10: Input parameters for phyllite

Parameter	Description	Peak value	Residual value	Unit
$\sigma_{ci,sat}$	Intact strength, saturated	63	–	MPa
GSI	Geological strength index	50	20	–
m_i	Material constant	5	–	–
E_{ci}	Intact def. modulus	35	–	GPa
ν	Poisson's ratio	0.15	–	–
T_0	Tensile strength	0.2	0	MPa
ϕ	Friction angle	40.5	30.1	deg
c	Cohesion	1.0	0.4	MPa
E_m	Rock mass modulus	10.8	–	GPa
	Dilation angle	–	18	deg

Table 10.11: Estimated values of foliation joint properties

Parameter	Description	Value	Unit	Source
E_{ci}	Intact deformation modulus	35	GPa	Table 9.2
E_m	Rock mass def. modulus	10.8	GPa	
ν	Poisson's ratio	0.15	–	Table 9.2
G_i	Intact shear modulus	15.2	GPa	Eq. (9.3)
G_m	Rock mass shear modulus	4.7	GPa	Eq. (9.3)
L	Mean joint spacing	0.20	m	
K_n	Joint normal stiffness	78.1	GPa	Eq. (9.1)
K_s	Joint shear stiffness	34.0	GPa	Eq. (9.2)
JCS	Joint wall strength	31	MPa	
JRC	Joint roughness	0.5	–	Figure 9.2
ϕ_r	Residual friction angle	15	deg	Figure 9.1

10.4.3 Modelling results

From running the continuum model, the depth impact of spalling around the tunnel is studied. Figure 10.7 shows that yielding of the rock mass elements occurs around the whole tunnel periphery, developing a plastic zone where the rock mass has partly or completely failed. The area of yielded elements is extending from the tunnel crown and floor in the direction of the minor in-plane stress. The measured depth impact in the model is 3.63 m.

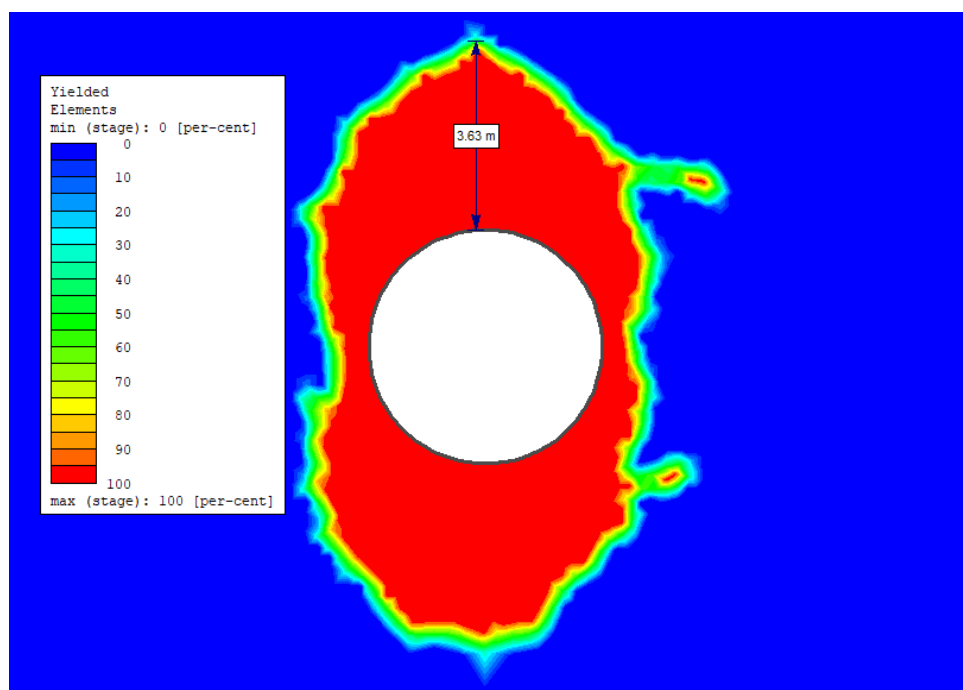
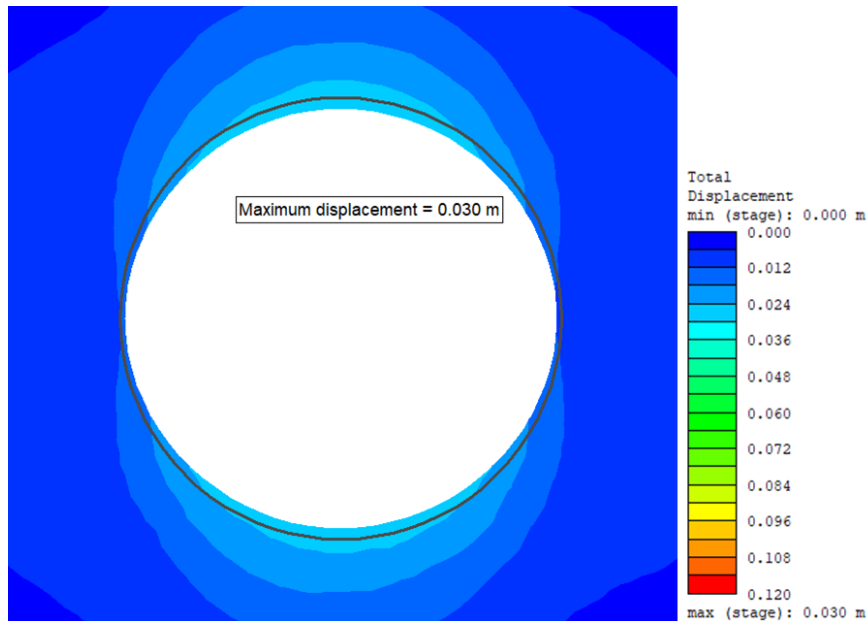
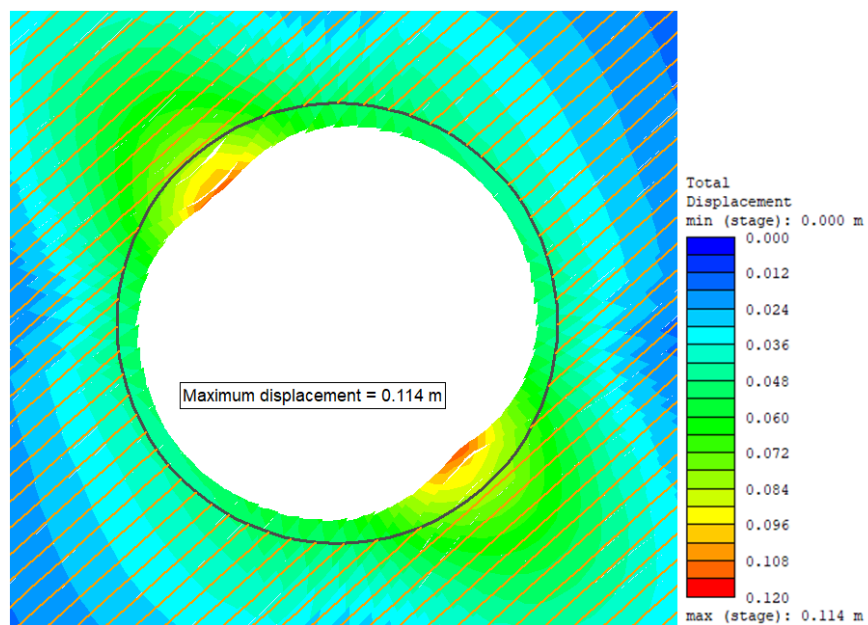


Figure 10.7: Yielded elements around the tunnel opening in continuum model. The maximum depth impact is 3.63 m

The discontinuum model is used to study the effect of foliation to the spalling behaviour. In Figure 10.8 the deformation in each of the two models is compared. In the continuum model the deformation appears in the tunnel crown and floor. When foliation joints are introduced in the discontinuum model, the deformation is relocated to the tunnel abutment and upper wall, appearing parallel to the foliation plane. It should also be noted that the total displacement is larger in the discontinuum model, as the material elements are allowed to slip and detach from each other along the joints.



(a) Continuum model without foliation joints



(b) Discontinuum model, where foliation joints are present

Figure 10.8: Effect of schistosity to buckling behaviour. Scale factor = 4.

10.5 Block fall caused by joints and induced fracturing

Large volumes of failed rock that have slid along a joint or seam have been observed during the tunnel inspections in both 2008 and 2015. The identified instability issue is assumed to be a result of both shear failure along joints and the failure of intact rock due to induced stresses. Using numerical modelling, the possible failure mechanisms involved are evaluated, and the effect of joint weakening to the mode of failure is analyzed.

10.5.1 Model geometry and setup

A cross-sectional model of the tunnel is created in RS². The external boundaries of the model are placed with sufficient distance from the tunnel and restrained in both X and Y directions. Figure 7.16 show a photo taken at the location of failure. Sliding of the blocks occurred along one continuous joint, which can be seen dipping into the tunnel wall. To simulate the situation a joint network is added into the model, with joint spacing of 4.5 m, such that one joint is located in the tunnel wall in the same way as in the photo.

The model is run with two different input sets for the joint. The first run represents the conditions where no weakening of joints has taken place. In the second run the joint intersecting the tunnel contour is assigned different joint properties than the ones that is located outside of the tunnel periphery. This was done to simulate the reduction in joint strength due water flow in the tunnel during operation.

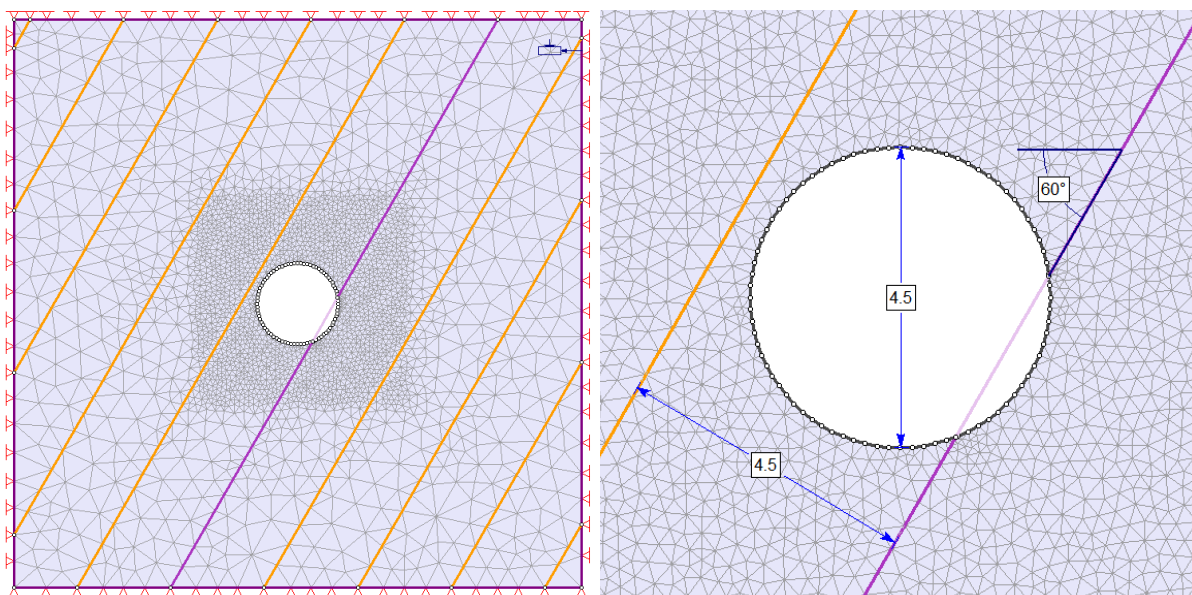


Figure 10.9: Model geometry for analysis of induced fracturing and joint. Full model (left) looking upstream, and detailed measures (right). The weak joint in purple.

10.5.2 Input parameters

Stress conditions

Stresses at the tunnel location are calculated according to Equation (9.5) and the chosen stress ratios, and resolved into the model plane. From running a topographic model, it is confirmed that the stresses are not affected by topography. The stress conditions used in the analysis are summarized in Table 10.12.

Table 10.12: Calculated stresses at chainage 10 400

Parameter	Description	Value	Unit
z	Tunnel depth	224	m
γ_0	Average overburden unit weight	0.03	MN/m ³
σ_v	Vertical stress	6.7	MPa
k	Stress ratio	2.8 / 1.07	
σ_H	Major horizontal stress	18.8	MPa
σ_h	Minor horizontal stress	7.2	MPa
σ_{XX}	In-plane horizontal stress	16.6	MPa
σ_Z	Out-of-plane horizontal stress	9.4	MPa

Rock mechanical properties

The rock mass in this case is assumed to be of the quartzitic phyllite. It seems to be quite massive, with few open joints or seams. The intact rock strength is set in the higher end of the estimated range in Table 9.2, and a high GSI value is chosen since the spacing of joint is relatively large. Again are the Mohr-Coulomb parameters calculated using RocData, and the residual values are found based on the GSI_r method. The input values for the rock mechanical properties are given in Table 10.13.

Joint properties

Joint properties are determined for both strong joints and for a weakened joint. The weakening of the joint in contact with the tunnel is assumed to be a result of reduced rock mass strength due to saturation, alteration of the joint wall and washing of the joint filling material. Additional pressure is applied inside the weak joint, to simulate the water pressure that may arise due to mass oscillation. The effect of the differential pressure that can develop is studied through running the model with values varying from 0 to 167 m water pressure, equivalent to 0-1.6 MPa.

The normal and shear stiffness of joints is dependent of the rock mass modulus. For the weak joint the empirical formula given by Panthi (2006) is used to estimate the rock mass modulus. With this formula a lower value of E_m is obtained than the value calculated from RocData. The lower E_m would represent a weakened rock mass along the joint.

The shear strength of the joints is estimated with the Barton-Bandis model. The joints in the quartzitic phyllite are generally rough and planar, and a JRC value of rough, planar joint is adopted for both strong and weak joints. The weakening of the joint intersecting the tunnel is done by reduction of the joint wall strength by 80 % (highly weathered) and the residual friction angle to a value representing small clay fraction coatings (20°). The weak joint properties are only assigned to the joint intersecting the tunnel in the second run of the model, while all other joints kept with the same properties as for strong joints.

Table 10.13: Input parameters for phyllite

Parameter	Description	Peak value	Residual value	Unit
$\sigma_{ci,sat}$	Intact strength, saturated	90	–	MPa
GSI	Geological strength index	65	35	–
m_i	Material constant	7	–	–
E_{ci}	Intact def. modulus	35	–	GPa
ν	Poisson's ratio	0.15	–	–
T_0	Tensile strength	0.9	0	MPa
ϕ	Friction angle	46.2	38.5	deg
c	Cohesion	2.4	0.9	MPa
E_m	Rock mass modulus	22.1	–	GPa
	Dilation angle	–	22	deg

Table 10.14: Estimated values of joint properties

Parameter	Description	Strong joint	Weak Joint	Unit	Source
E_{ci}	Intact deformation modulus	35	35	GPa	Table 9.2
E_m	Rock mass def. modulus	22.1	5.5	GPa	
ν	Poisson's ratio	0.15	0.15	–	Table 9.2
G_i	Intact shear modulus	15.2	15.2	GPa	Eq. (9.3)
G_m	Rock mass shear modulus	9.6	2.4	GPa	Eq. (9.3)
L	Mean joint spacing	4.5	4.5	m	
K_n	Joint normal stiffness	13.32	1.45	GPa	Eq. (9.1)
K_n	Joint shear stiffness	5.79	0.63	GPa	Eq. (9.2)
JCS	Joint wall strength	70	14	MPa	
JRC	Joint roughness	2.5	2.5	–	
ϕ_r	Residual friction angle	35	20	deg	
p	Water pressure in joint	0	0-1.6	MPa	

10.5.3 Results

Two different simulations were carried out, in order to study the effect of the joint strength to the mode of failure. The joint intersecting the tunnel is in direct contact to the flowing water within the tunnel, and is assumed to be the only joint that is affected and weakened by water.

Strong joints

In this model all joints have the properties of a strong joint. No alteration and washing of the joint have occurred, and it is assumed that the joint is sealed, such that water will not flow inside the joint during mass oscillations. The result from the simulation is shown in Figure 10.10. The figure show that yielding of the rock mass occurs in the tunnel crown and floor, and that joint elements near the tunnel contour have yielded slightly (red color). The maximum total displacement of 2.6 cm occurs in the tunnel crown. The maximum normal and shear displacements of the joint intersecting the tunnel are both 0.1 cm, which can be considered as negligible.

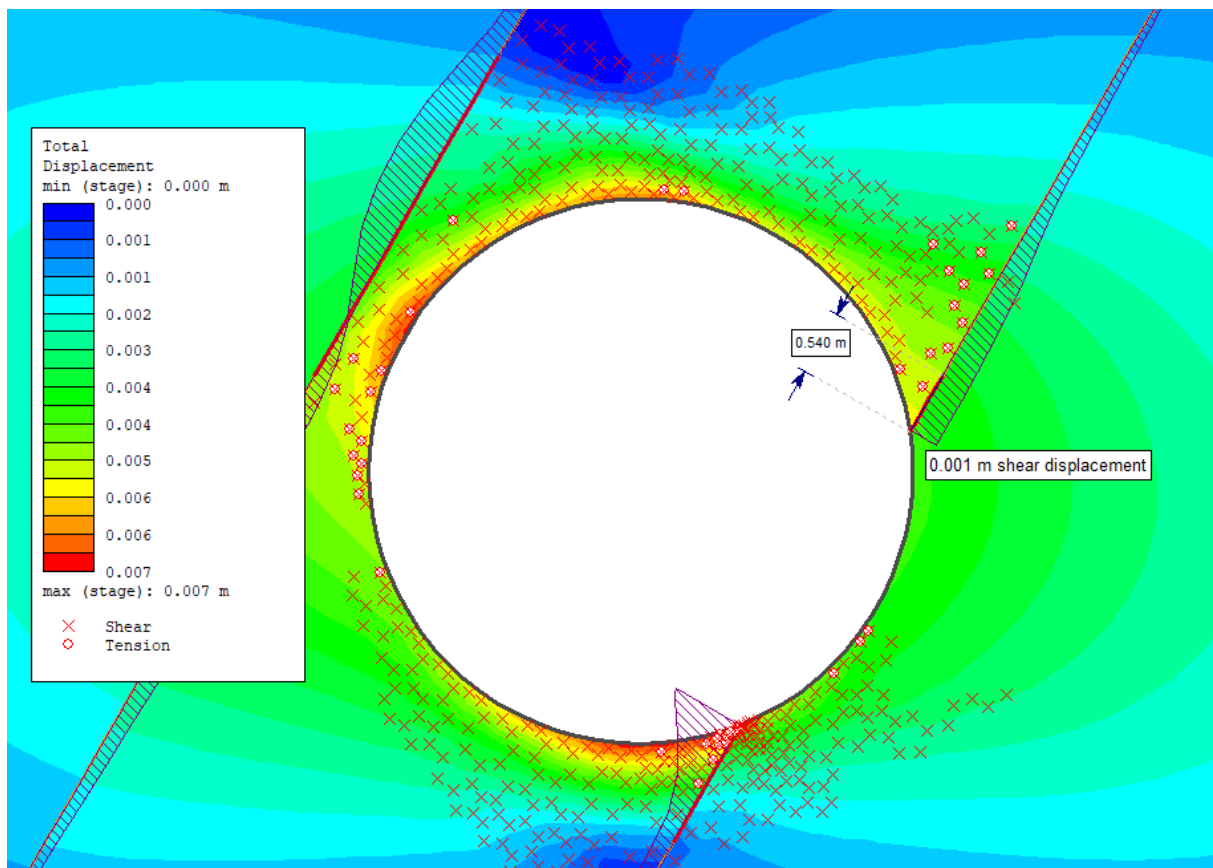


Figure 10.10: Yielded elements and shear displacement of strong joint

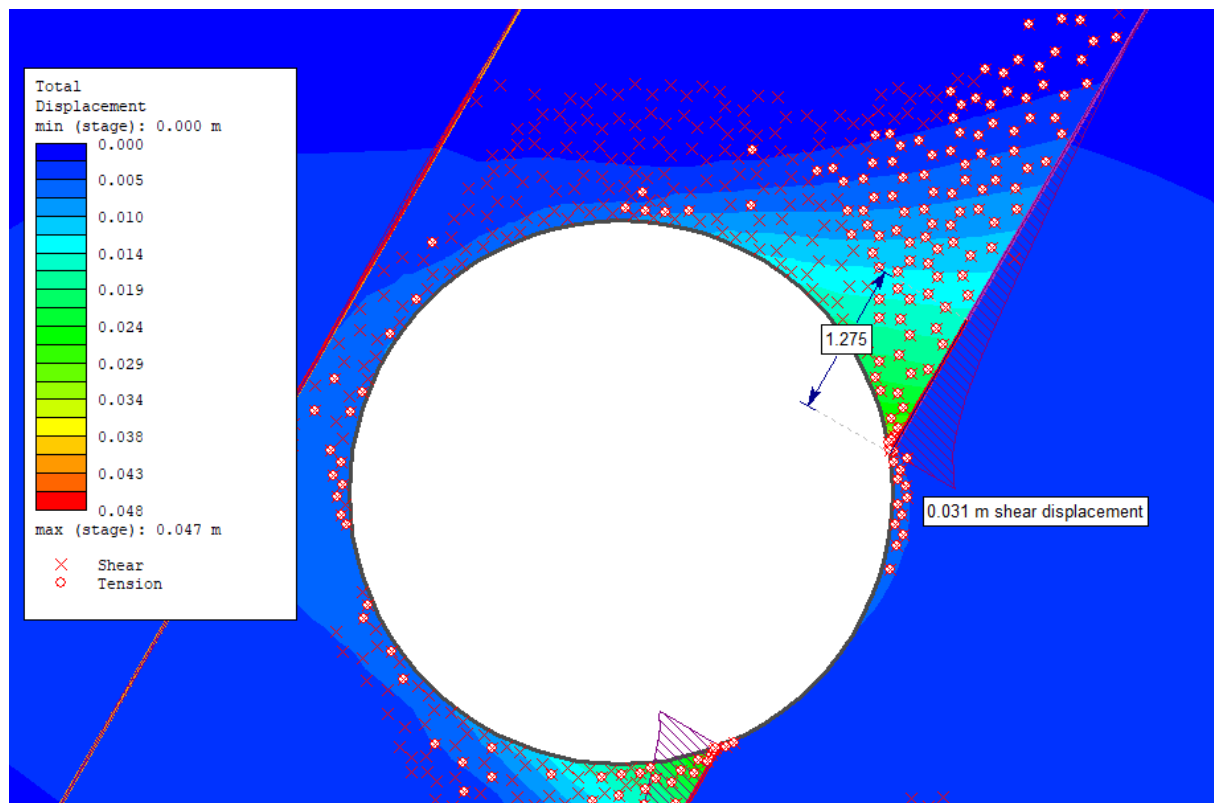


Figure 10.11: Yielded elements and shear displacement of weak joint when no water pressure is applied

Weak joint

In the second run of the model, the properties of the joint intersecting the tunnel are reduced, to simulate the alteration of the joint walls and joint filling. All other joints are kept strong. The result of the simulation, with no additional pressure inside the weak joint, show that the yielding of the rock mass has increased. Yielding of the rock mass has increased near the weak joint, and there is a larger number of elements failed by tension closer to the joint. A longer section of the joint has also yielded. The maximum deformation of 8.6 cm is now located in the tunnel wall, and the normal and shear stress along the joint is 1.8 cm and 3.5 cm respectively.

The weak joint is in contact with the water flow within the tunnel such that water may travel through the joint, affecting the water pressure within it. The effect of increased water pressure from mass oscillations is simulated by applying additional water pressure inside the weak joint. The pressure was increased from 0 to 1.6 MPa in steps of 0.2 MPa. The highest pressure represents the most extreme case that can arise, which is when the maximum differential pressure of ~ 160 m is able to travel through the joint. The shear and normal displacement along the joint, as well as the total displacement of the tunnel wall, for the different water pressures are illustrated in Figure 10.12.

The simulation result from where 1.6 MPa water pressure is added within the weak joint is shown in Figure 10.13. The yielding of the joint is more than 2 m and the shear displacement is more than 70 cm. The total displacement at the tunnel wall is 1.27 m. In the upper wall have rock elements yielded by tension formed a triangular wedge. The white dotted line illustrates where the developing cracks may form a continuous joint that intersects the existing joint.

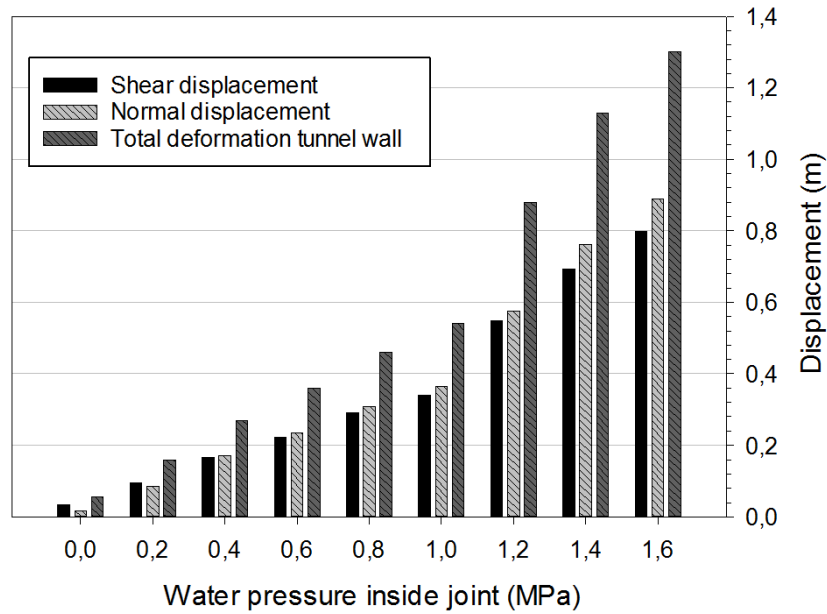


Figure 10.12: Displacement along weak joint

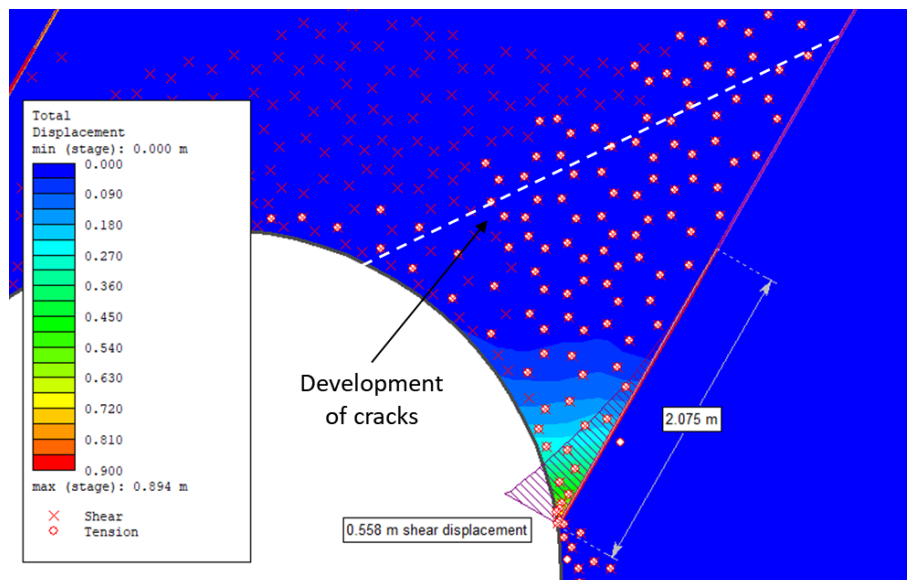


Figure 10.13: Simulation with 1.6 MPa water pressure inside weak joint

10.6 3D modelling of swelling pressure in weakness zone

Mao (2012) performed numerical analysis of weakness zones containing swelling clays, comparing results from modelling in two dimensions (Phase²) and 3D (FLAC^{3D}). It was concluded that 3D models are able to consider complicated geometries for tunneling in weakness zones, while to get realistic results from a 2D analysis, the weakness zone had to be perpendicular to the tunnel axis and much wider than the tunnel diameter. In this case the zone in question is narrow (only 1 m wide) and oriented oblique to the tunnel axis. It is therefore decided to carry out the swelling analysis in a three-dimensional program, more precisely in RS³ version 2.0.

10.6.1 Model set up and geometry

The model geometry is presented in Figure 10.14. The weakness zone is represented by a geological layer of 1.5 meter thickness, intersecting the tunnel at an angle of 40 degrees and with a dip of 75°. The surrounding rock mass is assigned the properties of phyllite. The external box is sufficiently extended in both vertical and horizontal directions, and restricted in X, Y and Z directions.

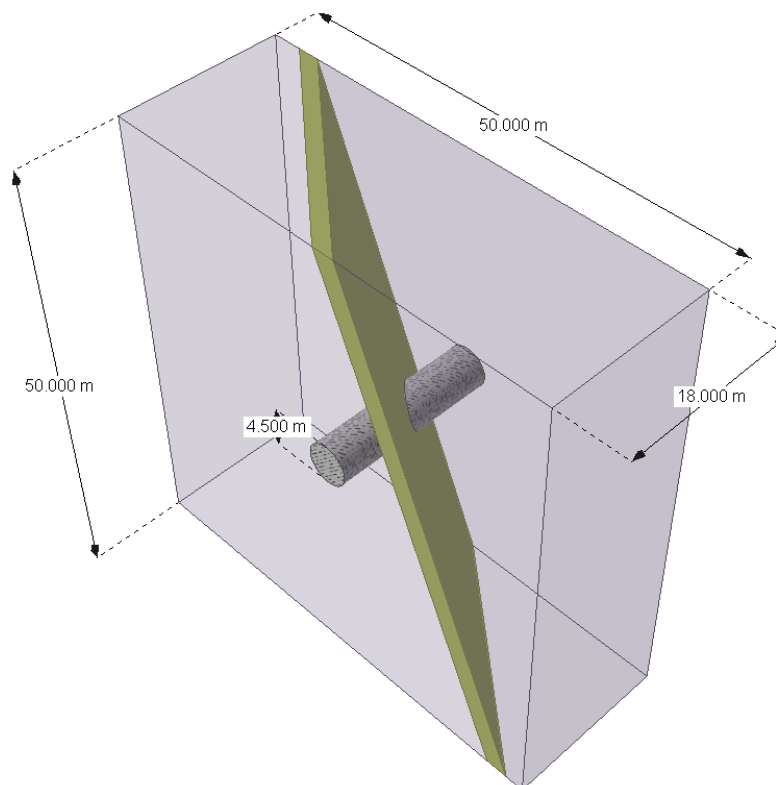


Figure 10.14: Geometry of 3D model of weakness zone. The zone (green layer) is intersecting the tunnel in the centre of the model. Downstream direction is to the upper right in the figure.

10.6.2 Input parameters

Stress conditions

Stresses at the tunnel location are calculated according to Equation (9.5) and the chosen stress ratios. To check if the principal stresses are affected by topography, an elastic stress analysis was run in RS², with cross sections along the two directions of the horizontal stresses. The analysis confirmed that the stresses are not significantly affected, and that the horizontal and vertical stresses can be regarded as the principal stresses at the tunnel location. The calculated stress magnitudes are given in Table 10.15.

Table 10.15: *Calculated stresses at chainage 1200*

Parameter	Description	Value	Unit
z	Tunnel depth	155	m
γ_0	Average overburden unit weight	0.03	MN/m ³
σ_v	Vertical stress	4.7	MPa
k	Stress ratio	2.8 / 1.07	
σ_H	Major horizontal stress	13.0	MPa
σ_h	Minor horizontal stress	5.0	MPa

Rock mass properties

It is assumed that the surrounding phyllite is of moderate quality, assigning it intermediate values from the given ranges in Table 9.2. The applied failure criterion is Mohr-Coulomb, and required parameters are calculated through RocData. The rock mass of the area has been subjected to folding and shearing. Close to a fault, which is the case here, the rock is likely to be very schistose. The estimation of rock mass modulus is therefore based on the formula proposed by Panthi (2006), as it is well suited for highly anisotropic rocks with low compressive strength.

The weakness zone consists of highly jointed and weathered rock mass. It is considered as a homogeneous material and the general Hoek-Brown failure criteria is applicable. Assuming weathering grade IV (ref. Table 3.5), both strength and deformation modulus is estimated to be reduced by 80 % compared to the parameters for the surrounding rock mass (ref. Figure 3.6). The material can therefore be considered to already be in residual state in the model, and the input values for peak and residual strength will be equal.

The strength reduction in the weakness zone is believed to have developed and aggravated over the years during operation of the plant. The material closest to the tunnel periphery would have experienced most water flow and fluctuations, and there would most likely be a variation in strength within the weakness zone. In the model a conservative simplification

is chosen, and the parameters for the weakest material is assigned to the whole weakness zone. Input parameters for the phyllite and the weakness zones are given in Tables 10.16 and 10.17.

Table 10.16: Input parameters for phyllite near weakness zone

Parameter	Description	Peak value	Residual value	Unit
σ_{ci}	Intact rock strength	70	–	MPa
GSI	Geological strength index	60	30	–
m_i	Material constant	7	–	–
E_{ci}	Intact def. modulus	35	–	GPa
ν	Poisson's ratio	0.15	–	–
T_0	Tensile strength	0.2	0	MPa
ϕ	Friction angle	43.8	37.6	deg
c	Cohesion	1.01	0.58	MPa
E_m	Rock mass modulus	4880	–	MPa
	Dilation angle	–	20	deg

Table 10.17: Input parameters for weathered material in weakness zone. Values are applied for both peak and residual input.

Parameter	Description	Value	Unit
σ_{ci}	Intact rock strength	14	MPa
GSI	Geological strength index	15	–
m_i	Material constant	4	–
E_{ci}	Intact def. modulus	7	GPa
ν	Poisson's ratio	0.15	–
m_b	Reduced material constant	0.192	–
s	Constant	0.00007	–
a	Constant	0.561	–
E_m	Rock mass modulus	436	MPa

Rock support

The installed support at the weakness zone consists of a thin layer of standard shotcrete, probably about 10 cm thick or less (discussion with supervisor Dr. Krishna Panthi, 24.05.18). Shotcrete is implemented in the numerical model as a liner layer at the inner tunnel surface. The layer is applied in the length of the weakness zone. Approximate strength values for the shotcrete is based on typical shotcrete parameters given in Mahar et al. (1975). The residual values are set to 0, so that the load magnitude leading to failure of the rock support will be easy to detect. The thickness of the installed shotcrete layer is important for the maximum support pressure. The model is therefore run with two different thicknesses of the support layer: 5 cm and 10 cm.

Table 10.18: Input parameters for shotcrete

Strength parameter	Peak value	Residual value	Unit
Young's modulus	25	–	GPa
Poisson's ratio	0.2	–	–
Shear strength	5	0	MPa
Compressive strength	35	0	MPa
Tensile strength	5	0	MPa
Thickness	0.05/0.1		m

Porewater pressure

The rock material is assumed to be highly weathered and disintegrated. The permeability of the weathered material should therefore be significantly higher than for the surrounding rock mass. As pressure fluctuations arise in the headrace tunnel due to mass oscillations, it is hence assumed that the pressure can travel inside the weakness zone in the same way as described for joints in Chapter 9. As discussed, the maximum pressure difference could be as high as 1.6 MPa. To simulate the pore water pressure acting on the tunnel, a uniformly distributed load is applied at along the circumference where the weakness zone intersects the tunnel, as illustrated in Figure 10.15.

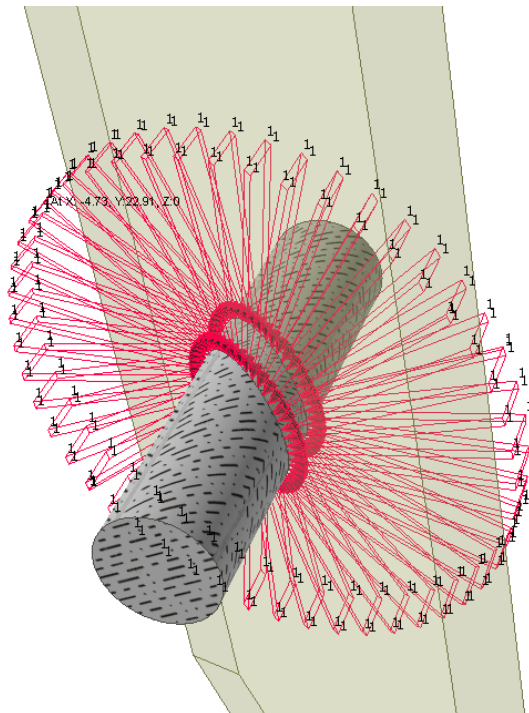


Figure 10.15: Application of load onto the tunnel circumference. Looking downstream.

Swelling pressure

Water flow through the weakness zone implies that any present swelling minerals have access to water, and swelling pressure may develop. Similarly to the pore water pressure, the swelling pressure will act onto the rock support where the weakness zone intersects the tunnel. In addition, the swelling pressure will act onto the rock mass adjacent to the weakness zone. This load will however be directed parallel to the tunnel alignment and not directly influence the loading of the support. It will therefore not be implemented in the model.

Since swelling pressures previously experienced in Norwegian tunnels have been between 0.1 and 1 MPa, the load from the swelling pressure at Brattset is assumed to be within the same range. The pressure from swelling will act normally on the tunnel in the same area as the pore water pressure, increasing the total load onto the rock support. Since the two factors of pressure act together, the total load will be decisive for the support behaviour. Thus, the load applied in the numerical simulation is the total contribution from both pore water pressure and swelling pressure.

10.6.3 Results

The numerical model was run with two different liner thicknesses. In each of the analysis the radial load was increased in steps of 0.1 MPa, from 0 and beyond failure of the shotcrete. The obtained maximum deformation in the tunnel is plotted for each load in Figure 10.16. For the model with shotcrete layer of 10 cm, tunnel collapse occurred at loads above 1.6 MPa. For the 5 cm thick layer, tunnel collapse occurred at loads above 0.8 MPa.

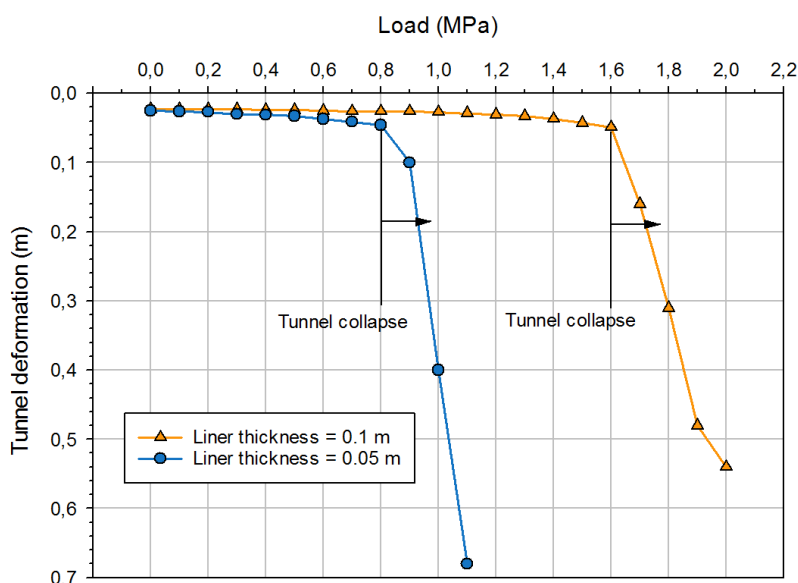
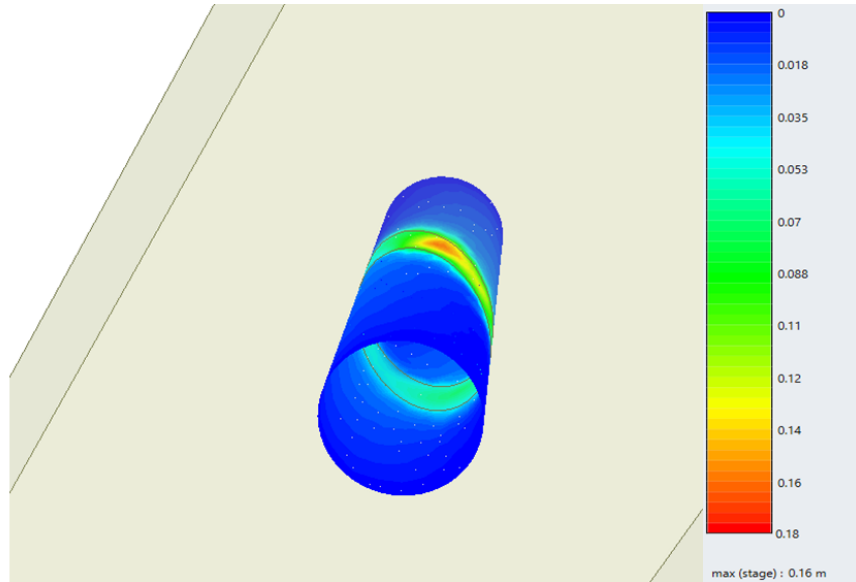
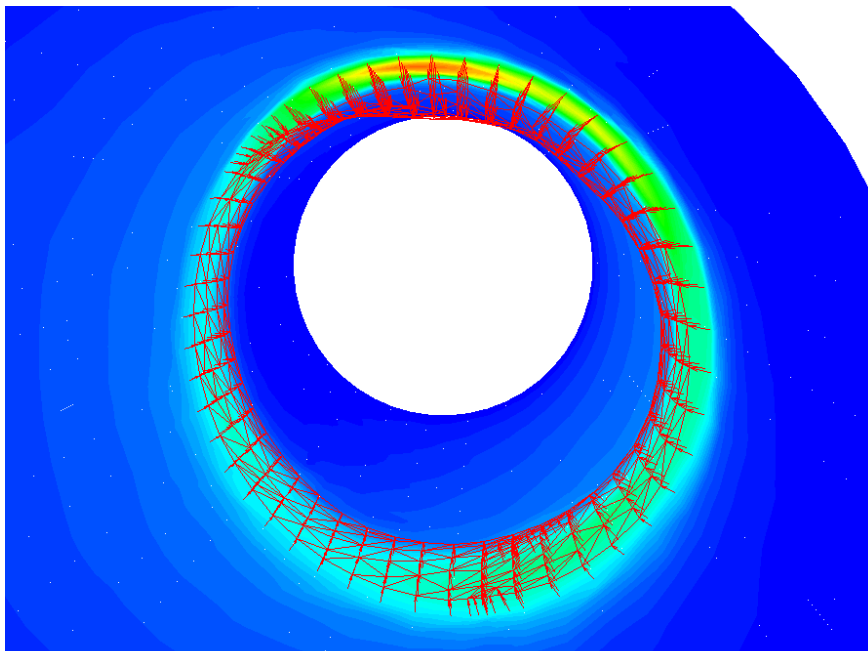


Figure 10.16: Result from weakness zone analysis. The plot shows the applied radial load onto the shotcrete liner, and the corresponding maximum deformation of the tunnel.

The result from a simulation is illustrated in Figure 10.17. Here the liner thickness is 10 cm and the applied load is 1.7 MPa. The support has failed, and the tunnel collapsed. The largest deformation appears in the tunnel crown and upper right wall of the tunnel when looking upstream. This result agrees well with the sketch of the failure, where the failure scar is indicated in the very same location.



(a) Tunnel deformation



(b) Deformation vectors inside the tunnel. Scale factor = 3.

Figure 10.17: Tunnel deformation due to radial load of 1.7 MPa. Looking upstream.

Chapter 11

Discussions

11.1 Design principle and hydraulic transients

One of the main criteria in the Norwegian design principles for unlined shafts and tunnels is the criterion of sufficient confinement. Over the years different "rule of thumb" formulas and finite element methods have been suggested and applied in the design of hydropower schemes in Norway. The purpose of these criteria has been to provide simple methods to fulfill the confinement criterion during the design stage. The principle is simple: to prevent jacking of the rock mass, the water pressure inside the tunnel should never exceed the minor in-situ stress (σ_3).

It is interpreted that the *maximum static water head* H used by the various authors (Broch, 1984; Selmer-Olsen, 1969; Bjørlykke and Selmer-Olsen, 1972) to express the design principle, is defined as the maximum water head during continuous production, i.e. the highest regulated gross head. The rise in hydraulic pressure from transients is rarely mentioned in the studied literature regarding design principles. The exception is Helwig (1987), who evaluates the impact of water hammer on the rock mass. The conclusion is that the pressure surges from water hammer are too fast for increasing the risk of hydraulic jacking of the rock mass.

The amplitude of water hammer is dependent on the distance between the turbine and the next free water surface in the system. In the first Norwegian hydropower projects a surge shaft was installed to reduce the water hammer. The innovative design of the air cushion chamber did not only give flexibility to the project layout, but the water hammer would also become comparatively less, as the chamber could be located closer to the turbine. On the other hand, the surge shaft and air cushion chamber give rise to mass oscillations, which amplitude is dependent on the distance between the shaft or chamber and the water reservoir. Thus, for the mass oscillations, the pressure amplitude would be larger for an air cushion chamber design.

The maximum amplitudes of water hammer and mass oscillations at full closure of the regulation valves have been estimated in this thesis. The calculated upsurge of mass oscillation is 83.5 m, nearly four times larger than for the water hammer. The relatively large upsurge pressure can be explained by the long headrace tunnel between the air cushion chamber and the reservoir ($> 16\,000$ m), with a relatively small cross-sectional area ($\sim 16\text{ m}^2$). It would therefore be of interest to consider the maximum total head at Brattset, including the additional pressure from mass oscillations, in connection to the design principle.

Since stress measurements have been conducted at the air cushion chamber, the principle can be checked here. The estimated static head at this location is 242.5 m. Inserting in Equation (2.4), it is found that $(H + \Delta z) \cdot \gamma_w = (242.5\text{ m} + 83.5\text{ m}) \cdot 9.81\text{ kN/m}^3 = 3.2\text{ MPa}$. This is less than $\sigma_3 = 5.1\text{ MPa}$, and the criterion of sufficient confinement should be fulfilled in the headrace tunnel at Brattset, also when the upsurge pressure from hydraulic transients are considered.

11.2 Discussion on stability assessments

The four modes of instability issues identified during the Project work are in this study modelled and analyzed. Since the observed failures have already taken place, this can be considered as back analyzes. The goal of the assessments has been to evaluate the influence of geological conditions, stresses and the water pressure within the water system on the stability of the headrace tunnel.

11.2.1 Input parameters

It is difficult to precisely determine in-situ stresses, and properties of rock mass and discontinuities. Input parameters for the stability analyzes are generally based on estimates and empirical relations, and the quality of the results are limited to the quality of the defined input parameters.

In this study a point load test has been conducted on one phyllite sample from the project area. However, the quality of the phyllite in the area varies to a great extent, and the test results may not be representative for the phyllite in the whole area. It should also be noted that converting the point load strength of highly anisotropic rocks to compressive strength could give inaccurate values. In the determination of rock mass parameters of the phyllite, it is therefore chosen to present a range of values. And from that, the most likely values for the relevant instability issue are estimated.

Joint parameters are based on observations from field work. As these are surface observations, they may not be representative for the joint conditions at tunnel depth. Since the

analyzed situations are caused by unfavourable conditions, either in rock mass quality or due to jointing and joint conditions, it is then chosen the most unfavourable value for use in the stability analysis.

11.2.2 Potential to spalling

The magnitude and orientation of the in-situ stresses, together with the rock mass strength, are the dominating factors in strainburst problems. Whether it is rock buckling or spalling that occur is generally dependent on the properties of the rock mass. A very schistose and weak phyllite will likely cause buckling, while a harder and less schistose phyllite will most likely fail by spalling. In this study, stress conditions and rock mass strength have been estimated to perform assessments of the susceptibility to stress related instabilities in the head-race tunnel at Brattset. The assessment of spalling potential is done by empirical and semi-analytical methods, and compared to results from numerical modelling. Although both empirical and numerical methods are subjected to a great deal of uncertainties, the different spalling analyzes give similar results.

The spalling classification by the Q-system is a qualitative approach, based on empirical studies. For what is assumed to be an unsaturated phyllite, the method suggests that spalling or buckling may occur if unfavourable jointing or weakness planes are present. This correlates well to the actual observations during construction of the tunnel, when buckling of the phyllite was observed in the tunnel wall and abutment. For a saturated phyllite, with lower strength, the result suggests that moderate spalling will take place.

Depth impact of spalling

The approach of maximal tangential stress and spalling strength to estimate the impact depth of fracturing is a semi-analytical method, based on both empirical case studies and relations for stress and strength values. The method gives a quantitative assessment, providing an estimate of the extent of damage caused by induced stress around the tunnel contour. The knowledge of depth impact is valuable information when developing a strategy for rock support, and is particularly useful for determining length and type of rock anchors, and other support measures such as mesh, rock straps and steel fiber reinforcement (Panthi, 2017).

From the analysis results it is evident that a 30 % reduction of the phyllite strength significantly increases the depth impact, from 1.6 m for the strong rock to 3.6 m for the weakened rock. The estimated depth impact of the weaker phyllite agrees well with the result from the 2D numerical modelling, where the affected area around the tunnel became 3.63 m. As seen in Figure 10.7, the affected zone around the tunnel is quite extensive, and a plastic zone has developed in the area where the rock mass has yielded.

Effect of schistosity

Since the highest induced stresses are located in the tunnel crown and floor, the spalling problems will develop here. However, the orientation of stresses relative to joint sets and structural features, such as bedding and schistosity, will have major influence on stress related instabilities. According to (Nilsen and Thidemann, 1993), this is particularly important if the schistosity runs parallel to the tunnel axis, and the major principal stress acts perpendicular to the tunnel axis and along the dip direction of the schistosity plane.

The spalling behaviour has also been analyzed with a 2D numerical model. Two different models from the evaluated tunnel location were compared: a continuum model with no joints, and a discontinuum model where foliation joints were inserted. The results from the simulation show that the tunnel deformation is relocated when schistosity is present, and that the total displacement is increased. The relocated deformation appears in the upper and lower wall, developing parallel to the schistosity plane, similar to how Blindheim (1982) described the buckling behaviour that was observed during construction.

11.2.3 Wedge fall

In the limit equilibrium analysis of the wedge fall, the stress situation and the water pressure inside the joints were considered to be constant, such that the stability of the wedge is depending entirely on the friction along the joints. The Barton-Bandis joint model was applied to estimate the shear strength of the joint, with input based on the joint roughness, rock wall strength and joint alteration. The obtained FS from a calculation with input values for a strong, unweathered joint were used as a reference in the further analysis.

Weakening of joints is assumed to appear in two ways: either 1) by weathering of the rock wall contact, reducing the wall strength, or 2) by alteration or wetting of the joint surface or filling, reducing the frictional resistance. To simulate joint weakening, the corresponding parameters in the Barton-Bandis model, JCS, JRC and ϕ_r were modified. The results show that a reduction of JCS and JRC does not significantly affect the frictional resistance along the joint. On the contrary, the change in ϕ_r has a substantial effect on the factor of safety, reducing it by almost 70 % over the range from a unaltered joint ($\phi_r = 35^\circ$) to a highly altered joint with low friction mineral coating ($\phi_r = 8 - 16^\circ$).

The tangential stress calculated for the analysis is of such magnitude that this is the main component that governs the driving force. It is also the most contributing component for the normal stress on the joint. Hence, the weight of the wedge and the water pressure acting in the joints are not significantly influencing the stability. As noted in Chapter 4, the failure of one block or wedge (key block) will decrease the interlocking and restraining effect of the stress. The progressing failure would then increasingly depend on the block weight and

water pressure in relation to the resisting shear strength of the joints. In this case would especially the water pressure due to mass oscillations contribute to reduced stability.

A second factor that could influence the interlocking stresses is plastic deformation, i.e. failure of rock mass. The quartz keratophyre is a strong rock, which has the ability to transfer high stresses, while the surrounding phyllite is weaker and more anisotropic. As the spalling potential assessments indicate, the tangential stresses may cause fracturing close to the contour, resulting in a plastic zone with reduced capacity to transfer stresses. As the intrusions of quartz keratophyre are relatively narrow, ranging from 0.1 m to 5 m, it is likely that plastic deformation in the surrounding phyllite may also influence the stress situation within these zones, reducing the interlocking effect.

11.2.4 Induced fracturing intersecting joint

Some of the most serious failures that have been reported from the tunnel inspections are assumed to be a result of both stress related mechanisms and shear failure of discontinuities. In the numerical model, the displacement along one joint intersecting the tunnel circumference is evaluated. It is assumed that the water flowing inside the tunnel may travel inside this joint, changing its properties as well as increasing the pore water pressure along the joint.

From the analysis it is confirmed that stress induced fracturing may develop in the intact rock around the tunnel periphery, and that the joint intersecting the tunnel will act as a sliding plane. Elements yielded by tension indicate that tensile fractures are induced around the tunnel crown and towards the modelled joint. As the fractures develop, they may coincide and form a continuous joint that intersects the pre-existing joint in the rock mass. It is evident that just a small increase in water pressure have a significant effect on the shear strength of the joint and the displacement that occur. From Figure 10.12 it can be seen that both the normal and shear displacements are linearly increasing to the amount of water pressure within the joint. It should be noted that an acceleration of the displacement occurs between 1.2 and 1.4 MPa of water pressure. This may indicate that the pressure at this point becomes so large that the adjacent joint walls loose contact, dramatically reducing the friction along the joint.

A reoccurring feature in the reported events of large block falls, is the presence of a clay-filled seam. The seams follow the foliation plane in the phyllite, moderately to steeply dipping into the tunnel, and are varying in size and extent. One of these failures is described by Skoglund (2008) as "*a large clay-filled seam. 10-15 m deep, 0.5 m thick at the inner end and 1 m thick at the tunnel contour. Fallen material is covering the tunnel floor in a 20 m long section*". In the wedge analysis it was found that the frictional conditions at the discontinuities and

the assigned value for the residual friction angle, are of great importance to the stability. This is also of relevance in this situation. The filling or gouge materials within the seams will significantly decrease the frictional resistance, as the residual friction angle (ϕ_r) would become correspondingly small, and increase the risk of failure.

11.2.5 Collapse of weakness zone

A back analysis of the collapse that occurred in a weakness zone at Brattset in 2008 has been conducted in this study. The weakness zone was most likely a fault containing swelling gouge material. Since the zone is narrow and orientated at an oblique angle to the tunnel alignment it was chosen to use 3D modeling for the analysis. Rock support in form of shotcrete was installed in the model and radial load was applied to simulate the pressure from the weakness zone.

There are identified two factors that contribute to the load acting on the tunnel circumference: 1) swelling pressure due to activation of swelling minerals, and 2) pore water rise due to mass oscillations. Investigations of swelling potential of gouges in Norwegian tunnels showed that the swelling pressures normally range between 0.1 and 1 MPa. However, the swelling pressure is to a large extent dependent on the physical conditions, such as water access and stress relieve. The pore water pressure is assumed to arise from the pressure surges due to mass oscillations, where the estimated maximum pressure difference corresponds to 1.6 MPa. It is at this point difficult to predict the contribution from each of these two factors to the total load on the support, and the analysis result will only suggest the magnitude of accumulated pressure that could lead to collapse.

Since the thickness of the installed shotcrete at Brattset is uncertain, the numerical model was run with two different thicknesses of the support liner. For a 5 cm thick support liner, the model collapsed on a pressure between 0.8 and 0.9 MPa, while for a 10 cm thick liner, collapse occurred at a pressure between 1.6 and 1.7 MPa. These loads leading to failure can be compared to the approximate estimates for maximum capacities for different support measures from Hoek (2007). The suggested maximum support pressure $p_{i\max}$ for a concrete or shotcrete lining of 5 cm and 10 cm thickness, respectively, are given in Table 11.1. It can be seen from the estimated values that the maximum support pressures agree well with the results from the numerical analysis.

The most critical factor to the issue seems to be the opportunity for water to flow freely within the weathered material, such that swelling minerals are hydrated. Water flow inside the weakness zone would also allow pore water pressure to build up behind the shotcrete liner. In this analysis the pore water pressure and swelling pressure act together, such that the total pressure is the crucial load leading to failure. It is therefore difficult to estimate the

Table 11.1: Maximum support pressure (Hoek, 2007). Tunnel diameter $D = 4.5$ m

Thickness (mm)	UCS (MPa)	Support pressure for a tunnel of diameter D	$p_{i\ max}$ (MPa)
100	35	$p_{i\ max} = 7.3 D^{-0.98}$	1.67
50	35	$p_{i\ max} = 3.8 D^{-0.99}$	0.86

amount of swelling pressure from the numerical analysis. With the magnitudes of the mass oscillation amplitudes that have been estimated in this study, the water pressure could possibly exceed the swelling pressure and be the largest contributing component to failure. In that case the permeability of the weathered material within the zone would be of importance, such that water is able to flow during the period of the mass oscillations.

11.3 Long-term instability issues

As concluded by Helwig (1987), the period of water hammer is probably too short for affecting the rock mass and its discontinuities considerably. Depending on the length between the reservoir and the surge shaft or air cushion chamber, the period of the following mass oscillation is significantly longer. At Brattset the period is almost 5 minutes, meaning that one cycle of pressure rise and drop of mass oscillations is more than 200 times longer than for the water hammer wave.

There exists very little research on the response in water pressure within discontinuities during mass oscillations. In this study it is suggested that open joints or joints with permeable filling materials may be more affected by pressure fluctuations. If water can flow inside these joints, the normal force along the discontinuity plane will be reduced, decreasing the shear strength. The frictional resistance could also be reduced by the wetting of filling or gouge material. In addition, fluctuating water pressures could cause washing of fill materials or breaking of rock bridges, leaving open discontinuities and increasing their persistence. Wetting and washing of gouge material would be especially crucial for clay filled seams, which there are observed many of along the headrace tunnel at Brattset (see Figure 11.1).

The stability of weakness zones is highly influenced by the supply of water into the zone from the waterway. If swelling minerals are present in the zone, the access to water will be an important factor to the swelling pressure that can develop. Additionally, the flow of water through the weak rock material could cause saturation and weakening of cohesion and frictional properties over time. The latter is possibly what led to the shaft collapse at Svandalsflona in 2008.

Although a weakness zone is supported by a concrete lining or shotcrete, it may still be pos-



Figure 11.1: Washed-out seam detected during tunnel inspection in 2015. The seam is following the schistosity plane, dipping into the tunnel (Landløpet, 2015).

sible for water to travel into the zone. Water can potentially migrate through shotcrete, as it can be to some extent permeable, but most importantly can water flow from unlined sections and through open, intercommunicating joints that intersect the zone. This is a likely explanation to the situation that led to the tunnel collapse at Brattset in 2008. Water supply to the zone of highly weathered material, probably caused weakening of the material and hydration of swelling minerals over time. The total pressure on the shotcrete lining, from both swelling and the pressure difference due to mass oscillations, may eventually lead to failure of the support and collapse of the extremely weak rock material.

The criterion of sufficient confinement has already been discussed, and is a design principle that in general is fulfilled, also when the pressure rise from hydraulic transients is considered. The second main criterion in the Norwegian unlined design principles, is the criterion of required geological conditions. This means that the rock mass should be well suited for direct contact with the water flowing through the unlined tunnel or shaft. Nilsen and Thidemann (1993) emphasize different geological conditions that should be avoided when planning the tunnel or shaft. Among these, it is recommended to avoid heavily jointed rock mass with open and intercommunicating joints. An increasing number of start-and stop cycles may cause more erosion and wash-out of discontinuities and breaking of rock bridges, such that the rock mass gets more open and intercommunicating joints.

Weakness zones and faults of unfavourable orientation is also recommended to avoid. It

is not always easy to detect weakness zones before excavation of the tunnels and normally, when weakness zones and faults encountered during construction, they are stabilized by rock support. However, in the long-term it may look like some weakness zones may be insufficiently supported. This may particularly concern narrow zones and faults, such as the ones at Brattset and Svandalsflona, that during construction of the tunnel were regarded to be less critical.

Chapter 12

Conclusions and recommendations

12.1 Conclusions

The results from the stability assessments show that several factors influence the stability. This involve stress conditions, rock mass strength and deformability, joint properties and water pressure. After the change in the production pattern in the hydropower plant of Brattset, from supply to demand driven, the amount of stability problems in the tunnel system has increased.

Stability assessments have been carried out on the observed instability issues at Brattset, and the involvement of hydraulic transients due to a fluctuating operation regime have been evaluated. Fore modes of failures were analyzed:

1. Stress induced spalling and buckling
2. Block fall caused by intersecting discontinuities
3. Block fall caused by joints and stress induced fracturing
4. Collapse in weakness zone

The spalling and buckling behaviours were observed during construction, while the three other instability issues have developed and raised in numbers over time. Since the stress situation and the geological conditions are generally constant, it is reason to believe that the increased number of instabilities may be a consequence of the higher frequency of start-and-stop sequences in the power production.

It is found that due to its long period, the mass oscillation that arise from fluctuation production will have the potential to affect the stability. The effects are mainly concentrated to discontinuities and may be summarized as follows:

- Erosion and washing of filling material
- Breaking of rock bridges

- Reduced normal force on discontinuity plane
- Wetting of filling material, reducing friction
- Increased mobilization of swelling material
- Saturation and weakening of rock mass
- Increased pressure on rock support

These are effects that aggravate slowly and will influence the long-term stability. It is not only the maximum amplitudes of the mass oscillations, which have been estimated in this study, that will determine the degree of impact during each start or stop of the turbines. The time it takes, or number of cycles, before the mass oscillations are dampened out would also be of importance here.

12.2 Recommendations

It is evident that the degree of jointing of the rock mass is an important factor in relation to the proposed effects. The water pressure fluctuations due to mass oscillations would therefore be most critical for hydropower schemes situated in jointed rock mass. It is at this point not done enough research on the effect of mass oscillations on discontinuities. In order to get closer to an understanding of how higher frequencies of start-and-stop sequences may affect the long-term stability of unlined tunnels, further studies are required.

According to Dr. Krishna Panthi (discussion with supervisor, 08.06.18), NTNU has recently established a monitoring system that can be used for continuous monitoring of the pore water pressure within the rock mass . The system is in testing at Roskrepp HPP (Sira-Kvina power company), and will be monitoring the pressure response within discontinuities during fluctuating operation of the power plant. The project will hopefully give valuable information to the matter, however, there will be need for more data in the future. In the further research on the topic, it should therefore be pursued to install continuous monitoring in waterway systems at other hydropower plants as well.

Bibliography

Printed Sources

- Aydan, Ö., Ulusay, R. and Kawamoto, T. (1997) Assessment of rock mass strength for underground excavations. *International Journal of Rock Mechanics and Mining Sciences* 34(3), pp. 18.1–18.17.
- Barton, N. (2002) Some new Q-value correlations to assist in site characterisation and tunnel design. *International Journal of Rock Mechanics and Mining Sciences* 39(2), pp. 185–216.
- Barton, N., Lien, R. and Lunde, J. (1974) Engineering classification of rock masses for the design of tunnel support. *Rock Mechanics and Rock Engineering* 6(4), pp. 189–236.
- Barton, N. and Bandis, S. (1990) Review of predictive capabilities of JRC-JCS model in engineering practice. *Proc. International Symposium on Rock Joints, Loen, 4-6. June*. Rotterdam: A. A. Balkema, pp. 603–610.
- Barton, N. (1972) A model study of rock-joint deformation. *International Journal of Rock Mechanics and Mining Sciences & Geomechanics Abstracts* 9(5), pp. 579–582.
- Bieniawski, Z. (1978) Determining rock mass deformability: experience from case histories. *International Journal of Rock Mechanics and Mining Sciences & Geomechanics Abstracts* 15(5), pp. 237–247.
- Bieniawski, Z. (1993) Classification of rock masses for engineering: The RMR-system and future trends. *Comprehensive rock engineering*. Ed. by J. A. Hudson. Vol. 3, pp. 553–573.
- Bjørlykke, S. and Selmer-Olsen, R. (1972) *Nødvendig overdekning i dalsider ved fjellrom med høyt innvendig vann- eller lufttrykk*. Report. Trondheim: Department of Geology, Technical University of Norway.
- Blindheim, O. T. (1982) Fullprofilboring i anlegg med bergtrykksproblemer (eng: Examples of rock pressure problems during tunnel and shaft boring). *Fjellsprengningskonferansen - Bergmekanikkdagen - Geoteknikkdagen 1982*. Ed. by A. M. Heltzen et al. Norsk Jord- og Fjellteknisk Forbund. Oslo: Tapir, 25.A.1–19.

- Bråtveit, K., Bruland, A. and Brevik, O. (2016) Rock falls in selected Norwegian hydropower tunnels subjected to hydropeaking. *Tunnelling and Underground Space Technology* 52, pp. 202–207.
- Broch, E. (1979) Changes in rock strength caused by water. *Proceedings of the 4th Congress of the International Society for Rock Mechanics, Montreux* (4), pp. 71–75.
- Broch, E. (1984) Development of Unlined Pressure Shafts And Tunnels in Norway. *Hydropower tunnelling, Publication No. 3*. Norwegian Soil and Rock Engineering Association.
- Broch, E. (2000) Unlined high pressure tunnels and air cushion surge chambers. *AITAS-ITA 2000 World Tunnel Congress*. Ed. by R. G. Stimson and J. L. Stimson. World Tunnel Congress. Johannesburg: South African Institute of Mining and Metallurgy, pp. 63–72.
- Broch, E. (2017) Tunnels and underground works for hydropower projects. Lecture held in TGB4212 - Rock Mechanics, Advanced Course, NTNU, 30. Oct. 2017.
- Broch, E. and Lysne, D. K., eds. (1992) *Hydropower'92. Proceedings of the 2nd International Conference on Hydropower*. Rotterdam: A. A. Balkema.
- Broch, E. (2006) Why did the hydropower industry go underground? *Sustainable underground concepts, Publication No. 15*. Ed. by J. K. Rohde et al. Oslo: Norwegian Tunnelling Society.
- Broch, E. (2013) Underground hydropower projects – Lessons learned in home country and from projects abroad. *Norwegian Hydropower Tunnelling II, Publication No. 22*. Ed. by E. Broch, E. Grاسبakken and W. Stefanussen. Oslo: Norwegian Tunnelling Society.
- Brown, E. T. (2008) Estimating the mechanical properties of rock masses. *Proceedings of the 1st Southern Hemisphere International Rock Mechanics Symposium*. Ed. by Y. Potvin et al. Perth: Australian Centre for Geomechanics, pp. 3–22.
- Buen, B. and Palmstrøm, A. (1985) Design and Supervision of Unlined Hydro Power Shafts and Tunnels with Head up to 590 Meters. *Hydropower tunnelling, Publication No. 3*. Norwegian Tunnelling Society.
- Cai, M. et al. (2007) Determination of residual strength parameters of jointed rock masses using the GSI system. *International Journal of Rock Mechanics and Mining Sciences* 44(2), pp. 247–265.
- Carranza-Torres, C. and Fairhurst, C. (2000) Application of the Convergence-Confinement method of tunnel design to rock masses that satisfy the Hoek-Brown failure criterion. *Tunnelling and Underground Space Technology incorporating Trenchless Technology Research* 15(2), pp. 187–213.
- Crowder, J. and Bawden, W. (2004) Review of Post-Peak Parameters and Behaviour of Rock Masses: Current Trends and Research, p. 14.

- Diederichs, M. (2014) When does brittle failure become violent? Spalling and rockburst characterization for deep tunneling projects. *Proceedings of the World Tunnel Congress 2014*. Foz do Iguazu, Brazil.
- Eberhardt, E. (2012) The Hoek–Brown Failure Criterion. *Rock Mechanics and Rock Engineering* 45(6), pp. 981–988.
- Elsworth, D. (1986) Wedge stability in the roof of a circular tunnel: Plane strain condition. *International Journal of Rock Mechanics and Mining Sciences and Geomechanics Abstracts* 23(2), pp. 177–181.
- Flønes, O. (1982) Fullprofilboring ved Orkla Grana-anleggene. *Fjellsprengningskonferansen - Bergmekanikkdagen - Geoteknikkdagen 1981*. Ed. by A. M. Heltzen, B. Nilsen and A. Mowinckel. Norsk Jord- og Fjellteknisk Forbund. Oslo: Tapir.
- Gee, D. G. et al. (1985) The central-southern part of the Scandinavian Caledonides. *The Caledonide Orogen - Scandinavia and related areas*. Ed. by D. G. Gee. Chichester: Wiley, pp. 109–133.
- Goodman, R. E. (1989) *Introduction to rock mechanics*. 2nd ed. New York: Wiley.
- Goodman, R. E. and Shi, G.-h. (1985) *Block Theory and Its Application to Rock Engineering*. New Jersey: Prentice-Hall, p. 338.
- Grøv, E. et al. (2011) *Developing future 20 000 MW hydro electric power in Norway*. Report. SINTEF Building and Infrastructure.
- Guttormsen, O. (2006) *TVM4165 Vannkraftverk og vassdragsteknikk – Vassdragsteknikk II*. Course compendium. Trondheim: Tapir, Kompandieforlaget.
- Hadizadeh, J. and Law, R. (1991) Water-weakening of sandstone and quartzite deformed at various stress and strain rates. *International Journal of Rock Mechanics and Mining Sciences & Geomechanics Abstracts* 28(5), pp. 431–439.
- Hansen, S. E. and Hanssen, T. H. (1988) Hydraulisk splitting (eng: Hydraulic fracturing). *Fjellsprengningskonferansen - Bergmekanikkdagen - Geoteknikkdagen 1988*. Ed. by K. R. Berg et al. Norsk Jord- og Fjellteknisk Forbund. Oslo: Tapir, pp. 26.1–26.15.
- Helwig, P. C. (1987) A theoretical investigation into the effects of water hammer pressure surges on rock stability of unlined tunnels. *Underground hydropower plants. Proceedings of the Int. Conference on Hydropower (Hydropower '87)*. Ed. by E. Broch and D. K. Lysne. Vol. 2. Trondheim: Tapir, pp. 811–818.
- Hoek, E. (2007) *Practical Rock Engineering*. RocScience. URL: <https://www.rocscience.com/documents/hoek/corner/Practical-Rock-Engineering-Full-Text.pdf>.
- Hoek, E. and Brown, E. T. (1980) *Underground excavations in rock*. London: Institution of Mining and Metallurgy.

- Hoek, E., Carranza-Torres, C. and Corkum, B. (2002) Hoek–Brown failure criterion – 2002 edition. *Mining and Tunnelling Innovation and Opportunity - Proceedings of the 5th North American Rock Mechanics Symposium and 17th Tunnelling Association of Canada Conference*. Ed. by Hammah et al. Toronto: University of Toronto, pp. 267–273.
- Hoek, E. and Diederichs, M. (2006) Empirical estimation of rock mass modulus. *International Journal of Rock Mechanics and Mining Sciences* 43(2), pp. 203–215.
- Hudson, J. A. and Harrison, J. P. (1997) *Engineering rock mechanics: an introduction to the principles*. Oxford: Elsevier Ltd.
- Hveding, V. (1992) *Hydropower development in Norway*. Vol. 1. Hydropower Development. Trondheim: Norwegian Institute of Technology, Department of Hydraulic Engineering.
- ISRM (1975a) Commission on Swelling Rock: Characterization of Swelling Rock.
- ISRM (1975b) Commission report on terminology.
- ISRM (1978a) Suggested Method for Petrographic Description of Rocks. *International Journal of Rock Mechanics and Mining Sciences & Geomechanics Abstracts* 15, pp. 43–45.
- ISRM (1978b) Suggested methods for the quantitative description of discontinuities in rock mass. *International Journal of Rock Mechanics and Mining Sciences & Geomechanics Abstracts* 15, pp. 319–368.
- ISRM (1985) Suggested method for determining point load strength. *International Journal of Rock Mechanics and Mining Sciences and Geomechanics Abstracts* 22(2), pp. 51–60.
- Jaeger, C. (1977) *Fluid transients in hydro-electric engineering practice*. Blackie, p. 413.
- Kjørholt, H., Broch, E. and Dahlø, T. S. (1992) Geotechnical design of air cushion surge chambers. *Hydropower'92. Proceedings of the 2nd International Conference on Hydropower*. Ed. by E. Broch and D. K. Lysne. Rotterdam: A. A. Balkema, pp. 189–192.
- Kristiansen, J. and Stokkebø, O. (1992) The 'Collect-and-Transfer' system in hydropower developments - A cost effective and environment saving solution. *Hydropower'92. Proceedings of the 2nd International Conference on Hydropower*. Ed. by E. Broch and D. K. Lysne. Rotterdam: A. A. Balkema, pp. 189–192.
- Kvaal, S. and Wale, A. (2000) *En spenningshistorie: Trondheim Energiverk gjennom et århundre*. Trondheim: Trondheim Energiverk.
- Landløpet, T. H. (2015) Notat til AO24625.
- Li, C. C. (2015a) *Applied Rock Mechanics*. Norwegian University of Science and Technology.
- Li, C. C. (2015b) Mechanical properties of rocks tested in the rock mechanics laboratory NTH/NTNU/SINTEF. Appendix 1 in *Applied Rock Mechanics*.

- Mahar, J. W., Parker, H. W. and Wuellner, W. W. (1975) *Shotcrete Practice in Underground Construction*. Tech. rep. Urbana, Illinois: Illinois Univ. at Urbana-Champaign. Dept. of Civil Engineering, p. 516.
- Mao, D. (2012) Analysis of Rock Support Performance for Tunnelling in Weakness Zones Containing Swelling Clay. PhD thesis. Trondheim: NTNU.
- Mao, D., Nilsen, B. and Lu, M. (2011) Analysis of loading effects on reinforced shotcrete ribs caused by weakness zone containing swelling clay. *Tunnelling and Underground Space Technology* 26(3), pp. 472–480.
- Martin, C. and Christiansson, R. (2009) Estimating the potential for spalling around a deep nuclear waste repository in crystalline rock. *International Journal of Rock Mechanics and Mining Sciences* 46(2), pp. 219–228.
- Midtlyng, A. (2015) Tunnelbefaring Brattset 27.08.2015, fra Næverdalen til Skamfer.
- Mitchell, J. K. and Soga, K. (2005) Soil mineralogy. *Fundamentals of Soil Behaviour*. 3rd ed. New Jersey: Wiley. Chap. 3, pp. 35–82.
- Munoz-Hernandez, G. A., Mansoor, S. and Jones, D. (2013) Hydraulic Models. *Modelling and Controlling Hydropower Plants, Advances in Industrial Control*. London: Springer-Verlag. Chap. 4, pp. 43–75.
- Myrvang, A. M. (2001) *Bergmekanikk (Rock mechanics)*. Trondheim: Department of Geology, Mineral Resources Engineering, Norwegian University of Science and Technology.
- Neupane, B. (2017) *Numerical Modelling of instability in Headrace tunnel of Brattset Hydropower Plant, Norway*. Project report: GB 8306 Numerical Modelling for Rock Mechanics. Unpublished. NTNU, Department of Geoscience and Petroleum.
- NGI (2015) *Using the Q-system: Rock mass classification and support design*. Handbook. Oslo.
- Nilsen, B. (1999) Alternative approaches for stability analysis. *Fjellsprengningskonferansen - Bergmekanikkdagen - Geoteknikkdagen 1999*. Ed. by T. Alten et al. Norsk Jord- og Fjellteknisk Forbund. Oslo, pp. 33.1–33.15.
- Nilsen, B. and Broch, E. (2012) *Ingeniørgeologi - Berg, grunnkurskompendium*. Trondheim: Department of Geology, Mineral Resources Engineering, Norwegian University of Science and Technology.
- Nilsen, B. and Palmström, A. (2000) *Engineering Geology and Rock Engineering; Handbook No. 2*. Oslo: Norwegian Group of Rock Mechanics (NBG).
- Nilsen, B. and Thidemann, A. (1993) *Rock Engineering*. Vol. 9. Hydropower Development. Trondheim: Norwegian Institute of Technology, Department of Hydraulic Engineering.
- Nyhaug, K. I. (2008) Ras i tilløpstunnelen til Brattset kraftverk. *Lyspunktet* 2, pp. 8–9.

- Ortlepp, W. and Stacey, T. (1994) Rockburst mechanisms in tunnels and shafts. *Tunnelling and Underground Space Technology* 9(1), pp. 59–65.
- Palmström, A. (1995) RMI – a rock mass characterization system for rock engineering purposes. PhD thesis. Oslo: University of Oslo.
- Palmström, A. (1996) Engineering geology and rock engineering applied in the design of Norwegian tunnels. *Proc. Int. Conf. on Tunnels for the Third Millennium*. Prievidza, Slovakia, pp. 59–74.
- Palmström, A. and Stille, H. (2015) *Rock Engineering*. 2nd ed. ICE Publishing.
- Panthi, K. K. (2014a) Analysis on the Dynamics of Burst Debris Flood at the Inclined Pressure-Shaft of Svandalsflona Hydropower Project, Norway. *Rock Mechanics and Rock Engineering* 47(3), pp. 923–932.
- Panthi, K. K. (2014b) Norwegian Design Principle for High Pressure Tunnels and Shafts: Its Applicability in the Himalaya. *Hydro Nepal: Journal of Water, Energy and Environment* 14.
- Panthi, K. K. (2017) Review on the prevailing methods for the prediction of potential rock burst/rock spalling in tunnels. *Fjellsprengningsdagen - Bergmekanikkdagen - Geoteknikkdagen 2017*. Ed. by K. K. Dunham et al. Oslo: Norsk Forening for Fjellsprengningsteknikk, Norsk Bergmekanikkgruppe and Norsk Geoteknisk Forening.
- Panthi, K. K. and Basnet, C. B. (2016) Review on the Major Failure Cases of Unlined Pressure Shafts/Tunnels of Norwegian Hydropower Projects. *Hydro Nepal Journal of Water Energy and Environment* 18, pp. 6–15.
- Panthi, K. K. (2006) Analysis of engineering geological uncertainties related to tunnelling in Himalayan rock mass conditions. PhD thesis. Trondheim: Norwegian University of Science and Technology.
- Popescu, M., Arsenie, D. and Vlase, P. (2003) *Applied hydraulic transients for hydropower plants and pumping stations*. Lisse: A.A. Balkema Publishers.
- Rasten, B. (2014) Virkning av hydrauliske transienter på inntaksluker på Tonstad kraftverk. Master thesis. Trondheim: Department of Hydraulic and Environmental Engineering, NTNU.
- Rathe, L. (1975) An innovation in surge-chamber design. *International Water Power and Dam Construction* 27(6-7), pp. 244–248.
- Selmer-Olsen, R. (1969) Experience with Unlined Pressure Shafts in Norway. *Symp. on Large Underground Openings*. Oslo.
- Selmer-Olsen, R. and Palmström, A. (1989) Tunnel collapses in swelling clay zones. *Tunnels & Tunneling*, pp. 45–51.

- Selmer-Olsen, R. and Broch, E. (1982) General design procedure for underground openings in Norway. *Hard Rock Tunneling, Publication No. 1*. Norwegian Soil and Rock Engineering Association.
- Sjeggedal, T. and Holter, K. G. (1998) Six case histories. *TBM Tunneling, Publication No. 11*. Norwegian Soil and Rock Engineering Association, pp. 79–83.
- Skoglund, M. (2008) Tunnelbefaring Brattset 2008.10.27.
- Solvang, E., Harby, A. and Killingtveit, A. (2011) *Økt balansekraftkapasitet i norske vannkraftverk*. Report. Trondheim: SINTEF
- Stille, H. and Palmström, A. (2003) Classification as a tool in rock engineering. *Tunnelling and Underground Space Technology* 18(4), pp. 331–345.
- Thidemann, A. and Bruland, A. (1992) Long term stability in Norwegian hydro tunnels. *Hydropower'92. Proceedings of the 2nd International Conference on Hydropower*. Ed. by E. Broch and D. K. Lysne. Rotterdam: A. A. Balkema, pp. 193–200.
- Tuseth, A. K. (2013) Numerisk modellering av luftputekammer. Master thesis. Trondheim: Department of Hydraulic and Environmental Engineering, NTNU.
- Wasantha, P. and Ranjith, P. (2014) Water-weakening behavior of Hawkesbury sandstone in brittle regime. *Engineering Geology* 178, pp. 91–101.
- Wong, L. N. Y., Maruvanchery, V. and Liu, G. (2016) Water effects on rock strength and stiffness degradation. *Acta Geotechnica (Berlin)* 11(4), pp. 713–737.
- Wyllie, D. and Mah, C. W. (2004) *Rock Slope Engineering*. 4th ed. New York: Spon Press, p. 456.
- Aasen, O., Ødegaard, H. and Palmström, A. (2013) Development of Unlined Pressure Shafts And Tunnels in Norway. *Hydropower tunnelling II, Publication No. 22*. Ed. by E. Broch, E. Grاسبakken and W. Stefanussen. Oslo: Norwegian Tunneling Society.

Online Sources

- Conacher, A. (2017) *Court rules against Glendoe client*. URL: <http://www.worldconstructionnetwork.com/news/court-rules-against-glendoe-client> (Accessed on 12/02/2018).
- Google Earth V7.3.0.3832. (2017) *Berkåk and Innset 32V 5554157 E, 6962355 N, elevation 620 m*. URL: <http://www.earth.google.com> (Accessed on 02/10/2017).
- Kartverket (2018) *Høydedata*. URL: <https://hoydedata.no/LaserInnsyn/> (Accessed on 16/04/2018).
- NGU (2018) *Kvartærgeologisk kart, løsmasser (Quaternary maps)*. URL: <http://geo.ngu.no/kart/losmasse/> (Accessed on 27/02/2018).

- Nilsen, O. and Wolff, F. (1989) *Røros og Sveg. Berggrunnskart Røros og Sveg M 1:250 000*. URL: <https://www.ngu.no/publikasjon/r-ros-og-sveg-berggrunnskart-r-ros-og-sveg-1250-000-trykt-i-farger> (Accessed on 02/10/2017).
- NVE (2017) *Vannkraftdatabase*. URL: <https://www.nve.no/energiforsyning-og-konsesjon/vannkraft/vannkraftdatabase/> (Accessed on 02/12/2017).
- NVE (n.d.) *NVE Atlas*. URL: <https://atlas.nve.no>.
- Palmström, A. (2018) *Input parameters to Q system*. URL: http://www.rockmass.net/files/Q_rating_tables-a.pdf (Accessed on 11/02/2018).
- Reynolds, P. (2017) *Judgment for contractor over Glendoe collapse*. URL: <https://www.tunneltalk.com/UK-Scotland-Jan17-Glendoe-hydropower-headrace-tunnel-collapse-judgment-for-Hochtief-against-SSE.php> (Accessed on 12/02/2018).
- Rocscience Inc. (2017) *RocData v5.008*. URL: <https://www.rocscience.com/help/rocdat a/webhelp/RocData.htm> (Accessed on 11/03/2018).
- Rocscience Inc. (2018[a]) *RS2 v9.0 webhelp*. URL: <https://www.rocscience.com/help/phase2/webhelp9/phase2.htm> (Accessed on 11/03/2018).
- Rocscience Inc. (2018[b]) *RS3 v2.0 webhelp*. URL: <https://www.rocscience.com/help/RS3/webhelp2/RS3.htm> (Accessed on 06/03/2018).
- SSB (2017) *Elektrisitet*. URL: <https://www.ssb.no/energi-og-industri/statistikker/elektrisitet/aar> (Accessed on 02/12/2017).
- SSE Generation Limited v. Hochtief Solutions AG & Another (2016) *CSOH 177*. URL: <http://www.scotcourts.gov.uk/search-judgments/judgment?id=805126a7-8980-69d2-b500-ff0000d74aa7>.
- TrønderEnergi (2017) *Brattset*. URL: <https://tronderenergi.no/produksjon/kraftverk/brattset> (Accessed on 10/12/2017).
- Wallis, S. (2009) *Rock falls shut down Glendoe power plant*. URL: <https://www.tunneltalk.com/Glendoe-Aug09-Rockfall-shutdown.php> (Accessed on 23/02/2018).

Appendix A

Strike and Dip Measurements

Strike and dip measurements from field work along E6 between Storfossen reservoir and Ulsberg on October 4, 2017.

Table A.1: Measurements at location 1 (* = adjusted measurement)

Mica schist	
Foliation	
Strike	Dip
N150°E	38°NE
N153°E*	34°NE
N150°E	35°NE
N153°E*	42°NE
N148°E	37°NE
N158°E	36°NE

Table A.2: Measurements at location 2 (* = adjusted measurement)

Mica schist					
Foliation		Joint set		Random joints	
Strike	Dip	Strike	Dip	Strike	Dip
N154°E	40°NE	N072°E	72°SE	N108°E	75°SW
N154°E	50°NE	N070°E	80°SE	N080°E	56°NW
N159°E*	35°NE				

Table A.3: Measurements at location 4 and 5

Phyllite			
Foliation		Joint set	
Strike	Dip	Strike	Dip
N164°E	40°NE	N080°E	28°N
N158°E	50°NE		
N186°E	58°NE		

Table A.4: Measurements at location 5

Quartz keratophyre	
Joint set	
Strike	Dip
N060°E	50°NW
N062°E	48°NW

Appendix B

Q-value estimation

Notes from Q-value estimation during field work 2017-10-4. ESR table, Rock support chart and Rock support classes from NGI (2015). Description and ratings for the input parameters of the Q-system from Palmström (2018).

Table B.1: Q-value estimation at location 1 and 2

	Quartzitic phyllite location 1		Quartzitic phyllite location 2	
RQD	70	(tight, few joints, fair to good)	60-70	(large joint spacing, fair)
J_n	1	(1 set + rnd)	9	(3 sets)
J_r	1.5	(rough, planar)	2	(smooth, undulating)
J_a	4	(thin filling)	4	(thin filling, chlorite clay)
J_w	1	(impermeable)	0.7-1	(open joints)
SRF	1	(good rock, moderate stress)	1	(good rock, moderate stress)
Q	26.3	(class 1)	2.3-3.9	(class 1)

Table B.2: Q-value estimation at location 5

	Amphibolite		Quartz keratophyre	
RQD	10-15	(schistose)	80	(large blocks)
J_n	6	(2 sets + rnd)	6	(2 sets + rnd)
J_r	3	(rough, irregular)	1.5	(rough, plane)
J_a	2	(slightly altered)	1	(no filling)
J_w	1	(impermeable)	0.8	(intercommunicating joints)
SRF	4	(weak rock, moderate stress)	1	(strong rock, mod. stress)
Q	0.6-0.9	(class 3)	16	(class 1)

Table B.3: Q-value estimation at location 5

Phyllite		
RQD	10	(very schistose)
J_n	6	(2 sets + rnd)
J_r	2	(smooth, undulating)
J_a	1	(no filling, some rust)
J_w	1	(impermeable)
SRF	4	(weak, moderate stress)
Q	3.3	(class 1)

Table 7 ESR-values.

7 Type of excavation		ESR
A	Temporary mine openings, etc.	ca. 3-5
B	Vertical shafts*: i) circular sections ii) rectangular/square section * Dependant of purpose. May be lower than given values.	ca. 2.5 ca. 2.0
C	Permanent mine openings, water tunnels for hydro power (exclude high pressure penstocks), water supply tunnels, pilot tunnels, drifts and headings for large openings.	1.6
D	Minor road and railway tunnels, surge chambers, access tunnels, sewage tunnels, etc.	1.3
E	Power houses, storage rooms, water treatment plants, major road and railway tunnels, civil defence chambers, portals, intersections, etc.	1.0
F	Underground nuclear power stations, railways stations, sports and public facilities, factories, etc.	0.8
G	Very important caverns and underground openings with a long lifetime, ≈ 100 years, or without access for maintenance.	0.5

Figure B.1: ESR table (NGI, 2015)

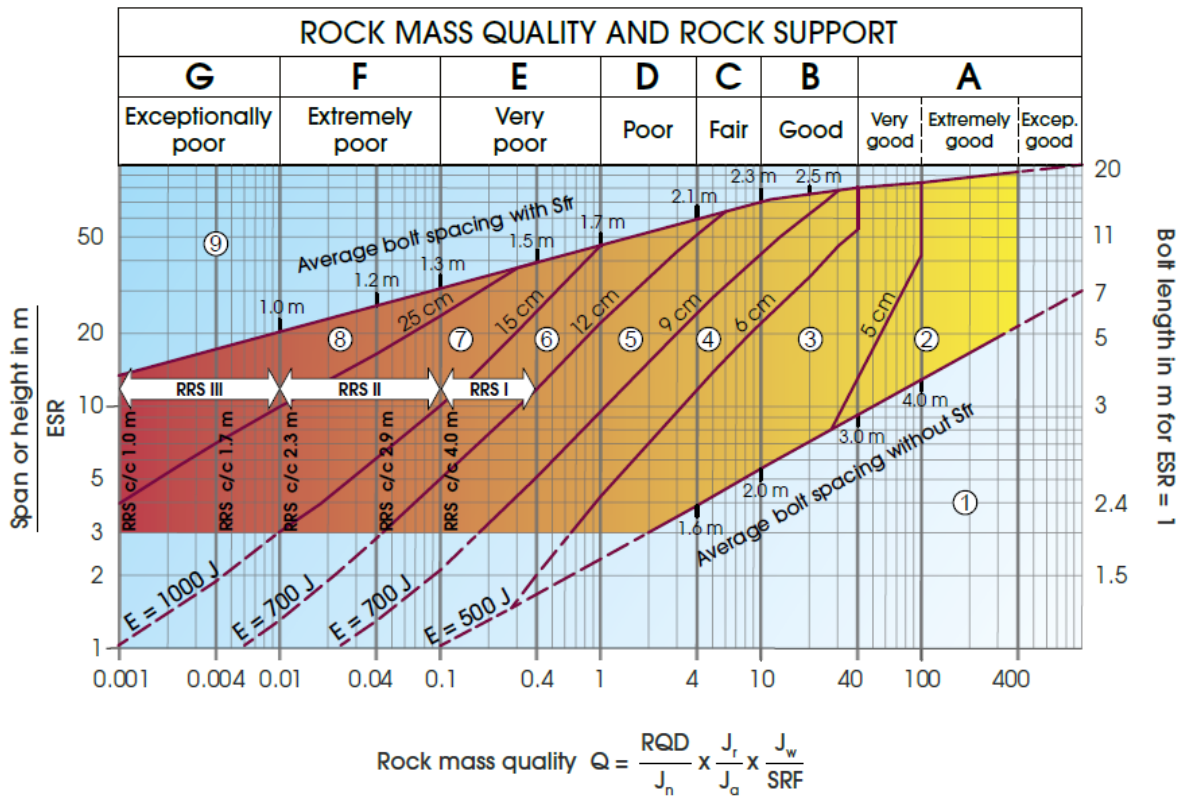


Figure B.2: Rock support chart (NGI, 2015)

Support categories

- ① Unsupported or spot bolting
- ② Spot bolting, **SB**
- ③ Systematic bolting, fibre reinforced sprayed concrete, 5-6 cm, **B+Sfr**
- ④ Fibre reinforced sprayed concrete and bolting, 6-9 cm, **Sfr (E500)+B**
- ⑤ Fibre reinforced sprayed concrete and bolting, 9-12 cm, **Sfr (E700)+B**
- ⑥ Fibre reinforced sprayed concrete and bolting, 12-15 cm + reinforced ribs of sprayed concrete and bolting, **Sfr (E700)+RRS I +B**
- ⑦ Fibre reinforced sprayed concrete >15 cm + reinforced ribs of sprayed concrete and bolting, **Sfr (E1000)+RRS II+B**
- ⑧ Cast concrete lining, **CCA** or **Sfr (E1000)+RRS III+B**
- ⑨ Special evaluation

Bolts spacing is mainly based on Ø20 mm

E = Energy absorption in fibre reinforced sprayed concrete

ESR = Excavation Support Ratio

Areas with dashed lines have no empirical data

RRS - spacing related to Q-value

I Si30/6 Ø16 - Ø20 (span 10m)
D40/6+2 Ø16-20 (span 20m)

II Si35/6 Ø16-20 (span 5m)
D45/6+2 Ø16-20 (span 10m)
D55/6+4 Ø20 (span 20m)

III D40/6+4 Ø16-20 (span 5m)
D55/6+4 Ø20 (span 10 m)
Special evaluation (span 20 m)

Si30/6 = Single layer of 6 rebars,
30 cm thickness of sprayed concrete

D = Double layer of rebars

Ø16 = Rebar diameter is 16 mm

c/c = RSS spacing, centre - centre

Figure B.3: Rock support classes (NGI, 2015)

Input parameters to Q system

Rock quality designation (RQD)

Very poor	RQD = 0 - 25%
Poor	25 - 50
Fair	50 - 75
Good	75 - 90
Excellent	90 - 100
Notes:	
(i) Where RQD is reported or measured as < 10 (including 0), a nominal value of 10 is used to evaluate Q	
(ii) RQD intervals of 5, i.e. 100, 95, 90, etc. are sufficiently accurate	

Joint set number (Jn)

Massive, no or few joints	Jn = 0.5 - 1
One joint set	2
One joint set plus random	3
Two joint sets	4
Two joint sets plus random	6
Three joint sets	9
Three joint sets plus random	12
Four or more joint sets, heavily jointed, "sugar-cube", etc.	15
Crushed rock, earthlike	20
Notes:	
(i) For tunnel intersections, use (3.0 x Jn); (ii) For portals, use (2.0 x Jn)	

Description and ratings for the parameter Jr (joint roughness number)

a) Rock-wall contact,		c) No rock-wall contact when sheared	
b) rock-wall contact before 10 cm shear			
Discontinuous joints	Jr = 4	Zone containing clay minerals thick enough to prevent rock-wall contact	Jr = 1.0
Rough or irregular, undulating	3		
Smooth, undulating	2	Sandy, gravelly or crushed zone thick enough to prevent rock-wall contact	1.0
Slickensided, undulating	1.5		
Rough or irregular, planar	1.5	Notes:	
Smooth, planar	1.0	i) Add 1.0 if the mean spacing of the relevant joint set is greater than 3 m	
Slickensided, planar	0.5	ii) Jr = 0.5 can be used for planar, slickensided joints having lineations, provided the lineations are orientated for minimum strength	
Note: i) Descriptions refer to small scale features, and intermediate scale features, in that order			

Descriptions and ratings for the parameter Ja (joint alteration number)

Contact between joint walls	JOINT WALL CHARACTER		Condition	Wall contact
	CLEAN JOINTS	Healed or welded joints:	filling of quartz, epidote, etc.	Ja = 0,75
		Fresh joint walls:	no coating or filling, except from staining (rust)	1
		Slightly altered joint walls:	non-softening mineral coatings, clay-free particles, etc.	2
COATING OR THIN FILLING	Friction materials:	sand, silt calcite, etc. (non-softening)	3	
	Cohesive materials:	clay, chlorite, talc, etc. (softening)	4	
Partly or no wall contact	FILLING OF:	Type	Partly wall contact Thin filling (< 5 mm)	No wall contact Thick filling
	Friction materials	sand, silt calcite, etc. (non-softening)	Ja = 4	Ja = 8
	Hard cohesive materials	compacted filling of clay, chlorite, talc, etc.	6	5 - 10
	Soft cohesive materials	medium to low overconsolidated clay, chlorite, talc, etc.	8	12
	Swelling clay materials	filling material exhibits swelling properties	8 - 12	13 - 20

Description and ratings for the parameter Jw (joint water reduction factor)

Dry excavations or minor inflow, i.e. < 5 l/min locally	$p_w < 1 \text{ kg/cm}^2$	Jw = 1
Medium inflow or pressure, occasional outwash of joint fillings	1 - 2.5	0.66
Large inflow or high pressure in competent rock with unfilled joints	2.5 - 10	0.5
Large inflow or high pressure, considerable outwash of joint fillings	2.5 - 10	0.3
Exceptionally high inflow or water pressure at blasting, decaying with time	> 10	0.2 - 0.1
Exceptionally high inflow or water pressure continuing without noticeable decay	> 10	0.1 - 0.05
Note: (i) The last four factors are crude estimates. Increase Jw if drainage measures are installed		
(ii) Special problems caused by ice formation are not considered		

Description and ratings for parameter SRF (stress reduction factor)

A. Weakness zones intersecting excavation	Multiple weakness zones with clay or chemically disintegrated rock, very loose surrounding rock (any depth)	SRF = 10	
	Single weakness zones containing clay or chemically disintegrated rock (depth of excavation < 50 m)	5	
	Single weakness zones containing clay or chemically disintegrated rock (depth of excavation > 50 m)	2.5	
	Multiple shear zones in competent rock (clay-free), loose surrounding rock (any depth)	7.5	
	Single shear zones in competent rock (clay-free), loose surrounding rock (depth of excavation < 50 m)	5	
	Single shear zones in competent rock (clay-free), loose surrounding rock (depth of excavation > 50 m)	2.5	
	Loose, open joints, heavily jointed or "sugar-cube", etc. (any depth)	5	
B. Competent rock, rock stress problems	Note: (i) Reduce these values of SRF by 25 - 50% if the relevant shear zones only influence, but do not intersect the excavation	σ_c / σ_1	σ_θ / σ_c
	Low stress, near surface, open joints	> 200	< 0.01
	Medium stress, favourable stress condition	200 - 10	0.01 - 0.3
	High stress, very tight structure. Usually favourable to stability, may be except for walls	10 - 5	0.3 - 0.4
	Moderate slabbing after > 1 hour in massive rock	5 - 3	0.5 - 0.65
	Slabbing and rock burst after a few minutes in massive rock	3 - 2	0.65 - 1
C. Squeezing rock	Heavy rock burst (strain burst) and immediate dynamic deformation in massive rock	< 2	> 1
	Plastic flow of incompetent rock under the influence of high pressure	Mild squeezing rock pressure	1 - 5
		Heavy squeezing rock pressure	> 5
D. Swelling rock	Chemical swelling activity depending on presence of water	Mild swelling rock pressure	5 - 10
		Heavy swelling rock pressure	10 - 15
Notes: (ii) For strongly anisotropic stress field (if measured): when $5 < \sigma_1 / \sigma_3 < 10$, reduce σ_c to $0.75 \sigma_c$.			
(iii) When $\sigma_1 / \sigma_3 > 10$, reduce σ_c to $0.5 \sigma_c$			
(iii) Few case records available where depth of crown below surface is less than span width. Suggest SRF increase from 2.5 to 5 for low stress cases		σ_θ / σ_c	

Appendix C

Estimation of GSI

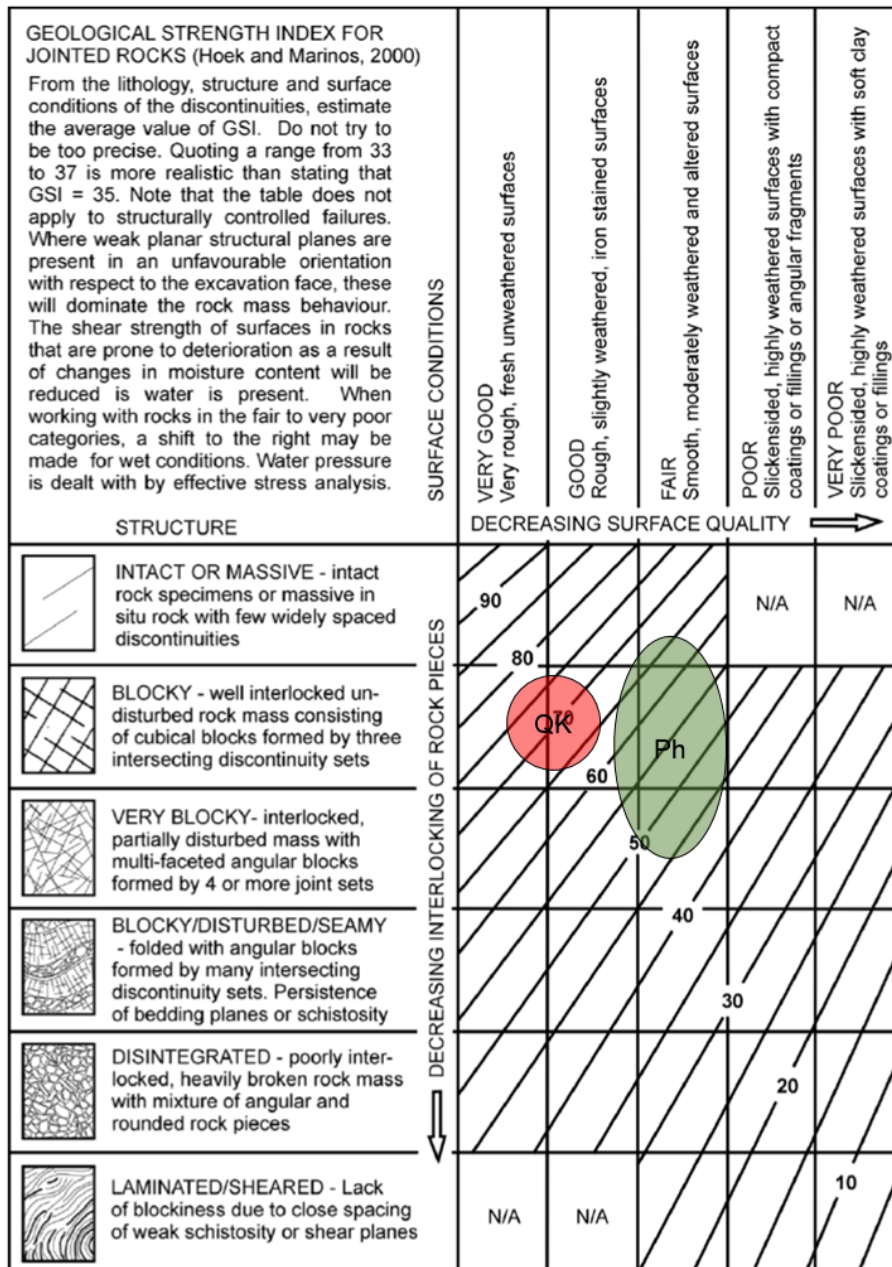


Figure C.1: Determination of GSI. Red hatch = quartz keratophyre, green hatch = phyllite. Modified from Hoek (2007).

Appendix D

Maps and drawings related to project

1. Engineering geological map
2. Observed failure events during tunnel inspections
3. Sketch of failure in weakness zone 2008
4. Illustration of Brattset HPP
5. Tender drawing of longitudinal section and alignment of tunnel system (1978)

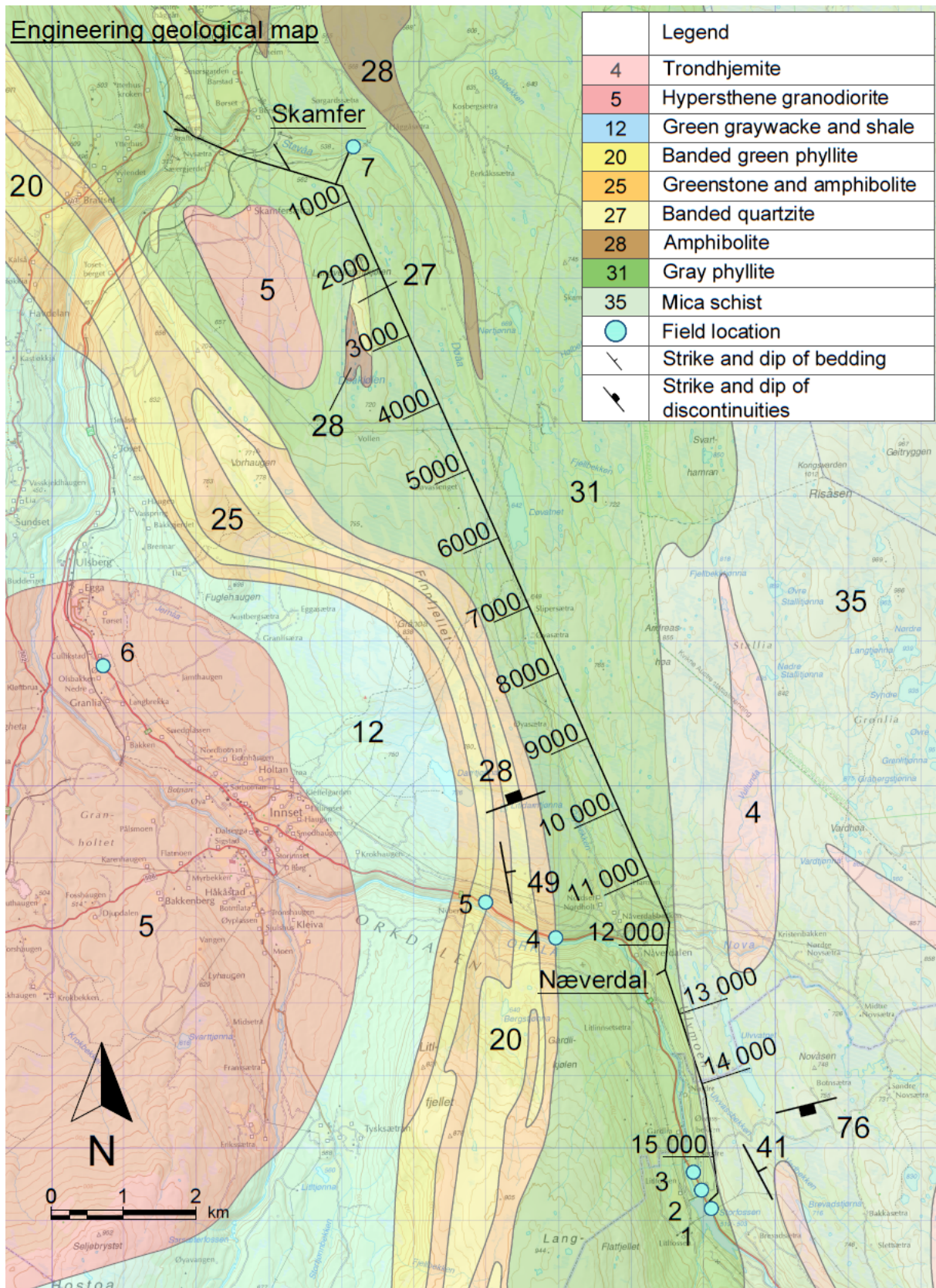


Figure D.1: Engineering geological map

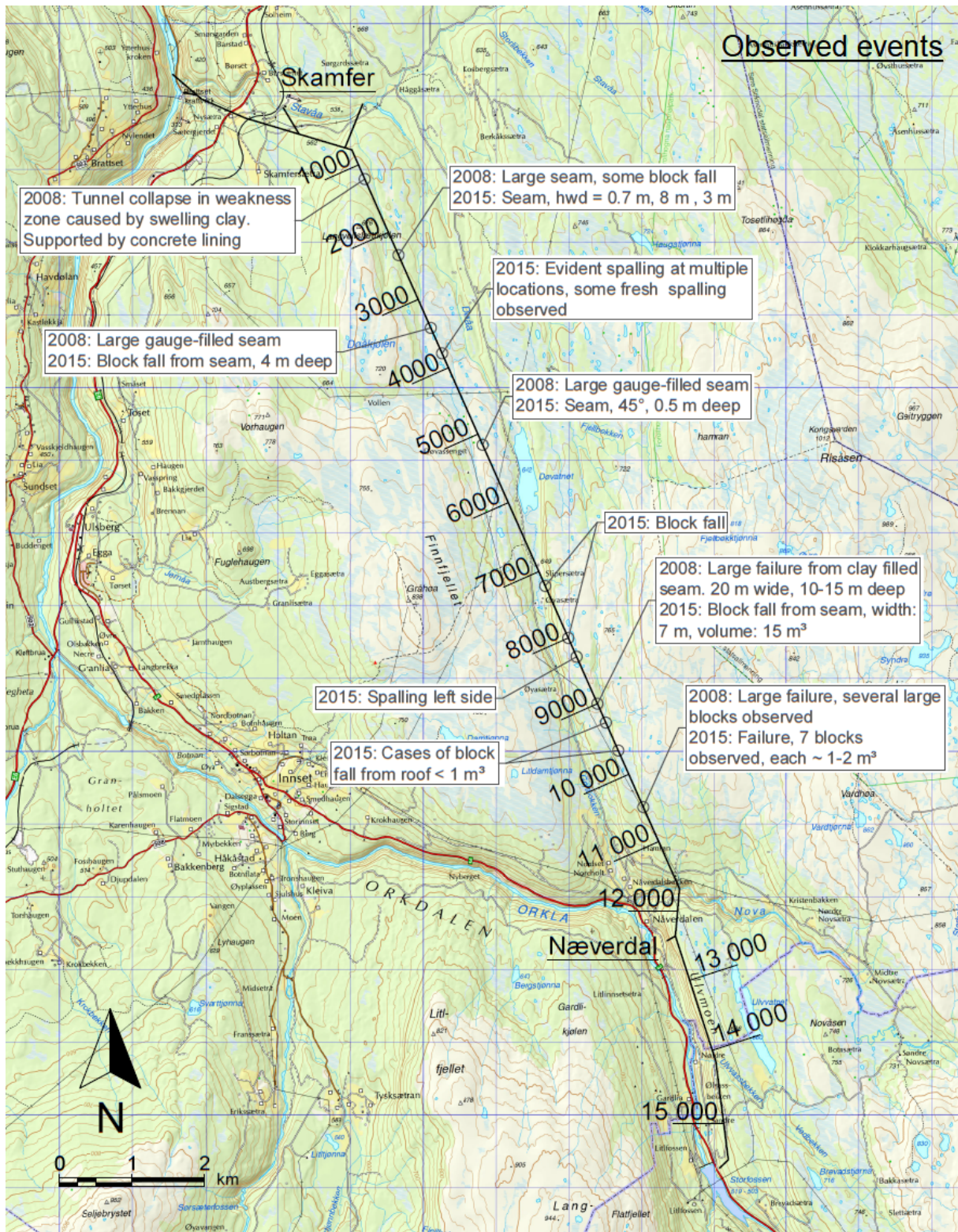


Figure D.2: Observed failure events during tunnel inspections

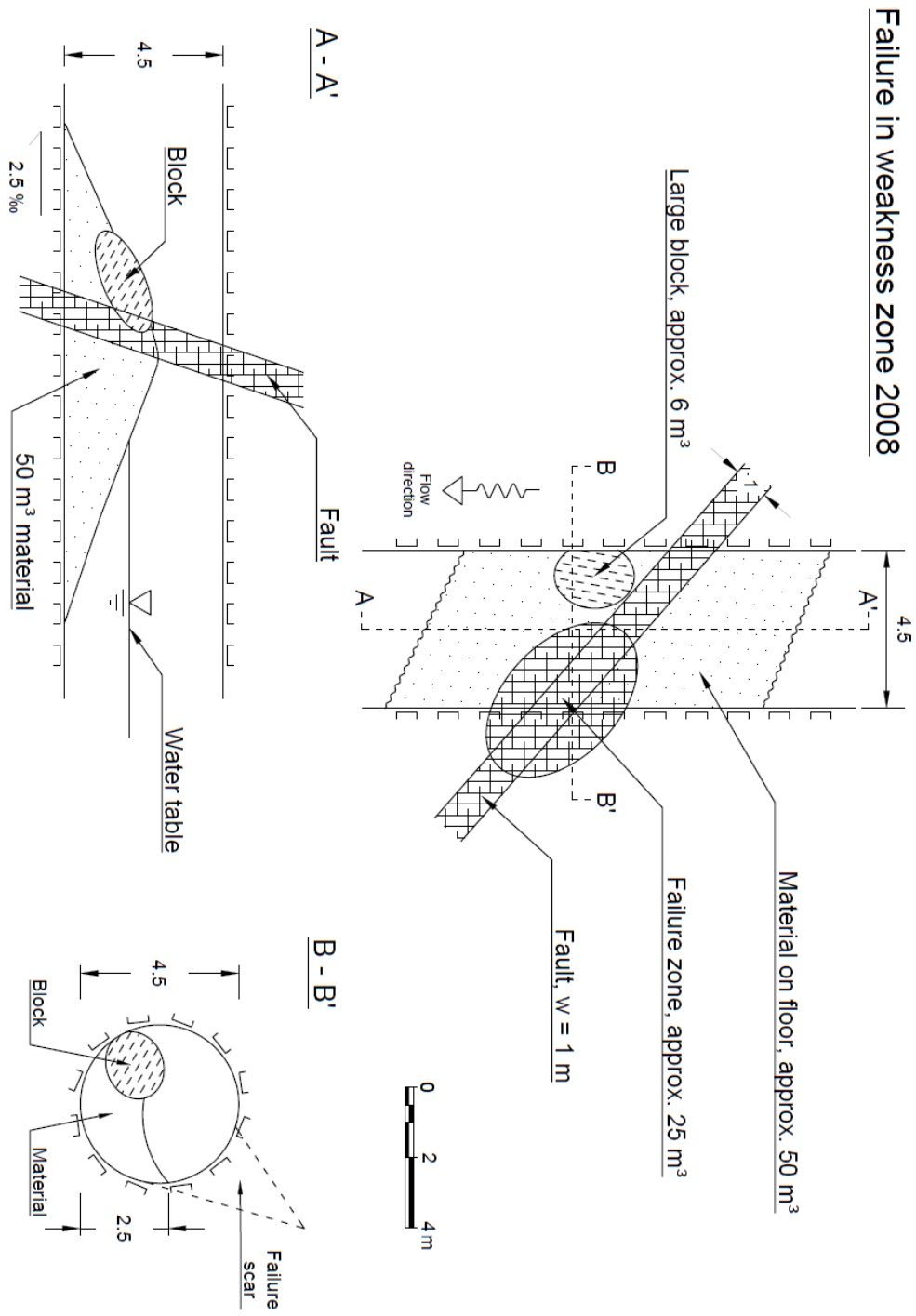


Figure D.3: Failure in weakness zone in 2008

Appendix E

Lab results

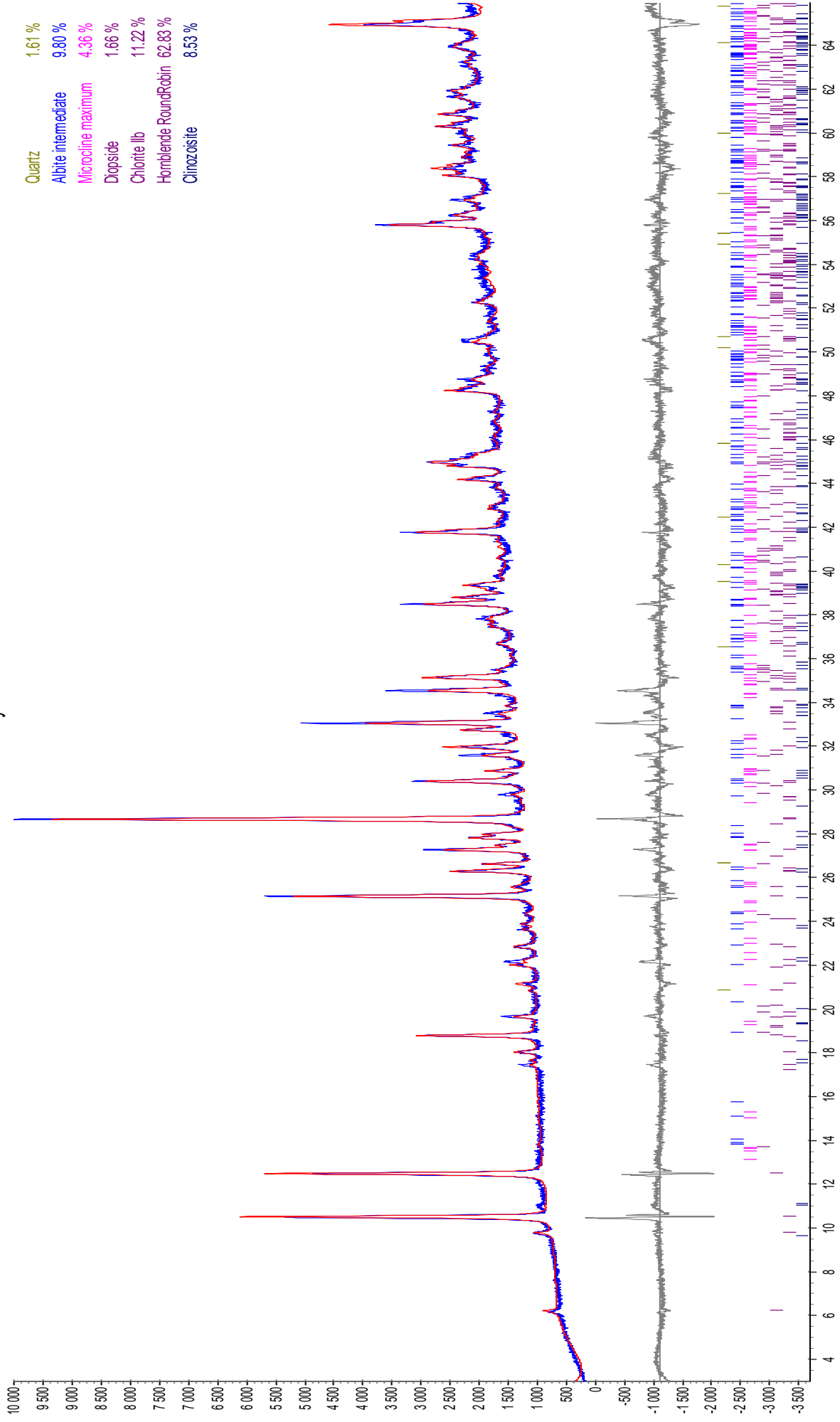
Results from laboratory tests of phyllite from Brattset (sampled near Næverdalen adit, coord. E 0555989, N 6953393).

1. Point Load test. Carried out 24.04.2018, at the Rock Mechanics Laboratory, NTNU, Trondheim. Samples were saturated for 4 days before testing.
2. XRD analysis. Carried out 30.04.2018, at the Chemical/Mineralogical Laboratory, NTNU, Trondheim.

Test #	Dir. to foliation	W ₁	W ₂	Width	Distance	Load kN	D _e ²	D _e	I _s	F	I _{s(50)}	Comment
1	perpendicular			41,7	36,3	19,72	1927,31543	43,9012008	10,23	0,94314372	9,65	Not valid
2	perpendicular			40,6	31,8	12,96	1643,85411	40,5444708	7,88	0,90998186	7,17	Not valid
3	perpendicular			50,2	34,6	30,09	2211,51523	47,0267502	13,61	0,97278918	13,24	
4	perpendicular			39,7	32,9	26,61	1663,01637	40,7800977	16,00	0,91235786	14,60	Not valid
5	perpendicular			39,9	33,3	19,45	1691,71519	41,1304654	11,50	0,91587695	10,53	
6	perpendicular			48,7	39,9	23,39	2474,06996	49,7400237	9,45	0,99765686	9,43	
7	perpendicular			39,1	31,7	12,19	1578,14222	39,7258382	7,72	0,90166742	6,96	
8	perpendicular	34,3	48,6	41,45	32,7	17,23	1725,76798	41,5423636	9,98	0,91999303	9,19	Not valid
9	perpendicular			48,4	40,8	33,05	2514,29159	50,1427123	13,14	1,0012834	13,16	Not valid
10	perpendicular			37,6	27,8	11,44	1330,89183	36,4813902	8,60	0,86775199	7,46	Not valid
11	perpendicular			39,3	33,5	14,48	1676,28352	40,9424416	8,64	0,9139905	7,90	
12	perpendicular	38,6	48,8	43,7	33,2	20,91	1847,26686	42,9798425	11,32	0,93418452	10,57	
13	perpendicular			45,1	34,2	12,78	1963,87014	44,3155744	6,51	0,94713933	6,16	
14	perpendicular			39,1	31,4	12,11	1563,20712	39,5374142	7,75	0,89974039	6,97	
15	perpendicular			34,9	30,4	27,67	1350,85623	36,7539961	20,48	0,87066393	17,83	
16	perpendicular			45,7	32,9	13,22	1914,35385	43,7533296	6,91	0,94171285	6,50	Not valid
17	perpendicular			39,1	30,9	18,87	1538,31529	39,2213626	12,27	0,89649672	11,00	
18	perpendicular			39,2	34,5	22,61	1721,92916	41,4961343	13,13	0,91953219	12,07	
19	perpendicular			40,3	37,1	24,95	1903,65864	43,6309367	13,11	0,94052651	12,33	Not valid
20	perpendicular			45	31	14,7	1776,16916	42,144622	8,28	0,92597118	7,66	
21	perpendicular			48	36,8	9,35	2249,05033	47,4241535	4,16	0,97647991	4,06	
22	perpendicular			42,2	39,3	13,57	2111,61686	45,9523324	6,43	0,96272422	6,19	Not valid
23	perpendicular			38,3	31,7	23,51	1545,85286	39,3173354	15,21	0,89748321	13,65	
24	perpendicular			47,3	31,6	22,7	1903,08568	43,6243703	11,93	0,94046281	11,22	
25	perpendicular			37,6	36,1	14,4	1728,24443	41,5721593	8,33	0,92028991	7,67	Not valid
26	perpendicular			41	31,9	22,85	1665,27	40,8077199	13,72	0,9126359	12,52	Not valid
27	perpendicular			38,8	30,9	11,23	1526,51235	39,0706073	7,36	0,89494443	6,58	Not valid
28	perpendicular			37,3	33,4	24,83	1586,22729	39,827469	15,65	0,90270473	14,13	
29	perpendicular			50,84	37,8	29,28	2446,85064	49,4656511	11,97	0,99517665	11,91	Not valid
30	perpendicular			42,3	27,5	15,65	1481,0959	38,4850088	10,57	0,88888323	9,39	
31	perpendicular			44	32,7	6,58	1831,93706	42,8011338	3,59	0,93243458	3,35	Not valid
32	perpendicular			40,6	29,3	12,82	1514,6203	38,918123	8,46	0,89337099	7,56	
33	perpendicular			40,5	25,1	21,97	1294,31166	35,9765432	16,97	0,86232751	14,64	Not valid
34	perpendicular			42	27,8	14,1	1486,63449	38,5568994	9,48	0,88963005	8,44	Not valid
35	perpendicular			37,3	32	17,54	1519,73872	38,9838264	11,54	0,89404938	10,32	
36	perpendicular			32	28,5	23,6	1161,19446	34,0763036	20,32	0,84152518	17,10	Not valid

37	perpendicular	39,4	29,6	11,54	1484,90289	38,5344377	7,77	0,88939679	6,91	Not valid
38	perpendicular	39,4	33,6	16,04	1685,56544	41,0556383	9,52	0,91512677	8,71	Not valid
39	perpendicular	38,2	36,2	12,47	1760,68657	41,9605359	7,08	0,92414892	6,55	Not valid
40	perpendicular	37,2	35,4	35,75	1676,70369	40,9475725	21,32	0,91404204	19,49	
41	parallel	33,8	25,8	0,58	1110,31581	33,3214017	0,52	0,83308433	0,44	
42	parallel	30,8	25,7	8,37	1007,84549	31,7465824	8,30	0,81513049	6,77	
43	parallel	34,7	33,4	9,5	1475,65917	38,4143094	6,44	0,88814804	5,72	
44	parallel	36,6	20,2	2,84	941,33146	30,6811255	3,02	0,80270428	2,42	
45	parallel	39,6	27,3	3,22	1376,47381	37,1008599	2,34	0,87435196	2,05	
46	parallel	38	28,42	2,15	1375,04778	37,0816367	1,56	0,87414806	1,37	
47	parallel	33,7	26	5,54	1115,61249	33,4007858	4,97	0,83397687	4,14	
48	parallel	31,3	27,3	2	1087,97046	32,9843972	1,84	0,82928221	1,52	
49	parallel	31,4	29	8,05	1159,41193	34,0501385	6,94	0,84123434	5,84	
50	parallel	33,8	21,5	7,27	925,263177	30,4181389	7,86	0,79960074	6,28	
51	parallel	30,1	20,9	5,71	800,982265	28,3016301	7,13	0,77406717	5,52	
52	parallel	32,6	23,5	5,19	975,428815	31,2318558	5,32	0,80915646	4,31	
53	parallel	41,1	32,2	5,91	1685,03068	41,0491252	3,51	0,91506144	3,21	
54	parallel	46	27,9	4,41	1634,07563	40,4237014	2,70	0,90876111	2,45	
55	parallel	44,1	38,9	4,27	2184,22971	46,7357434	1,95	0,97007568	1,90	
56	parallel	40,5	34,5	4,61	1779,03395	42,1785959	2,59	0,92630701	2,40	
57	parallel	39,6	35	5,46	1764,71001	42,0084516	3,09	0,92462366	2,86	
58	parallel	34	28,3	4,2	1225,11109	35,001587	3,43	0,85173203	2,92	

180375: Fyllitt Brattset



Appendix F

Standard chart and figures



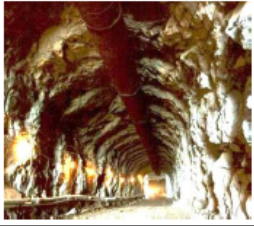
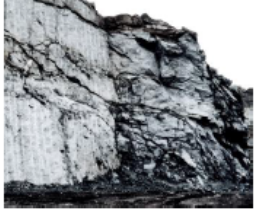

Appearance of rock mass	Description of rock mass	Suggested value of D
	Excellent quality controlled blasting or excavation by Tunnel Boring Machine results in minimal disturbance to the confined rock mass surrounding a tunnel.	D = 0
	Mechanical or hand excavation in poor quality rock masses (no blasting) results in minimal disturbance to the surrounding rock mass. Where squeezing problems result in significant floor heave, disturbance can be severe unless a temporary invert, as shown in the photograph, is placed.	D = 0 D = 0.5 No invert
	Very poor quality blasting in a hard rock tunnel results in severe local damage, extending 2 or 3 m, in the surrounding rock mass.	D = 0.8
	Small scale blasting in civil engineering slopes results in modest rock mass damage, particularly if controlled blasting is used as shown on the left hand side of the photograph. However, stress relief results in some disturbance.	D = 0.7 Good blasting D = 1.0 Poor blasting
	Very large open pit mine slopes suffer significant disturbance due to heavy production blasting and also due to stress relief from overburden removal. In some softer rocks excavation can be carried out by ripping and dozing and the degree of damage to the slopes is less.	D = 1.0 Production blasting D = 0.7 Mechanical excavation

Figure F.1: Guidelines for estimating disturbance factor *D*, from Hoek (2007)

Rock type	Class	Group	Texture			
			Coarse	Medium	Fine	Very fine
SEDIMENTARY	Clastic		Conglomerates* (21 ± 3)	Sandstones 17 ± 4	Siltstones 7 ± 2	Claystones 4 ± 2
			Breccias (19 ± 5)		Greywackes (18 ± 3)	Shales (6 ± 2)
	Non-Clastic	Carbonates	Crystalline Limestone (12 ± 3)	Sparitic Limestones (10 ± 2)	Micritic Limestones (9 ± 2)	Dolomites (9 ± 3)
		Evaporites		Gypsum 8 ± 2	Anhydrite 12 ± 2	
	Organic				Chalk 7 ± 2	
METAMORPHIC	Non Foliated		Marble 9 ± 3	Hornfels (19 ± 4) Metasandstone (19 ± 3)	Quartzites 20 ± 3	
	Slightly foliated		Migmatite (29 ± 3)	Amphibolites 26 ± 6		
	Foliated**		Gneiss 28 ± 5	Schists 12 ± 3	Phyllites (7 ± 3)	Slates 7 ± 4
IGNEOUS	Plutonic	Light	Granite 32 ± 3	Diorite 25 ± 5		
			Granodiorite (29 ± 3)			
	Dark	Gabbro 27 ± 3	Dolerite (16 ± 5)			
		Norite 20 ± 5				
	Hypabyssal		Porphyries (20 ± 5)		Diabase (15 ± 5)	Peridotite (25 ± 5)
Volcanic	Lava		Rhyolite (25 ± 5)	Dacite (25 ± 3)	Obsidian (19 ± 3)	
			Andesite 25 ± 5	Basalt (25 ± 5)		
	Pyroclastic	Agglomerate (19 ± 3)	Breccia (19 ± 5)	Tuff (13 ± 5)		

* Conglomerates and breccias may present a wide range of m_i values depending on the nature of the cementing material and the degree of cementation, so they may range from values similar to sandstone to values used for fine grained sediments.

** These values are for intact rock specimens tested normal to bedding or foliation. The value of m_i will be significantly different if failure occurs along a weakness plane.

Figure F.2: Values of the constant m_i for intact rock, by rock group, from Hoek (2007)

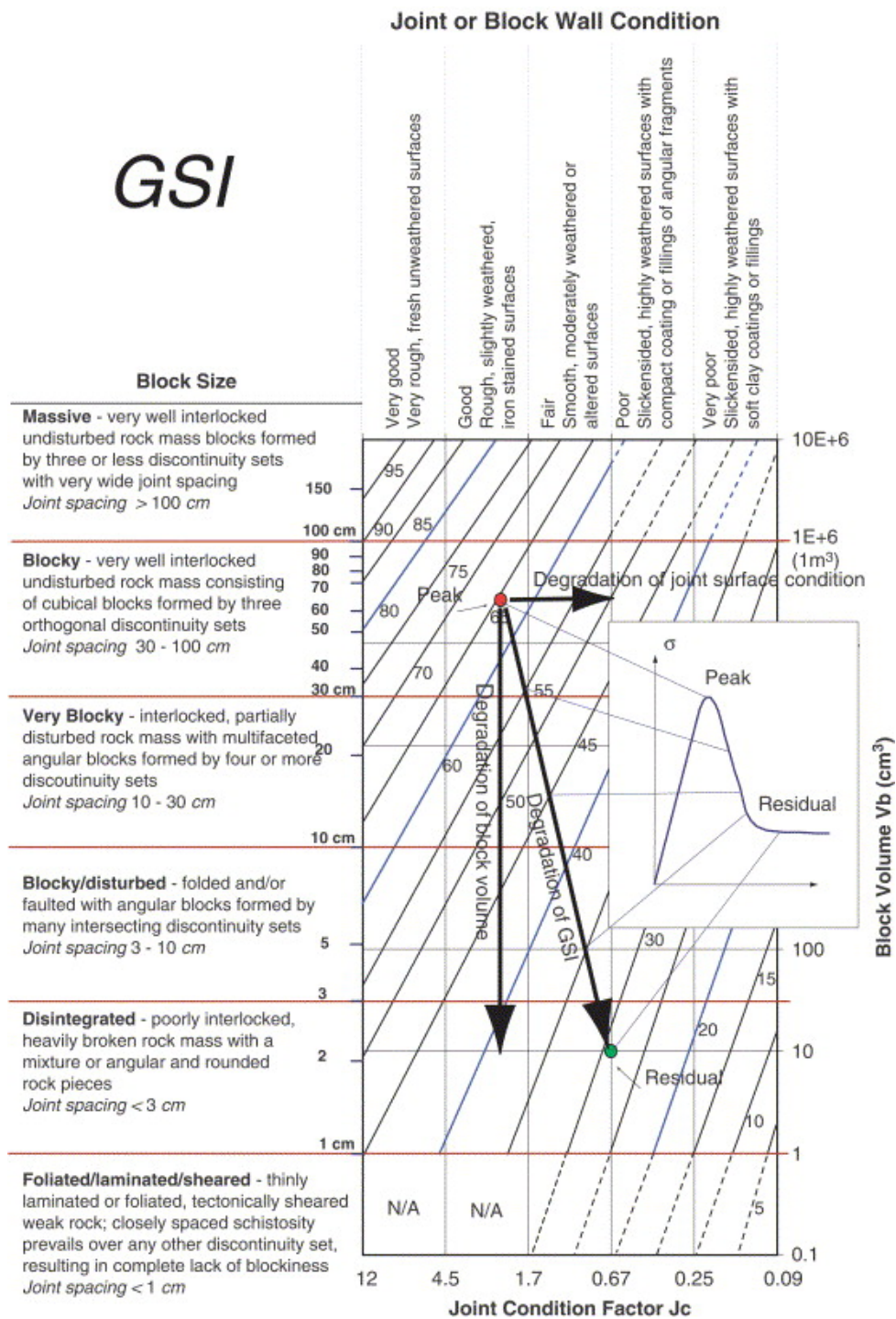


Figure E.3: Residual GSI_r , determined by the degradation of the block volume and joint surface condition from peak to residual state (Cai et al., 2007).